Dissertation

submitted to the

Combined Faculties for the Natural Sciences and for Mathematics

of the Ruperto–Carola University of Heidelberg, Germany

for the degree of

Doctor of Natural Sciences

presented by

Laurea Physicist: Della Pietra Leonardo

born in: S. Vito al Tagliamento [ITALY]

Oral examination: 24.01.2007

Coherent micromanipulation of 1-D BEC in designed potentials

Referees: Prof. Dr. Jörg Schmiedmayer
Prof. Dr. Annemarie Pucci

Zusammenfassung

Kohärente Mikromanipulation von 1-D BEC in designten Potentialen

Die Manipulation von Quantengasen hat viele neue Resultate in den letzten Jahren hervorgebracht. Eines der am häufigsten benutzten Werkzeuge, um ein Bose-Einstein Kondensat (BEC) herzustellen und zu kontrollieren ist der Atomchip: Eine lithographisch hergestellte Oberfläche, auf der Goldleiter benutzt werden, um Magnetfelder zu erzeugen.Um die speziellen Möglichkeiten des Atomchips voll auszchöpfen zu können, benötigt man folgende Techniken: Miniaturisierung der Strukturen und Integration unterschiedlicher Vorrichtungen (Resonatoren, Lichtfelder, Permanent-Magneten).

Wir haben eine Methode entwickelt um die Fallenpotentiale mikroskopisch zu strukturieren, indem wir die Oberfläche des Chips mit Hilfe einer Technologie bearbeitet haben, die die Grenzen des lithographischen Prozesses überwindet. Numerische Simulationen von Modellen wurden durchgeführt um die erzeugten Potentiale zu untersuchen. Experimentelle Daten von einer dieser Mikrostrukturen bestätigen die Erwartungen und zeigen die Qualität ihres magnetischen Potenzials. Wir schlagen auch eine periodische Struktur vor, die es ermöglichen soll, einen Quantenphasen Übergang zwischen BEC und Mott Isolator zu beobachten.

Eine weitere Möglichkeit der Erweiterung der Fähigkeiten des Atomchips ist der Einbau von Lichtfeldern nahe der Oberfläche. Wir erzeugen ein optisches Gitter auf unserem Chip und benutzen es, um einen Atom-Strahlteiler zu verwirklichen. Dabei kann das kohärente Aufspalten eines BECs beobachtet werden.

Abstract

Coherent micromanipulation of 1-D BEC in designed potentials

The manipulation of quantum degenerate gases has seen a flourishing of results in the last years. One of the most used tools to create and address a Bose-Einstein condensate (BEC) is the atomchip: A lithographycally patterned surface on which gold conductors are used to generate magnetic fields. To fully realize what the atomchip has to offer the miniaturization of structures and the integration of different devices (resonators, light fields, permanent magnets) are key factors.

We have devised a method to micro-engineer the trapping potentials by sculpturing the chip, overcoming some limitations of the lithographic process. Numerical simulations are done on model cases to show the potentials they generate. Experimental data collected on one of these microstructured geometries confirms the expectations and gives indications on the quality of its magnetic potential. We propose also a periodic structure allowing to observe a quantum phase transition between a BEC and a Mott insulator.

A further possibility for expanding the capabilities of the atomchip is integrating light fields close to its surface. We generate an optical lattice on our chip and use it to realize an atomic beamsplitter. Coherent splitting of a BEC is observed.

Multis et variis exanclatis laboribus magnisque Fortunae tempestatibus et maximis actus procellis ad portum Quietis et aram Misericordiae tandem,Luci, venisti.
Apuleius

Contents

List of Figures

Chapter 1

Introduction

The idea that light possesses momentum can be reconducted back to the end of the 19^{th} century, when we find energy and momentum of light deeply mixed in the Maxwell description of the electromagnetic field. Later on Einstein [1] pointed out the quantized nature of radiation: light comes in quanta, the photons, each of which has a well defined energy $h\,\nu$, proportional to its frequency ν, and a momentum of value $h\,\nu/c$. This knowledge of the radiation was already sufficient to realize that light pressure can be used to confine a gas. There is however an intrinsic difficulty on the way to the experimental realization of this idea, linked to the way atoms and radiation interact.

The standard way of trapping atoms with radiation is using monochromatic light of an (angular) frequency close to the visible, or around $\omega = 2\pi\,\nu = 3 \cdot 10^{15}\,\text{Hz}$; the rate at which atoms scatter photons is defined by their natural linewidth, that for the atoms used (generally alkali) lie around $\Gamma = 5 \cdot 10^{7}\,\text{Hz}$. This last factor sets also the maximum imprecision we can have in determining the wavelength of our light source $\Delta\omega$. It has to hold $\Delta\omega \ll \Gamma$. The absolute precision we need in determining the wavelength is then of at least 1 part in 10^9.

Cooling and trapping atoms with radiation is a process that has been possible only in the last decades, thanks to the enormous advances in the field of laser light generation, and nicely shows how deeply intertwingled theory, technology and experiment are.

Since the successful realization of the first ultracold atom trap [2], much has been done. On one side the availability of ultracold atom samples in an ordinary lab environment has enabled the realization of precise and compact time reference standard (atomic fountain clocks [3]), on the other it has paved the way to further cooling schemes, giving rise to the nowadays huge research field of degenerate quantum gases [4, 5].

Bose-Einstein condensates (BEC) and Fermi gases have been and are still very important in testing predictions on the most different fields of quantum mechanics, as the behaviour of weak-interacting degenerate gases [6], the couple-pairing responsible of superconducting effects [7], or quantum phase transitions in periodic structures [8]. Much has been done also in the direction of creating precise sensors [9] and there is a strong push also toward the use of the subtleties of quantum mechanics for information processing [10, 11].

Considering the way investigation is performed, we can roughly subdivide it in two fields. On one side research is done by trapping and manipulating atoms with far-detuned light potentials. This method allows to easily produce periodic potential modulations (lattices), mimicking crystal structures while at the same time allowing for greater flexibility. On the other side there is the manipulation of atoms thanks to magnetic fields. The push toward miniaturization has led to the realization of monolithic structures, on which conducting lines are deposited: the *atomchip* [12]. The atomchip allows to create miniaturized arbitrarily complex conduction structures to perform atom and quantum state manipulation with magnetic fields.

In parallel with the observation of condensates with this new tool, its limits began to appear.

When approaching the surface the BEC starts to fragment in individual blobs, due to disorder in the trapping potential. The origin of this unwanted potential modulation can be reconducted to technological limits in the realization of the current-carrying structures (see section 7.4). If we wish to fully exploit the possibilities of the atomchip, especially concerning quantum information processing and investigation of other quantum phase transitions (see chap. 4), this problem has to be addressed.

Moreover, a need of increasing complexity and flexibility of the atomchip has emerged. Optical fibers and cavities have already been integrated on the surface for atom detection, and miniaturization and control of the quality of microstructures has helped, between other things, to reduce of two orders of magnitude the amplitude of the fragmentating potential [13].

The work done in this thesis goes in that direction. We devised a new way of microengineer magnetic and electric potentials on the atomchip, by employing a technique already used in the microelectronic industry. We realize on a chip some simple geometric structures, and present a study to show what can be achieved by the technique. The BEC is then used as a ultrasensitive tool to test the characteristics of one of such structure and to observe its influence on the disorder potential. Finally a proposal is done in order to generate periodic light potentials close to the surface in view of further expanding the capabilities of the atomchip. First tests are performed showing the feasibility of the idea and the limits of the current experimental apparatus.

1.1 Organization of the work

- First we are going to explain from a theoretical point of view what a BEC is, and the physical processes we exploit to reach the Bose-Einstein condensation. The ultracold atom gas cannot be contained in a material box, which cannot be cooled down to the temperature of a BEC (100 nK range), so we use magnetic confinement. We describe the physics of the atoms in the magnetic trap, both in static and dynamic conditions. If usually we trap and address the ultracold atoms on the chip with magnetic fields, that does not encompass all the possibilities. A section is devoted to other tools to (coherently) manipulate the condensate: electric fields and light. We will explore also the limits of the condensate: deep in 1D-regimes the bosons loose phase coherence, but acquire new interesting properties and share similarities with fermions. The theoretical framework describing atom-light interaction and quantum degenerate gases has already been deeply studied, and often goes far beyond the physic touched by this work. We decided to present here only the results more closely related to our investigations. References given should help the interested reader to find deeper clarifications.

- Then there is a part devoted to the technology used in the experiment, explaining some of the developments realized. Part of the hardware solutions employed have already been described in previous works. In such cases we give only an overview and point to references for deeper details. Most of the work leading to the results presented in this PhD thesis has been done on the subjects presented in this part. In particular we realized a feedback system to stabilize the currents generating the needed magnetic fields; apart from a decrease in the currents' noise levels this solution proved of great help in removing the most annoying drifts shown by the experiment, and reduced to a few minutes the start up time. A great effort went also in the development of the experimental control software; to name just a few modifications: flexibility and automatization procedures were added to the program, a debug test-mode has been created, and event-driven triggers control now the flow of the real-time software.

- The last part presents the results achieved. We first describe the experimental cycle and dwelve into the measurements that are usually performed on a BEC. It is interesting to clarify how the different physical quantities we may be interested in can be derived from the only

measurables we have access to: imaging of a microscopic gas cloud. Some complementary insight is given by the knowledge of the stimuli and parameters we can control. There are however some possible sources of errors, often caused by side-effects of the procedure we adopt. We illustrate with some examples how they show up and influence the results. After the procedure has been explained our results are presented. We first describe the idea we had of creating microscopic structures on the atomchip by ion beam milling and show the characteristics of some model cases. Numerical simulations are done in order to study quantitatively the potentials they generate. Experimental data has been collected on one of these microstructured potentials that confirms the expectations and gives indications on the quality of the magnetic potentials it realizes. We propose also a periodic structure allowing to observe a BEC-Mott insulator quantum phase transition. The limits of this technique are given by the minimum distance at which the trapping potential is still smooth. Finally, in the last chapter we give the results of first measurements which show it is possible to couple light fields in the close vicinity of the chip surface. This helps in overcoming some of the limitations intrinsic in magnetic trapping.

1.2 Conventions and notation used

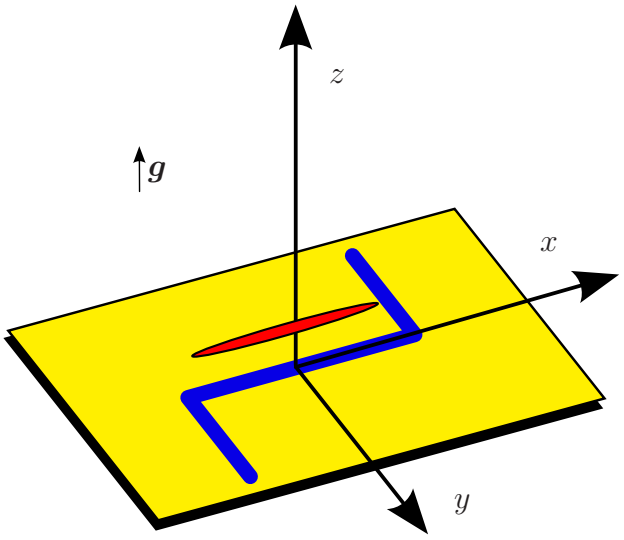

Figure 1.1: The chip with a typical ***Z*** trapping wire (blu), the atomic cloud (red) and the reference system. The z axis points toward the earth center

The experiments performed in this work are all done close to a gold-covered surface: the *atomchip*. On the chip various gold structures are used to trap atoms; it is natural to use a system of reference referred to the trapping structure. This is shown on fig. 1.1, and is determined by the following assumptions:

- The z axis is perpendicular to the chip surface, with zero on the chip surface in correspondence of the trapping structure[1], and positive values of z above the surface. As the chip is mounted upside-down (sec. 6.4 and 5) it is oriented as the gravity acceleration.
- The trapping structure is generally a straight wire with the ends bent to form a ***Z***. We fix the x axis in the direction of this wire, with the zero in its central part.

[1] On the chip there may be gold layers of different thickness, but instead of defining a global zero it makes more sense to define the atom-surface distance at the position where the atoms really are.

- The remaining y axis is also parallel to the chip surface, and perpendicular to x, with zero above the trap center. x, y, z form a right-oriented basis.

The trap is cigar-shaped, and has a symmetry axis along x. When the discussion is related to the trapping conditions it makes sense to consider directions parallel to this axis (also denoted as longitudinal direction) and perpendicular to it; parameters connected to them are thus indicated, respectively, by the subscripts $\parallel$ and $\perp$.

As example we may consider here the trapping frequencies: $\nu_x \equiv \nu_\parallel$ and $\nu_y \equiv \nu_\perp \equiv \nu_z$ (the last equivalence is due to the fields generating the trap). We will often call *trap frequency* also the *angluar frequency* $\omega_i = 2\pi \cdot \nu_i$. The magnetic field $\boldsymbol{B}$ components are similarly indicated; moreover as in the minimum of the trap $B_y = B_z = 0$ the value of the field minimum will be denoted by B_x.

We tried to keep the same notation throughout the whole work, in order to ease the reading. A list of the most used symbols and physical constants is given in appendix A, and can be easily accessed any time a symbol used in a certain passage is not locally defined.

As last note, we would like to call the attention on the units used. Although the SI unit for the magnetic field is the Tesla, being $|\boldsymbol{B}|$ often of values around $10^{-4}\,T$ we found more convenient to use the Gauss. The system we work with is a cloud of Rb atoms in the maximally stretched spin state $m_F = 2$, trapped in a magnetic field and with temperatures of $10^{-4} - 10^{-7}\,\mathrm{K}$; energies will be often expressed in temperature units ($E = k_B T$), in frequency ($E = h\nu$) or as a magnetic field ($E = \boldsymbol{\mu} \cdot \boldsymbol{B}$); a useful equivalence to keep in mind is

$$1\,G \;=\; 67.1\,\mu K \;=\; 1.4\,\mathrm{MHz} \tag{1.1}$$

Part I

THEORY

Chapter 2

Interaction of atoms and electromagnetic field

Matter and the EM field interact in the most various ways; this chapter deals mainly on how to use the electromagnetic field to cool or to manipulate cold neutral atoms.

Using light to cool atoms is something done routinely with modern-day technology. The theoretical background can be traced back to the beginning of the 20^{th} century, with Einstein paper on the quantum theory of radiation [1] , followed by the experimental demonstration of the radiation recoil [14]. We have to wait the end of the 70s, with the rapid developments in the field of lasers, to have the first proposals and experiments for cooling atoms with radiation pressure [15, 16, 17], and eventually for trapping them [18, 19]. A nice overview of the possibilities of laser cooling can be found on the Nobel lectures Of S. Chu, C.N. Cohen-Tannoudji and W.D. Phillips [20, 21, 22].

2.1 The MOT

The more successful way of cooling atoms to much below the mK is a combination of magnetic fields and laser light, the *Magneto Optical Trap*, or MOT for short. We explain here its working principle. A simple recipe to cool and trap atoms is given by the following ingredients [23, 24]:

- A viscous force, dispersive and preferably proportional to velocity.
- A space-dependent force, with a minimum at the position where we want to trap the atoms.

It turns out we can realize it with a combination of laser light and static magnetic fields. Let us consider for simplicity a model atom with a closed optical transition of frequency ω_A (*two-level system*), wavevector k, wavelength λ, linewidth Γ, excited state lifetime τ and a total spin for ground and excited state $F_g = 0$ and $F_e = 1$. We take then a light source of intensity I, frequency ω_L, so that $\delta = \omega_A - \omega_L$ denotes the detuning of our light source from the atom transition. If the atom absorbs a photon, its momentum changes by $\Delta \boldsymbol{p} = \hbar \boldsymbol{k}$. As the spontaneously emitted photon (averaging out) carries no net momentum (fluorescence photons are emitted isotropically), it can be seen that the atom moving is slowed down if it absorb photons from a beam propagating opposite to it. The Doppler effect is of help in realizing this. If the atom moves against the light source with a velocity v, the average force[1] it feels, due to the continuous absorption and subsequent reemission of photons, is dependent on both v and δ, and its value is given by:

$$\langle \boldsymbol{F}(s, v, \delta) \rangle = \hbar k \cdot \frac{\Gamma}{2} \cdot \frac{s}{1 + s + \left[\frac{2(\delta - kv)}{\Gamma}\right]^2} \tag{2.1}$$

[1] This force is the average over many absorption-reemission events

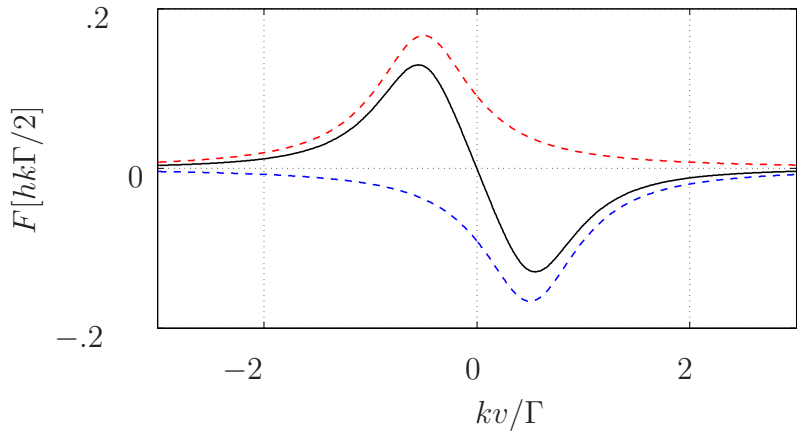

Figure 2.1: Viscous force in the MOT. *Dashed lines*: force of each single light source. *Continuous curve*: combined force from eqn. 2.1, for $\delta = -0.5$, $s = 0.2$.

the saturation parameter $s = I \cdot \frac{3\lambda^3\tau}{\pi hc}$ describes effectively 'how much' light is present, in terms of 'how much' can be absorbed by the atom. The maximum force, for high intensities, has a value of $F = \hbar k\Gamma/2$ at resonance ($\delta = \boldsymbol{kv}$). Its limit is fixed by the lifetime of the excited atom τ. The spontaneous absorption/emission cycle has in fact a minimum duration of $2\,\tau$ (in high light intensities). As a consequence the atom-light interaction due to this process cannot be increased at will. If we now shine two counterpropagating laser beams on the atom, with a detuning δ from resonance, the combined force they exert on the atom (fir $s \ll 1$) can be linearized around $v = 0$, and its value is:

$$\langle \boldsymbol{F}(s, v, \delta)\rangle_{Total} = \alpha v \qquad \text{with} \qquad \alpha = \frac{8\hbar k^2 \delta s}{\Gamma(1 + s + 4\frac{\delta^2}{\Gamma^2})} \tag{2.2}$$

The equations 2.1 and 2.2 tell us:

- In order to maximize the viscous force on its linear region we need detunings of the order of the linewidth Γ. The ^{87}Rb D_2 transition has a frequency $\nu = 384\,\text{THz}$, and a $\Gamma = 2\pi \cdot 6.06\,\text{MHz}$, thus we have to define the cooling light wavelength with a precision much better than one part in about 10^7: only the development and availability of lasers has allowed cooling by light.

- For a viscous force we need red detuning: when the atom moves against a laser beam the Doppler blue shift compensates for it and a photon is absorbed, slowing down the atom.

- The force of eqn. 2.2 should ideally stop completely the atom; however, that formula is valid *only* if we can average to zero the momentum acquired by the atom from the isotropic spontaneous emission. When the atom is cold, the discreteness of the absorption/emission process will make the atom follow a sort of *Brownian motion* (with a diffusion constant) in the momentum space [25].

This last point sets the minimum reachable kinetic energy/temperature for $\delta = \Gamma/2$, a quantity known as *Doppler limit*:

$$k_B T(\delta) = -\frac{\hbar T}{4}\left(\frac{\Gamma}{2\delta} + \frac{2\delta}{\Gamma}\right) \qquad T_{Doppler} = \frac{\hbar\Gamma}{2k_B} \simeq 140\,\mu\text{K} \tag{2.3}$$

To realize a trap we need additionally a spatially dependent force. This is done by interacting with the atom magnetic spin; the interaction is obtained thanks to a quadrupole magnetic field,

generated by two coaxial coils with counterpropagating currents: an *anti-Helmholtz configuration* (fig. 2.2). The spatially dependent Zeeman detuning, coupled with the choice of the correct light polarization (circular, σ^+ and σ^- as in fig. 2.2 right[2]) gives rise to a force similar to that of eqn. 2.2, but now with spatial dependence:

$$\langle \boldsymbol{F}(s,\boldsymbol{r},\delta)\rangle_{+/-} = \pm\hbar k \cdot \frac{\Gamma}{2} \cdot \frac{s}{1+s+\frac{4(\delta_{+/-}(\boldsymbol{r}))^2}{\Gamma^2}} \qquad \text{with} \qquad \begin{cases} \delta_{+/-}(\boldsymbol{r}) = \delta \pm \frac{\mu' B(\boldsymbol{r})}{\hbar} \\ \mu' = \mu_B(g_e m_e - g_g m_g) \end{cases} \tag{2.4}$$

where the choice of the sign depends on the light polarization. A visual representation of the situation is given in fig. 2.2, left. Atoms displaced from the trap center interact with the laser light only if the photons possess the right spin, and are so excited to the m_e state in resonance (in the figure $m_e = 1$).

The Zeeman shift needed (in energy) has to be of the same order of $\Gamma\hbar$, so the corresponding magnetic field at the border of the trap (a few mm from its center) is, for ^{87}Rb, of a few Gauss. This can be done with ordinary copper coils (no need of superconducting inductances).

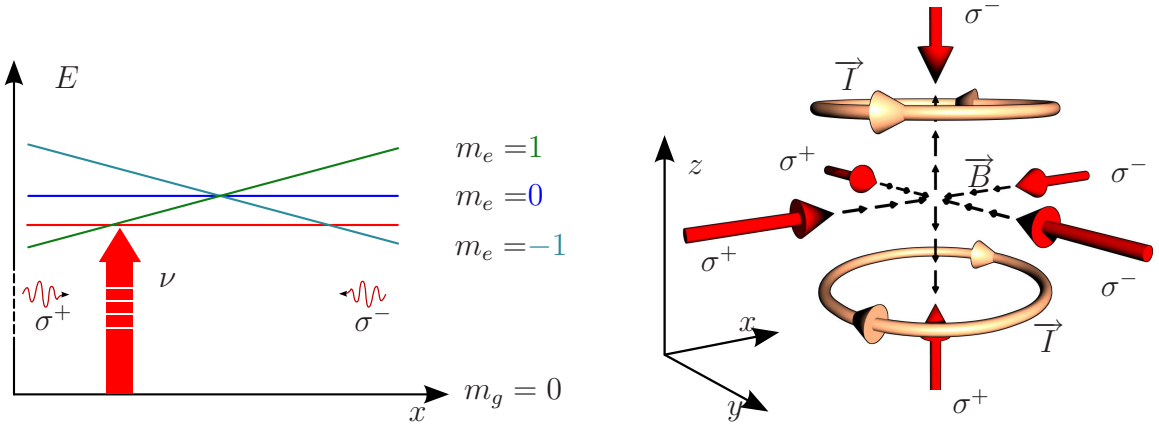

Figure 2.2: *Left*: schematic representation of the energy levels of the atom in a magnetic field; the red line represents the energy of the laser photons, of frequency ν; only one of the spin levels $m_e = \pm 1$, at a precise position in space (x) has the right Zeeman shift to move the resonance toward ν. Subscripts e and g are, respectively, for the excited and ground state. *Right*: Representation of the laser beams in a MOT (Red arrows) with indication of polarization (spin, not polarity), and of the quadrupole coils (yellow), with black arrows to show the magnetic field direction [2].

Summarizing: two counterpropagating laser beams generate each a velocity-dependent force given by eqn. 2.1, and with vectorial sum that for atoms with velocity around $v = 0$ can be linearized as in eqn. 2.2. Similarly if we add a quadrupole magnetic field there is a couple of spatially-dependent forces given by eqn. 2.4 linearizable around the MOT center ($\boldsymbol{B} = 0$). Then we obtain for the atoms the equation of motion of the *damped harmonic oscillator*. Given the interaction strength for ^{87}Rb[3], the atoms are cooled and trapped on a timescale of a few ms. Atoms are accumulated in the trap, usually for a few seconds (depending on the vacuum conditions, see section 2.2, and on the mutual interaction between trapped atoms), at which point the equilibrium of collection with losses is reached. Such a trapping scheme, because of its working principles, has

[2] We give the polarization of the light in the lab frame, as well as the magnetic fields values; an alternative possibility, that highlights the symmetries of the MOT, is using the helicity to indicate the photons' spin; in this case however the magnetic field vector has to be specified in respect to the light propagation, and we have to renounce to a global coordinate system.

[3] ^{87}Rb has a D_2 transition lifetime of 26 ns, and the momentum of a single photon gives to the atom at rest a recoil velocity $v = 6$ mm. At room temperature $v = 200 - 300$ m/s

been named *Magneto Optical Trap*, or MOT. In reality things get a bit more complicated, because both the *Doppler* and *Zeeman* detuning are present at the same time and interfere with each-other in determining the absorption rate. Similarly we have interference between the effects of the forces along the three spatial directions. Finally, the spin levels of real atoms can be more complex than depicted in 2.2. As an example, the transition used to trap ^{87}Rb goes from a total spin of $F_g = 2$ to $F_e = 3$, thus allowing in principle transitions between 5 and 7 m_F spin levels. The presence of counterpropagating laser beams creates also standing light waves in the region of the MOT where intensity, or polarization, changes periodically with position. Such a situation has been exploited for cooling schemes allowing to go below the Doppler temperature 2.3, such as the *Polarization gradient cooling*, or *Sisyphus cooling*, and *subrecoil laser cooling* or *dark state cooling*, that does not rely on the spontaneous emission any more [26, 27]. However, as such advanced cooling techniques are not relevant for our experiment, we are not going to explore them any further. The interested reader can easily find references to them (one example is the Nobel lecture of S. Chu [20]).

2.2 Vacuum

How many atoms can be trapped in a MOT? A first limit is given by the same forces acting in the MOT: the atoms inside the cold atomic cloud emit spontaneously resonant light, that exerts radiation pressure on the same trapped atoms. This limits the maximum cloud density and thus the maximum amount of atoms. Moreover in a dense cloud light cannot reach the center region. But there is another phenomenon that we have to consider: the ultracold cloud is confined inside a vacuum chamber. The background and untrapped Rb atoms and molecules of the remaining gas in the chamber in thermal equilibrium with the chamber walls ($T \simeq 300\,\mathrm{K}$) have a certain probability of hitting atoms in the MOT per time unit. Following ref. [28] we can write the rate equation for the atom number in the MOT as:

$$\frac{dN}{dt} = R - \frac{N}{\tau} \tag{2.5}$$

with N as the total atom number, R as the loading rate of the atoms, τ as the loss time constant, defined by:

$$\frac{1}{\tau} = \sum_i n_i \sigma_i \bar{v}_i + n_{Rb} \sigma_{Rb} \bar{v}_{Rb} \tag{2.6}$$

In the last eqn. n_x is the density of scattering particles, σ_x the scattering cross section, $\bar{v}_x$ their average thermal velocity and the subscripts i and Rb are, respectively, for the various background atoms/molecules and untrapped ^{87}Rb. The derivation of this equation assumes the target (MOT atom) is at rest (which is true to a good approximation) and can be found in most thermodynamics textbooks. The differential equation 2.5 yields a maximum atom number $N_{max} = \tau \cdot R$, which is approached exponentially with a time constant given by τ.

In our experiment we achieve a long lifetime ($\tau \simeq 20s$) and a high loading rate (about $1 - 4 \cdot 10^7$ atoms/s) using a double MOT setup (see chap. 5), where a first MOT, at a higher pressure $p \simeq 10^{-9}$ mBar can load Rb efficiently, and a second one, kept at $10^{-11} < p < 3 \cdot 10^{-12}$ mBar, is loaded with Rb extracted from the first MOT with a push beam. A thin nozzle allows the buildup of the pressure difference between the two chambers. After 10 s of loading time the upper MOT has about $1 - 4 \cdot 10^8$ atoms .

2.3 The magnetic trap

To reach the extremely high phase-space density needed (low temperature and high enough density) for Bose-Einstein condensation the MOT is not sufficient. The same holds true as well for further

cooling techniques based on atom-light interaction. We have thus to somehow store the cold atoms and employ then different cooling techniques. Two are the solutions adopted:

- A strongly focused, far red detuned laser light is used to create a dipole trap, using the *AC Stark effect* that atoms experience in a light field.
- A minimum of the magnetic field is created in space, and atoms interact with it by their magnetic spin: a magnetic trap.

Both schemes have been successfully adopted, and each has its limitations. In our experiment we work close to lithographically patterned surfaces: the atomchip (see chap. 7). The chip enables us to address atoms with electric and magnetic potentials defined on the micrometer scale. The most natural trap for us is the magnetic one.

A particle, with total spin $\boldsymbol{F}$ and magnetic moment $\boldsymbol{\mu} = g_F \mu_B \boldsymbol{F}$ in a magnetic field B feels a potential:

$$U_B = -\boldsymbol{\mu} \cdot \boldsymbol{B} = g_F \mu_B m_F \left|\boldsymbol{B}\right| \tag{2.7}$$

where the symbols are, as usual, μ_B the Bohr Magneton, g_F the Lande' factor and m_F the magnetic quantum number. The sign of the potential changes with respect to the mutual orientation of the magnetic field and of the spin (or on the m_F value, considering as spin base the one defined by the direction of $\boldsymbol{B}$)

Magnetic traps for atoms are realized in free space in proximity of structures generating magnetic fields (either wires or permanent magnets). No maxima of the magnetic field can be realized in free space (*Earnshaw* theorem), so the standard solution is to use spin states with positive m_F, also known as *weak-field seeking* states, with their spin aligned opposite to $\boldsymbol{B}$. In such a way the atoms are attracted toward the region where a minimum of $|\boldsymbol{B}|$ is located, can be stored and eventually further cooled. A trap with a depth of a few Gauss can contain atoms with temperatures of tens of μK.

The simplest configuration is the *quadrupole trap* [29], realized by a couple of coaxial coils with antiparallel current flow (*Paul trap*). The center of the trap sits at a field $B_0 = 0$. As $\boldsymbol{B}$ has no sources the gradient along one spatial direction (the coils axis) is twice as big as along the other two. In such traps the magnetic field vectors have an orientation that depends on the position. The atomic spin can follow its variations only if, with the motion of the atom, the field variation is slow compared with the timescale of the spin precession around the local field: the spin then follows adiabatically $\boldsymbol{B}$. Such timescale is given by the inverse of the *Larmor precession frequency* $\omega_L = \mu_B B/\hbar$. At the minimum of the trap this approximation no longer holds, and spin flips can happen, with consequent loss of atoms [30].

One solution adopted in the early experiments on Bose-Einstein condensation was the dynamic displacement of the trap minimum around the atoms, that feel a time-averaged potential (the *TOP trap* [31]). A second one was the use of a *light plug*, a far blue detuned laser beam (see chap. 2.5) to repel the atoms from the quadrupole minimum [4].

A trap which has become a standard tool is the *Ioffe-Pritchard trap* [32, 33, 34], in which the field minimum created by the current flowing in four rods (a sort of magnetic guide between them) is closed longitudinally by the field of two coils. The trapping is usually strongly anisotropic, with its longitudinal confinement (along the rods direction) much weaker than the perpendicular one.

Since then the development of magnetic traps has moved toward the miniaturization of structures. A first step was the *Keplerian guide*, where a particle orbits around a current-carrying wire [35, 36, 37, 38]. The atoms move around the wire, and the conservation of angular momentum prevents them from hitting it. Along the direction of the wire they are however free to move.

Another trap, on which those realized on our chip are based, is the *side guide*. The basic idea is to superpose a magnetic field generated by a wire in which the current I flows with a homogeneous one B_y (orthogonal to the direction of the wire), so that they cancel each other at a certain distance

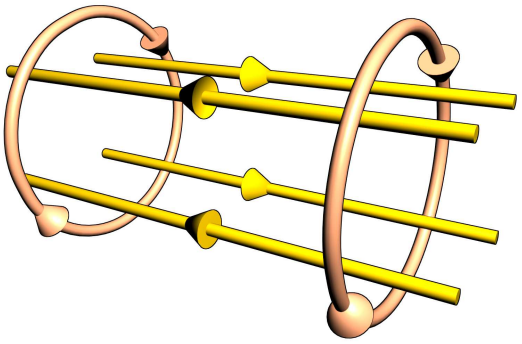

Figure 2.3: A schematic view of the Ioffe trap, with the two coils for the *bottle field* providing both longitudinal confinement and field minimum B_{IP}, and the four rods for transversal confinement.

from the wire r_0 [39]. For round wires two important parameters are r_0 and the field gradient (in the plane perpendicular to the wire) can be computed by:

$$r_0 = \left(\frac{\mu_0}{2\pi}\right)\frac{I}{B_y} \qquad \left.\frac{dB}{dr}\right|_{r_0} = \frac{2\pi}{\mu_0}\frac{{B_y}^2}{I} = \frac{B_y}{r_0} \tag{2.8}$$

To minimize losses due to the so-called *Majorana spin-flip* an extra field is added, B_{IP} usually named *Ioffe-Pritchard* field, so that the trap minimum is non zero. The potential (around the minimum) is in first approximation harmonic in two directions, and the trapped atoms oscillate transversely with the angular frequency $\omega_\perp$; this is usually the highest frequency of the trap. It has to hold [40, 41]:

$$\omega_\perp = \sqrt{\frac{\mu_B g_F m_F}{m_{Rb}}\left(\frac{d^2B}{dr^2}\right)} = \frac{B_y}{r_0}\sqrt{\frac{\mu_B g_F m_F}{m_{Rb}B_{IP}}} \ll \omega_L \tag{2.9}$$

and spin-flip rate due to atomic spin not following adiabatically the field change experienced by the atom moving in the trap is given by:

$$\gamma = 4\pi\omega_\perp e^{-2\omega_L/\omega_\perp} \tag{2.10}$$

This guide is however confining only along two directions and leaves the atoms free to move in the third one. In order too have a real trap it has to be closed by two endcaps. A possible solution is the bending of the wire to form a ***U*** shape. The other one is to create a ***Z*** structure: This second realization has the advantage that the field configuration has a minimum different from zero, such that it prevents Majorana losses without the need of an external B_{IP}. Due to the wire topology the trap is highly anisotropic, with a much weaker longitudinal confinement.

Such basic structures can be further altered, as shown in fig. 2.4, allowing for traps with independent adjustment of transversal and longitudinal trapping frequencies (***H*** trap), or with a potential more box-like in the longitudinal direction (*double* ***S*** endcaps).

Although all these wire configurations look quite different, some common behaviour can be observed:

- Structures far away from the trap center (e.g. the ***Z*** arms) generate fields components that add up vectorially, and whose direction at the center of the trap is close to the vertical (in the fig. 2.4 perpendicular to the image). The remaining field is due to the not perfect cancellation of all the contributions. As the cancellation is more precise going closer to the wire, the longitudinal frequency $\omega_\parallel$ goes to zero at $z = 0$, on the wire surface.

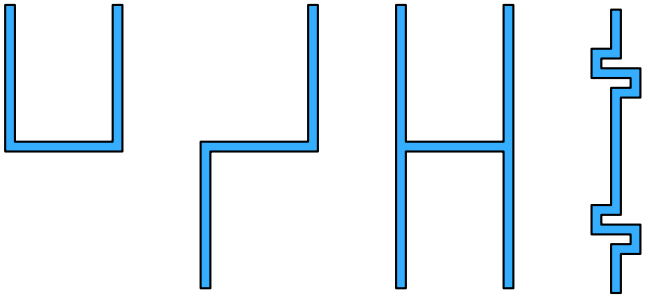

Figure 2.4: Some of the more common wires' configuration for the realization of magnetic traps: the ***U***, the ***Z***, the ***H*** and the ***double S***.

- The field gradient of a thin wire goes as $1/z$ above the trap center (see eqn. 2.8), and so does the transversal trap frequency $\omega_\perp$. This dependence on z is valid as long as the distance from the wire is bigger than its transversal dimensions. For smaller distances, the current density inside the wire has to be taken into account for the calculation of the fields (finite-size effect), and generally $\omega_\perp$ reaches a maximum value.

Thus going closer to the current-carrying structure increases the trap anisotropy; for extremely miniaturized structures, as those realized in our atom chips, values $\omega_\perp/\omega_\parallel > 1000$ are not uncommon. Further details can be found in the review papers [12, 42]

Another force experienced by the atoms in the magnetic trap, and not yet considered is the gravitational one. The gravitational field of the earth affects almost all atoms' traps (there are some experiments in presence of microgravity): it causes a shift of the trap minimum downwards and eventually, for too weak confinements, leads to the loss of the atoms. With the usual frequencies reached of $\omega_\perp > 2\pi \cdot 100\,\mathrm{Hz}$ this is not a problem.

We finish this part with a short consideration on the spin. As described in the section 2.1 on the MOT, the atoms interact continuously with the laser light. When the magnetic trap is switched on, we have to consider the atomic spin components along the local magnetic field (quantization axis): The population having $m_F < 0$ is expelled and gets lost. The transfer from the MOT to the magnetic trap is a critical moment, and some tricks are used to minimize losses.

- After the collection of a high enough atom number in the MOT (we get $N = 1 - 4 \cdot 10^8$) the fields are first increased, in order to compress the trap and to concentrate the atoms within the small trapping area, and then switched off suddenly; the laser intensity and detuning (eqn. 2.3) are ramped so that the minimum possible temperature is reached. This phase, named ***optical molasses*** (because of the dissipative force proportional to velocity), has a duration of a few ms. Longer times can lead to appreciable diffusion of the atoms, that move now at a few cm/s.

- The position of the magnetic trap is adjusted so that it matches that of the center of the MOT; this procedure, called ***mode-matching*** avoids unnecessary heating that can happen during the transfer between the traps by exciting oscillations.

- A homogeneous magnetic field (bias field along the y direction B_y) is applied: it serves as quantization axis for the atoms' spin. A short pulse of polarized light is shot; this ***optical pumping*** beam is used in order to transfer within few transitions all the atoms to the $m_F = +2$ state along B_y.

- The current in the ***Z*** wire structure is switched on, so that the magnetic field configuration of the trap is formed; the number of captured atoms $N = 3 - 8 \cdot 10^7$ are sufficient for proceeding to the last step in the road toward BEC: the evaporative cooling.

2.4 Evaporative cooling

For further cooling the atoms, we move from optical transitions to RF photons, by using a technique known as RF cooling. The atoms in the trap experience a different magnetic field, depending on the spatial position; hotter ones can move further away from the trap minimum and are subject to a higher Zeeman splitting. The irradiation of RF photons induces m_F spin flips into non-trapped states (for $m_F < 0$) and atoms are expelled from the trap (see fig. 2.5). When decreasing the energy of the photons $E_{RF} = h\nu_{RF}$ colder atoms are addressed, until only the coldest remain.

In the ideal case, only the hottest atoms are removed: this maximizes the reduction of kinetic energy per atom number loss. If we define the mean particle energy $\bar{\epsilon}$, then we can quantify the effect of RF cooling by introducing the parameter β: $(1+\beta)\bar{\epsilon}$ is the mean energy of the particles removed. If we remove only the hottest atoms β has high values, while its minimum is $\beta = 0$ and corresponds to the situation when we remove all the atoms.

It can be shown [43] that the temperature of the atoms remaining in the trap T varies as:

$$\frac{\mathrm{d}\ln T}{\mathrm{d}\ln N} = \beta \tag{2.11}$$

It's clear that in order to maximize the energy loss per atom number loss we should remove only the hottest atoms. In principle, as the magnetic trap has a finite depth, we could get cooling already with the spilling of particles over the trapping potential. Such cooling processes, although possible and used with some modifications in all-optical traps[4] has the disadvantage of being slow, with a characteristic time constant increasing exponentially with β.

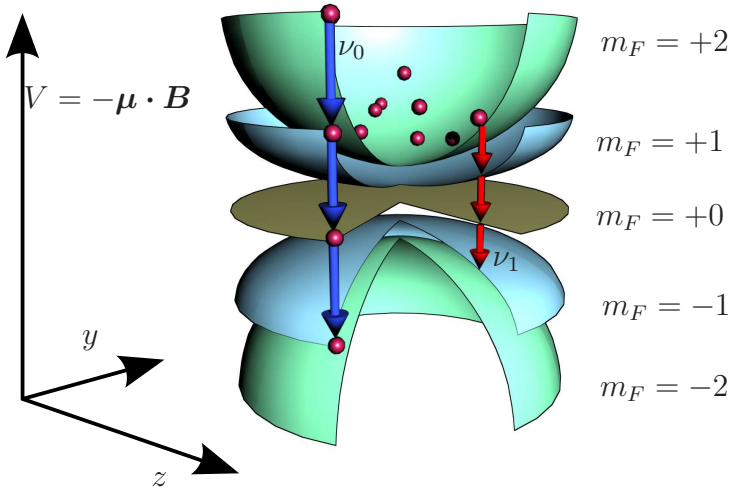

Figure 2.5: An atom with total spin $F = 2$ sitting in a harmonic magnetic field: to each m_F corresponds a different potential; a RF photon can couple the different m_F. Hotter atoms populate regions where $|\boldsymbol{B}|$ is bigger, experiencing a bigger Zeeman splitting; thus moving from higher RF frequencies (ν_0) to lower ones (ν_1) we selectively remove colder and colder atoms, leaving the coldest in the trap. The figure schematically shows a 2D section of the magnetic trap for the different m_F, and the effect of the interacting RF photons at higher (blue arrows) and lower (red arrows) frequencies.

In this regard we have to consider the other loss mechanisms that do not cool atoms. We have already seen in equation 2.6 the contribution of the scattering with background gas. Another loss

[4] In optical traps it is not possible to use the spin-flip evaporation procedure, as the trapping does not depend on the spin state. The standard method to cool atoms is then the controlled reduction of the trap depth.

channel is due to the *two-body spin relaxation*; it depends linearly on the atoms' density n, but as we are working in the maximally stretched state of $F = m_F = 2$ it is strongly suppressed [44]. Higher relevance covers the *3-body losses* process [45, 46]. As it is proportional to n^2 its effect grows toward the end of the RF sweep, with the increased density reached. However, as also the elastic collision rate increases with n, in most trap geometries (usually harmonic and slightly anisotropic) a regime known as *runaway evaporation* is reached, and rethermalization remains the dominating process [47, 43].

The importance of the previous considerations shows up when we define the time evolution of the RF and of the trap frequencies. One can show that optimizations are possible that lead to a considerable increase in the final atom number [48, 49].

2.5 Electric and optical fields

2.5.1 Static fields

Atoms placed in a static electric field $\boldsymbol{E}$ interact with it: the electron orbitals (mainly in the outer shell) are modified by $\boldsymbol{E}$, and a dipole moment $\boldsymbol{p}$ is induced. The relation between the two is determined by the electrical polarizability α. Although generally α is a complex tensor, for atoms of the first group (Alkali-metals), that have only one unpaired electron in a s shell, it is a positive scalar. Dipole momentum and interaction energy are then respectively:

$$\boldsymbol{d} = \alpha \boldsymbol{E} \qquad\qquad V_0 = -\frac{1}{2}\,\boldsymbol{d}\cdot\boldsymbol{E} = -\frac{1}{2}\,\alpha E^2 \tag{2.12}$$

The electric field interaction is independent of the atomic spin; combining magnetic and electric fields allows for more flexibility in the addressing of atomic quantum states.

As clear from eqn. 2.12 we have a minimum of the interaction potential V_0 in correspondence of a field maximum; the *Earnshaw theorem* prohibits to have a maximum of E^2 in free space ($\nabla \cdot \boldsymbol{E} = 0$), so a stable electric trap is not realizable.

This limit can be overcome using dynamic fields: modulating $\boldsymbol{E}$ with frequencies deep into the MHz range (quasi-static in respect to the electronic dynamics but much faster than the atomic motion), or close to the atomic transitions, where α is imaginary (see below). Another possibility is to realize the trapping with magnetic fields.

To have an idea of the strength of the interaction, let us consider the atom we are dealing with, ^{87}Rb. We have then $\alpha = h \cdot 7.94 \cdot 10^{-6}\,\mathrm{Hz/(V/m)^2}$. Typical fields on the atomchip can be around $E = 0.1\,V/\mu\mathrm{m}$, corresponding to $V_0 \simeq 1.9\,\mu\mathrm{K}$. Such potentials, when space-varying, can be used to modulate the magnetic trap (sec. 11.2.1).

2.5.2 Light fields

A laser field is an intense (high *luminosity*) and coherent source of electromagnetic radiation. The oscillating electric field generated interacts with the atoms, but differently from the static case we have to consider how α varies in respect to the radiation frequency ω. It is instructive to study the case of a classical electron oscillating in one dimension under the influence of the time-varying electrical field $E(t)$, and with natural frequency ω_0 (given by our atomic transition). The equation of motion and the polarizability are in this picture:

$$\ddot{x} + \Gamma_\omega \dot{x} + \omega_0^2 x = -\frac{e}{m_e} E(t) \qquad\qquad \alpha = \frac{e^2}{m_e} \cdot \frac{1}{\omega_0^2 - \omega^2 - \mathrm{i}\omega\Gamma_\omega} \tag{2.13}$$

where the damping $\Gamma_\omega = \frac{e^2\omega^2}{6\pi\epsilon_0 m_e c^3}$ is due to the radiative energy loss of the accelerated electron (rotating around the atom). These results, although naïve in the derivation, are quite precise for alkali metals.

The knowledge of α is essential to derive the two most important parameters describing the interaction of light and atoms: the dipole potential V_0 (already met above in the case of static fields) and the scattering rate Γ_{sc}, telling us how long a single atom can stay in the light field before becoming excited. The imaginary part of α describes an out of phase component of the polarizability, and is then associated with energy exchange between field and electron (absorption), while the real part determines V_0. This can be easily seen if we take the time averages over one oscillation period:

$$V_0 = -\frac{1}{2}\,\langle \boldsymbol{p}\cdot\boldsymbol{E}\rangle = -\frac{1}{2\epsilon_0 c}\,\mathrm{Re}(\alpha)\,I \qquad \Gamma_{sc} = \frac{P_{abs}}{\hbar\omega} = \frac{\langle \dot{\mathrm{p}}\cdot \mathrm{E}\rangle}{\hbar\omega} = \frac{\mathrm{Im}(\alpha)}{\hbar\epsilon_0 c}\,I \tag{2.14}$$

here I is the laser light intensity. At resonance α is purely imaginary and as it should be we have a maximum in the scattering. Expressing now eqn. 2.14 in terms of Γ, the natural decay rate (or using the classical picture as above $\Gamma \equiv \Gamma_{\omega_0}$), and following the derivation of V_0 and Γ_{sc} given in most textbooks and reviews on the subject [50], we obtain:

$$\begin{aligned} V_0 = &\quad -\frac{3\pi c^2}{2\omega_0^3}\left(\frac{\Gamma}{\omega_0-\omega}+\frac{\Gamma}{\omega_0+\omega}\right) I \quad &\simeq -\frac{3\pi c^2}{2\omega_0^3}\left(\frac{\Gamma}{\Delta_\omega}\right) I \\ \Gamma_{sc} = &\quad \frac{1}{\hbar}\frac{3\pi c^2}{2\omega_0^3}\left(\frac{\omega}{\omega_0}\right)^3\left(\frac{\Gamma}{\omega_0-\omega}+\frac{\Gamma}{\omega_0+\omega}\right)^2 I \quad &\simeq \frac{1}{\hbar}\frac{3\pi c^2}{2\omega_0^3}\left(\frac{\omega}{\omega_0}\right)^3\left(\frac{\Gamma}{\Delta_\omega}\right)^2 I \end{aligned} \tag{2.15}$$

where $\Delta_\omega = \omega - \omega_0$; the equations are valid in the limit of low intensity (compared to the saturation intensity, $I/I_s \ll 1$) and large detunings ($|\Delta_\omega|\,\Gamma \gg 1$). The last step is justified if $|\Delta_\omega|/\omega \ll 1$, that is for detunings small compared with the transition frequency: this is known as the *rotating-wave approximation* (RWA). Both V_0 and Γ_{sc} decrease for higher detuning, however:

$$\frac{V_0}{\hbar\Gamma_{sc}} = \frac{\Delta_\omega}{\Gamma} \tag{2.16}$$

in fact Γ_{sc} decays quadratically in Δ_ω, while V_0 only linearly. To decrease the dissipative scattering processes we have to move to a larger detuning (if we have enough laser power I to achieve the desired potential). The other handle we can work on is Γ, but that is fixed once the atomic species are. Finally another note on V_0. Due to its linear dependence on the detuning we can reverse its sign, by moving from red to blue shifts. Usually laser traps for atoms are realized with red detunings; it is easy to create a region of maximum for the light fields, by focusing a laser beam, and the atoms are then attracted there. However if we have a standing wave, blue detuned, the minima of V_0 are also the minima of the intensity, and as consequence we can minimize the scattering (atoms sit in dark spots).

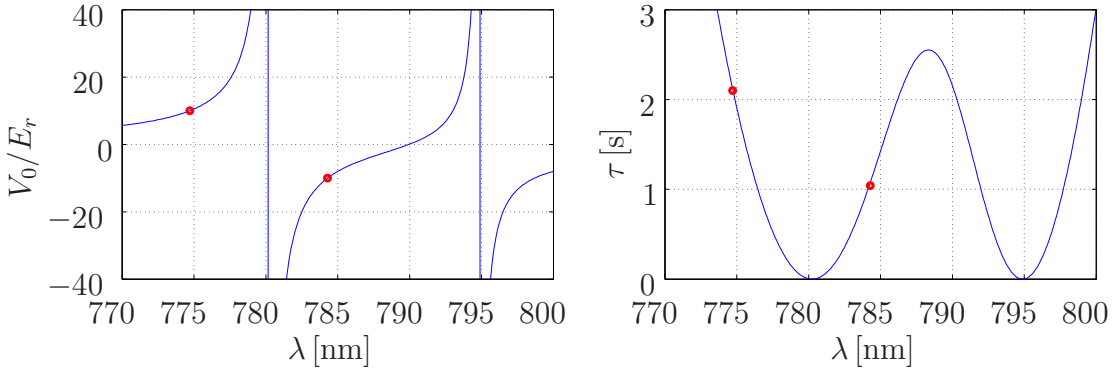

Figure 2.6: Dipole potential V_0 in lattice recoil energy units E_r (left) and lifetime before scattering (right) in a 0.5 W/mm^2 beam, around the D_1 and D_2 ^{87}Rb transitions (794.9, 780.2 nm).

What said so far is valid on systems where there is a dominating transition. In case of alkali more are possible, with different energy splitting between them. The biggest split is due to the spin-orbit coupling, giving rise to the D_1 and D_2 doublet (see app. B) with a frequency difference of $\Delta_{fs} = 7.1\,\mathrm{THz}$, or $14.7\,\mathrm{nm}$. Then, in order of importance, we have the hyperfine splitting of the S ground state $\Delta_{hf,0} = 6.8\,\mathrm{GHz}$ and of the excited P states, $\Delta_{hf,1} \simeq 100 - 800\,\mathrm{MHz}$. Simplifications are possible if we work in the limit $\Delta_{fs} \gtrsim \Delta_\omega \gg \Delta_{hf,0}$. In the experiments performed with standing waves we will always be in this range, with detunings of $1 - 13\,\mathrm{nm}$; moreover the waves will be realized with linearly polarized light. We can then write [50]:

$$V_0 = \frac{\pi c^2 \Gamma}{2\omega_0^3}\left(\frac{2}{\Delta_2}\right) I \qquad \Gamma_{sc} = \frac{1}{\hbar}\frac{\pi c^2 \Gamma^2}{2\omega_0^3}\left(\frac{2}{\Delta_2^2} + \frac{1}{\Delta_1^2}\right) I \tag{2.17}$$

with Δ_1, Δ_2 as detunings from the D_1, $D2$ transitions. The laser power accessible in the lab allows to have potential depths of tens of times the lattice recoil energy $E_r = \hbar^2 k_0^2 / 2m_{Rb}$ (where k_0 is the wave vector) and lifetimes τ (before absorption occurs) around $1\,s$. If both blue or red detuning are available there may be a convenience in choosing one of the two. In fig. 2.6 it is evident that if we want $V_0/E_r = 10$ (red circles) a blue detuning has twice the lifetime and twice the power stability ($\mathrm{d}V_0/\mathrm{d}\lambda$) of the red shift.

The dipole potential of a standing wave can be used to create a lattice, that we may combine with a magnetic trap on which a BEC is loaded. If the amplitude V_0 is big enough a MI transition should be observed (sec. 4.2).

Chapter 3

BEC descriptions

3.1 Maxwell-Boltzmann, Bose-Einstein, Fermi-Dirac statistics

The classical theory of thermal motion and the classical statistics, summarized in the Maxwell-Boltzmann distribution, achieved huge successes in describing highly complex systems, where it is impossible (computationally and experimentally) to follow the evolution of every dynamic variable.

The textbook example is given by the description of a gas, where we work with a number of particles of the order of $N_A \simeq 10^{23}$, each living in a 6-dimensional coordinate space[1] (position and momentum), whose state and evolution (under reasonable assumptions like quasi-equilibrium dynamics) can be described by equations as simple as:

$$pV = nRT \tag{3.1}$$

To be fair saying we can describe the evolution of N_A particles with the three free parameters p, V and T is a bit cheating. In reality we are just describing the quantities we are interested in, and we still ignore how each single gas molecule moves. We will do something similar in the forthcoming sec. 3.3 with a *softer* kind of matter.

The classical statistics worked quite well with gases, and achieved successes also in describing quantities as the heat capacity of some solids, but it failed with conductors. As each atom in a conductor has one or more free electrons, it was expected that these, moving as a gas inside the conductor would contribute with a heat capacity of $C = 3\,\mathrm{cal/K \cdot mole}$[2], whereas the observation contradicts this assumption.

As we all know, this is due to the fact that the *fermions*, as electrons are, cannot occupy the same quantum state, because of *Pauli exclusion principle*; in a solid the free electrons occupy energy levels up to the *Fermi energy*, that for silver is $E_F/k_B \equiv T_F = 6 \cdot 10^4\,\mathrm{K}$, so only those at the highest levels can acquire the thermal energy ($E = kT$ at room temperature is only a tiny fraction of T_F) and jump to some free or partially occupied level, contributing to C.

What we see here is the quantum mechanical properties of the matter entering actively into the physics, modifying dramatically macroscopic quantities. This is because the particles' *indistinguishability* and the Pauli exclusion principle have a huge impact on statistics, that lies as mathematical foundation of the *physics of the heat*. To account for the quantum properties of the matter and extend the results obtained with ideal gases, the following statistics have to be considered:

- *Maxwell-Boltzmann* [**MB**]: The classical one, with distinguishable particles.

[1] for molecules there may be other degrees of freedom.
[2] the unit given here is the usual one in the field, not the SI equivalent.

- *Fermi-Dirac* [**FD**]: Particles are indistinguishable and cannot occupy the same quantum state; this applies to all the semi-integer spin particles.
- *Bose-Einstein* [**BE**]: Particles are indistinguishable and can occupy the same state; it is the statistics of the integer spin particles

If particles are indistinguishable, exchanging two of them does not modify the picture and as a practical result we have less ways to arrange N_p particles in N_s levels. Other conditions can come from the type of particles we are working with. For example if they are atoms, the total number N_p is fixed as well as the total energy E_{tot}; on the contrary the photons in a cavity (*black body radiation*) are absorbed and reemitted continuously from the cavity walls, and N_p is generally not a conserved quantity.

A certain number N_b of books have already dealt with such questions, and apart from introducing some concepts we do not want to repeat the story here; we will only give some more results, following ref. [51]. If we have a system with well defined energy levels (as for example particles confined on a box), denoted by the index s, each with degeneracy g_s and energy ϵ_s , it can be shown with basic reasoning that the number of particles in each level n_s is given by the equations:

$$MB \qquad \frac{n_s}{g_s} = \frac{1}{e^{(\epsilon_s-\mu)/(k_BT)}} \tag{3.2}$$

$$FD \qquad \frac{n_s}{g_s} = \frac{1}{e^{(\epsilon_s-\mu)/(k_BT)}+1} \tag{3.3}$$

$$BE \qquad \frac{n_s}{g_s} = \frac{1}{e^{(\epsilon_s-\mu)/(k_BT)}-1} \tag{3.4}$$

where the free parameter μ, also known as *chemical potential* of the system, is fixed by the constraints on the total energy, k_B is the Boltzmann constant and T is the equilibrium temperature.

Equation 3.2 is the well known equation that leads to the Maxwell-Boltzmann distribution. The chemical energy can be factorized and solved by summing over the whole particle number (N is constant). We get then the *partition function* of the system:

$$Z \equiv \sum_{s=1}^{\infty} g_s e^{\epsilon_s/k_bT} = N \Big/ \left(e^{-\mu/k_BT}\right) \tag{3.5}$$

Equation 3.3 describes the probability of occupation of the energy levels for Fermions. At $T = 0$, for all energies $\epsilon_s < \mu$ the occupation probability is 1, and is 0 if $\epsilon_s > \mu$. This is the case of the electrons in a metal. The situation at higher T is summarized in fig. 3.1.

The last one, equation 3.4, is valid for Bosons. Next section will explore its predictions at low temperature.

3.2 The Bose-Einstein condensate

For the *bosons* the situation is quite different. This can be understood from the following example: assume to have N particles and consider the two distributions:

- 1 atom in each of the N lowest energy levels.
- $N-1$ atoms in the lowest one, and 1 in a higher level, so that the total energy E is the same as that of the previous distribution.

For the MB statistics the possibilities of realizing the first distribution are $n!$, due to the distinguishability of the particles. The second one can be done in n different ways, by choosing each time a different particle for the highest state.

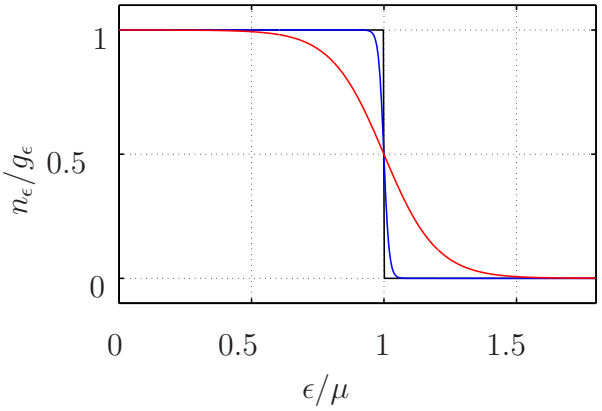

Figure 3.1: Occupation probability for FD statistics (normalized to the degeneracy index g_ϵ). The discrete levels s are represented here by the continuous energy variable ϵ (valid for $s \gg 1$). Curves, from squared to smooth, correspond to $T/\mu = [0,\ 0.01,\ 0.1]$. For $T = 0.1\,\mu$, corresponding to $T = 6000\,\mathrm{K}$ in the case of silver, only 7% of the electrons are excited.

For the BE statistics there is only one way of realizing each of the two distributions, because of the indistinguishability of particles.

We already see that MB, in respect to BE, predicts a much lower occurrence of distributions with a high occupation of lower levels. Such behaviour led A. Einstein, thanks to an idea originally developed by S. N. Bose [52, 53], to predict a new state of the matter, nowadays known as *Bose-Einstein condensate*. In such a state ideally all the particles of the system occupy the ground quantum level.

Because of the extremely high phase-space density needed to observe the Bose-Einstein condensation, it took various decades to experimentally realize it. The first boson cooled to temperatures where quantum phenomena as *superfluidity* emerge has been helium. But although ^{4}He is superfluid below $T = 2.2\,\mathrm{K}$ the interaction between atom and atom is so high that in the experiments done only around 10% of the atoms occupied the lowest level, and a mixture of *superfluid+fluid* fractions always exist.

Gases have a low mutual interaction, but at low temperatures they tend to solidify. Exceptions are Hydrogen and alkali atoms, that due to their low three-body inelastic scattering cross section (at densities reached in experiment) remain in a metastable gaseous phase for a sufficient amount of time. Although the first candidate for condensation was H (1959, [54]), the first condensate was achieved with ^{23}Na only in 1995 [4], thanks to the advances in laser cooling (see chap. 2) of alkali and vacuum technology.

In order to have an estimate of the temperature T_C needed for condensing, we can consider densities usually achievable in experiment: $n = 10^{13} - 10^{15}\,\mathrm{atoms/cm^3}$. Quantum phenomena emerge when the wavefunctions of the different atoms start to overlap. From Heisenberg *uncertainty principle* $\Delta x \cdot \Delta p \geq \hbar/2$, using $\Delta x \simeq n^{-1/3}$ and (under the assumption of non-interacting gas) the kinetic energy $k_B T = \Delta p^2/2m$, we have for a phase-space density $\Delta x \cdot \lambda_{dB} \simeq 1$ (λ_{dB} is the atom *de Broglie* wavelength):

$$T_C \simeq \frac{\hbar^2 n^{2/3}}{m k_B} = 20 - 2000\,\mathrm{nK} \tag{3.6}$$

Due to the extremely low temperature required it should be clear now why laser cooling (section 2.1) was a necessary step toward the BEC, but cannot be sufficient.

The conditions leading to BEC formation can be better calculated by taking into account the actual traps for cold particles. Usual traps are realized magnetically (section 2.3) or optically

(chapter 2.5), and are either harmonic over the distances occupied by the ultracold cloud (with oscillation frequencies along the three axes ν_x, ν_y, ν_z), or box-like in up to two dimensions. The density of states in a trap depends strongly on its shape. In the following, unless stated, the only particles we deal with will be atoms.

Let us first consider the case of free particles in a box of dimensions L_x, L_y, L_z. The *cavity modes* are those wavelengths satisfying $\lambda_i = 2L_i/n_i$, where n_i are positive integers and $i = x, y, z$. If a particle is contained in the box, these are the only allowed wavelengths for its wavefunction, as the particle density has to vanish at the walls. From the wavelength-momentum relation of *de Broglie* $\lambda_i = h/p_i$, and the energy for a free particle $\epsilon = p^2/2m$ we get $\epsilon = h^2\left(n_x^2 + n_y^2 + n_x^2+\right)/8mV^{2/3}$ where $V = L_xL_yL_z$ is the volume; then the number of states $G(\epsilon)$ of energy less than ϵ, and the density of states $g(\epsilon)$ are[3]:

$$\begin{aligned} G(\epsilon) &= \frac{1}{8}\cdot\frac{4\pi V}{3}\left(\frac{8m\epsilon}{h^2}\right)^{3/2} \\ g(\epsilon) &= 2\pi V\left(\frac{2m}{h^2}\right)^{3/2}\sqrt{\epsilon} \end{aligned} \tag{3.7}$$

For a harmonic quantum oscillator the energy is given by $\epsilon = (n_x + 1/2)\,\hbar\omega_x + (n_y + 1/2)\,\hbar\omega_y + (n_z + 1/2)\,\hbar\omega_z$. Using this relation eqn. 3.7 yields:

$$\begin{aligned} G(\epsilon) &= \frac{\epsilon^3}{6\hbar^3\omega_x\omega_y\omega_z} \\ g(\epsilon) &= \frac{\epsilon^2}{2\hbar^3\omega_x\omega_y\omega_z} \end{aligned} \tag{3.8}$$

The above formulas 3.7, 3.8 can be derived also for a number of dimensions different than 3, and an extensive literature exists already on the subject (see only [43]).

We will finish here by using eqn. 3.4, 3.7 and 3.8 to derive the behaviour of the cold gas around the *critical, or transition temperature* for condensation, T_C. If we define it as the lowest temperature at which we **do not** have macroscopic occupation of the lowest energy state, we can approximate the sums over the allowed (excited) energy levels with integrals, and add a term for the atoms in the lowest level. The total atom number must then satisfy:

$$N = n_0 + \int_{\epsilon_0}^{\infty} n(\epsilon)\,d\epsilon = \frac{1}{e^{(\epsilon_0-\mu)/k_BT} - 1} + \int_{\epsilon_0}^{\infty}\frac{g(\epsilon)d\epsilon}{e^{(\epsilon-\mu)/k_BT} - 1} \tag{3.9}$$

where we changed the discrete index s of g_s and ϵ_s, eqn. 3.4 to the continuous variable ϵ in $g(\epsilon)$ in the integrals. From eqn. 3.4 we get (considering the atoms in the lowest level $n_0 \gg 1$, and also $N \gg 1$):

$$e^{(\epsilon_0-\mu)/k_BT} = 1 + \frac{1}{n_0} \quad \Rightarrow \quad \frac{\epsilon_0 - \mu}{k_BT} \simeq \frac{1}{n_0} \tag{3.10}$$

Experimentally realized condensates have a final number of condensed atoms of $n_0 = 10^3 - 10^7$, so already at the **beginning** of the condensation process we are allowed to make the assumption leading to eqn. 3.10; this tells us that we make a minimal approximation if we change the lowest integration bound in eqn. 3.9 to $\epsilon = 0$ and the exponential at the denominator to e^{ϵ/k_BT}. This allows to calculate explicitly the integral for the cases of eqn. 3.7 and 3.8 [43]. We get T_C by requiring that all the atoms still be in the excited levels. For a box and harmonic potential:

$$\begin{aligned} \text{Box:} \quad T_C &\simeq 3.31\frac{\hbar^2N^{2/3}}{k_BmV^{2/3}} \\ \text{Oscillator:} \quad T_C &\simeq 0.94\hbar\bar{\omega}N^{1/3}/k_B \quad \text{with} \quad \bar{\omega} = \sqrt[3]{\omega_1\omega_2\omega_3} \end{aligned} \tag{3.11}$$

[3] we assume here a continuous distribution; the assumption is valid only for high energies, or n_x, n_y, $n_z \gg 1$

Using typical experimental numbers of $N = 10^5$ and trap parameters $\omega_x = 2\pi \cdot 10$ Hz and $\omega_y = \omega_z = 2\pi \cdot 10^3$ Hz, the value for the critical temperature is $T_C = 450\,\mathrm{nK}$. The number of condensed atoms is given by:

$$\begin{aligned} \text{Box} \quad n_0 &\simeq N\left(1 - \left(\frac{T}{T_C}\right)^{3/2}\right) \\ \text{Oscillator} \quad n_0 &\simeq N\left(1 - \left(\frac{T}{T_C}\right)^{3}\right) \end{aligned} \tag{3.12}$$

Below T_C the number of atoms in the lowest level represents a significant fraction of N: we have a *quantum phase transition*. The situation for two standard systems is plotted in fig. 3.2.

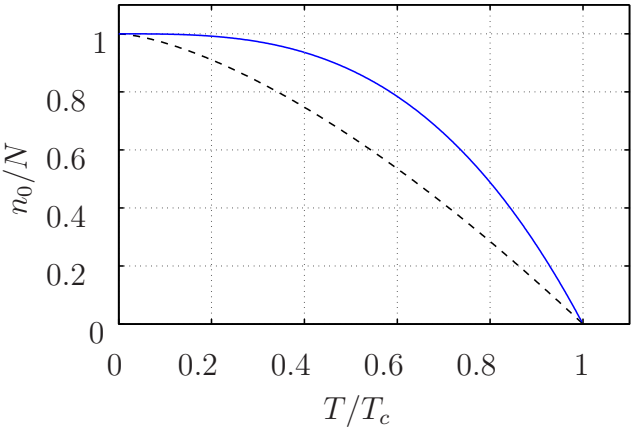

Figure 3.2: Fraction of condensed atoms in a 3D harmonic (blue, continuous curve) and in a 3D box-like (black, dashed curve) trap, plotted over temperature in units of T_c.

3.3 The interacting gas: mean field description

The above considerations are only valid in the case of non-interacting particles, but in reality we have to consider how atoms interact with each other. Alkali have typically scattering lengths a_s of ~ 100 times the atomic radius[4]; simplifications in calculating the interaction potential are possible thou. We deal with extremely low energies and at densities $n = 10^3 - 10^5\,\mathrm{atoms/cm^3}$, where the *gas parameter* g_s obeys the relation $\sqrt[3]{g_p} \equiv d_0 a_s = \sqrt[3]{n} a_s = 0.01 - 0.05$, which means that the atoms are separated in average much more than the interaction range (d_0 is the particle spacing).

The problem of describing N condensed bosons interacting with each other, and subject to the external potential $V(\boldsymbol{r})$ has been solved and is nowadays well known; the Hamiltonian describing the system is [55, 56]:

$$\hat{H} = \int \left\{ \hat{\Psi}^\dagger(\boldsymbol{r}) \left[-\frac{\hbar^2}{2m}\nabla^2 + V(\boldsymbol{r}) \right] \hat{\Psi}(\boldsymbol{r}) + \frac{1}{2} \int \hat{\Psi}^\dagger(\boldsymbol{r}) \hat{\Psi}^\dagger(\boldsymbol{r}') U(\boldsymbol{r} - \boldsymbol{r}') \hat{\Psi}(\boldsymbol{r}) \hat{\Psi}(\boldsymbol{r}') \cdot d\boldsymbol{r}' \right\} \cdot d\boldsymbol{r} \tag{3.13}$$

where $\hat{\Psi}(\boldsymbol{r})$ and $\hat{\Psi}^\dagger(\boldsymbol{r})$ denote, respectively, the boson field operators for annihilation and creation and $U(\boldsymbol{r} - \boldsymbol{r}')$ the interparticle interaction potential. Using the standard commutation relations:

$$\left[\hat{\psi}(\boldsymbol{r}), \hat{\psi}^\dagger(\boldsymbol{r'})\right] = \delta(\boldsymbol{r} - \boldsymbol{r}') \qquad \left[\hat{\psi}(\boldsymbol{r}), \hat{\psi}^\dagger(\boldsymbol{r'})\right] = 0 \tag{3.14}$$

[4] For ultracold alkali gases we can approximate the interaction by considering only s-wave scattering.

we can easily write down[5] the equation for the time evolution of $\hat{\Psi}$:

$$i\hbar\frac{\partial}{\partial t}\hat{\Psi}(\boldsymbol{r},t) = \left[\hat{\Psi},\hat{H}\right] = \left[-\frac{\hbar^2\nabla^2}{2m} + V(\boldsymbol{r}) + \int \hat{\Psi}^\dagger(\boldsymbol{r}',t)V(\boldsymbol{r}'-\boldsymbol{r})\hat{\Psi}(\boldsymbol{r},t)\cdot d\boldsymbol{r}'\right]\hat{\Psi}(\boldsymbol{r},t) \tag{3.15}$$

The basic idea to proceed from here is to use a *mean-field* description of the system, as first done by Bogoliubov [6]. Therefore we decompose the time-dependent field operator into $\hat{\Psi}(\boldsymbol{r},t) = \Phi(\boldsymbol{r},t) + \hat{\Psi}'(\boldsymbol{r},t)$, where Φ is a complex function[6] describing the condensate fraction, and $\hat{\Psi}'$, called the *depletion*, is an operator for the remaining particles. We neglect the depletion (in a rarefied-gas BEC the condensate fraction can be easily of 90%). Respecting the limits outlined above (on density and energy), we can approximate the interaction potential as a point-like one, $U(\boldsymbol{r}'-\boldsymbol{r}) = g\,\delta(\boldsymbol{r}'-\boldsymbol{r})$, with an amplitude $g = 4\pi\hbar^2 a_s/m$. This leads us to the well known *Gross-Pitaevskii* (GP) equation[57, 58, 59]:

$$i\hbar\frac{\partial}{\partial t}\Phi(\boldsymbol{r},t) = \left(-\frac{\hbar^2\nabla^2}{2m} + V(\boldsymbol{r}) + g\left|\Phi(\boldsymbol{r},t)\right|^2\right)\Phi(\boldsymbol{r},t) \tag{3.16}$$

This equation describes the behaviour of a condensate at low or zero temperature, under the conditions that the atom number $N \gg 1$. It can be employed to study how the BEC behaves over distances d much bigger than the mean interparticle separation $d \gg n^{-1/3}$.

The ground state of the condensate can be recovered with variational methods. For specific stationary solutions of the type $\Phi(\boldsymbol{r},t) = \phi(\boldsymbol{r})\exp(-i\mu t/\hbar)$ the eqn. 3.16 leads to:

$$\left(-\frac{\hbar^2\nabla^2}{2m} + V(\boldsymbol{r}) + g\left|\phi(\boldsymbol{r})\right|^2\right)\phi(\boldsymbol{r}) = \mu\phi(\boldsymbol{r}) \tag{3.17}$$

That can be solved or numerically computed for the various potentials V acting on the atoms. The chemical potential μ represents the interaction energy, as can be seen by taking the case of a uniform condensate ($\nabla^2\psi = 0$ and $V = 0$). In the limit of weak interaction $g \to 0$ we recover the Schrödinger equation for a particle in an external potential.

3.4 The Thomas-Fermi approximation

Equation 3.17 can be further simplified in particular situations: when the particle number is high, or for sufficiently high interaction U_0. In the latter case the interaction term dominates, and the contribution of the kinetic energy in 3.17 can be neglected. This approximation describes quite well the behaviour of the BEC at the center of the cloud, but it fails on its border, where the density $n = |\phi|^2$ goes to zero. It is quite easy to solve, as all the derivatives are dropped from it, and it returns:

$$n(\boldsymbol{r}) = |\phi|^2 = \frac{[\mu - V(\boldsymbol{r})]}{g} \qquad \text{and} \qquad V(\boldsymbol{r_0})|_{\phi=0} = \mu \tag{3.18}$$

where the second equation defines the edges of the cloud. For harmonic confinement along the axis $j = x, y, z$ we have $r_{0,j} = \sqrt{2\mu/(m\omega_j^2)}$. With such an approximation (known as the *Thomas-Fermi* approximation , TF), plus the normalization condition on the overall atom number, the basic parameters of the cloud in the trap can be recovered (see again [43] and [60]).

The TF approximation is more precise with a high atom number and in isotropic traps, i.e. cases in which the BEC *surface/volume* ratio is low.

[5] Thanks to Shahpoor Saeidian of the Cold Atoms Theory Group at the P.I. Heidelberg for reminding me the fun of playing with operators.

[6] The operator can be changed to a complex function in the limit of high atom number, where $N \simeq N-1$

3.4.1 The healing length

An important parameter for a condensate is the *healing length*, ξ.

Assume to have a BEC that extends indefinitely in the y and z directions and is homogeneous along those directions; along x we have a potential that is infinite for $x < 0$, and constant and null for $x \geq 0$. The condensate wavefunction has to vanish at $x = 0$, while for $x \gg 0$ it is constant, say $\phi(x \to \infty) \equiv \phi_0$. The distance over which it spans from 0 to ϕ_0 can be estimated by the help of the Heisenberg uncertainty principle. If this distance is ξ, then the kinetic energy associated with it can be equated with the interaction energy where $\phi(x)$ is at equilibrium (at $x \gg 0$):

$$\frac{\hbar^2}{2m\xi^2} = ng \qquad \text{or} \qquad \xi = d_0\sqrt{\frac{d_0}{6a_s}} \tag{3.19}$$

As the interparticle spacing d_0 is in normal traps around two orders of magnitude bigger than the scattering length a_s, usually the inequalities $d_0 \gg \xi \gg a_s$ hold. ξ can be interpreted as the distance required to the BEC to *recover* from the zero value boundary condition, and is thus called *healing length*. When analyzing the density of a BEC in an elongated trap ξ is usually much smaller than the imaging resolution (that in our case is approx $3\,\mu$m).

3.5 Dynamics of the condensate

The dynamics of a condensate is fully contained in the treatment of Bogoliubov [6], and can be recovered from the GP equation 3.17.

Of particular interest is the case of local excitations, propagating with the *sound velocity* inside the condensate and eventually giving rise to *dark* or *bright solitons* [61, 62].

Another phenomenon observed is the quantization of the rotational field, that manifests itself with a regular lattice of *vortices*. We will not deal at this point with such effects, that have been already investigated in numerous specific works [63].

Of more interest for us are are the collective modes of the condensate. They can be exploited experimentally to test some of the basic parameters of the condensate and of the trap.

3.5.1 BEC oscillations

If we have a BEC in a trap and suddenly displace it along one of its symmetry axes, the BEC will start to oscillate with the trapping frequency along that direction. The observation of this oscillation (eventually after release and a sufficient long time of flight, *TOF*) is the simplest way of measuring the confinement of the trap. In order to measure the longitudinal confinement $\nu_\parallel$ we have another method: changing the Ioffe field B_x (or the distance from the chip) we obtain a modulation of $\nu_\perp$, causing the BEC to be squeezed, and subsequently expanding and collapsing along the x axis, with an oscillation behaviour named *breathing mode*.

In order to derive the oscillation frequencies relative to the trap confinement used we start by writing the GP time-dependent equation, as done in eqn. 3.16. Then, following [64, 56], we use the density and introduce the velocity field $\boldsymbol{v}$:

$$n(\boldsymbol{r},t) = \left|\Phi(\boldsymbol{r},t)^2\right| \qquad \boldsymbol{v}(\boldsymbol{r},t) = \frac{[\Phi^*(\boldsymbol{r},t)\nabla\Phi(\boldsymbol{r},t) - \nabla\Phi^*(\boldsymbol{r},t)\Phi(\boldsymbol{r},t)]}{i\cdot 2\,m\,n(\boldsymbol{r},t)} \tag{3.20}$$

and plug them into equation 3.16, which yields the following set of equations:

$$\begin{cases} \dfrac{\partial}{\partial t}n + \nabla(\boldsymbol{v}n) = 0 \\[2ex] m\dfrac{\partial}{\partial t}\boldsymbol{v} + \nabla\left(\delta\mu + \dfrac{m\boldsymbol{v}^2}{2}\right) = 0 \end{cases} \quad \text{with} \quad \delta\mu \equiv -\mu + V + gn - \frac{\hbar^2}{2m\sqrt{n}}\nabla^2\sqrt{n} \tag{3.21}$$

The eqn. 3.21 are known as *hydrodynamic equations*, because of their similarity to the equations describing the flow of classic fluids. In the TF limit the last term in the definition of $\delta\mu$ (kinetic energy contribution) can be neglected.

From eqn. 3.21, provided $|n| > 0$, it follows that the superfluid motion is irrotational. This has consequences for the flow around vortexes [56]. Considering small deviations from equilibrium periodic in time $\delta n(\boldsymbol{r})e^{-i\omega t} = n(\boldsymbol{r},t) - n_{0,eq}(\boldsymbol{r})$ and small velocity fields $\boldsymbol{v}$, eqn. 3.21 can be linearized and yields:

$$\omega^2 \delta n(\boldsymbol{r}) = \nabla \cdot (n_{0,eq} \nabla \delta\mu) \tag{3.22}$$

From this, in the limit of constant external potential V, the velocity of sound waves in the condensate can be recovered [6].

In the TF limit (interaction energy much higher than kinetic energy) $\nabla\delta\mu$ simplifies greatly. Additionally, if we consider the x axis symmetry of usual magnetic traps, in which the potential can be expressed as:

$$V(x,y,z) = \frac{1}{2}m\left(\omega_\perp^2 r^2 + \omega_\parallel^2 x^2\right) \equiv \frac{1}{2}m\omega_\perp^2(r^2 + \lambda^2 x^2) \qquad \text{with} \qquad \begin{cases} \lambda \equiv \omega_\parallel/\omega_\perp \\ r \equiv \sqrt{y^2+z^2} \end{cases}$$

we can then write:

$$\omega^2 \delta n = -\frac{1}{2}\omega_\perp^2 \nabla\Big[(r_{0,eq}^2 - r^2) + \lambda^2(x_{0,eq}^2 - x^2)\Big]\nabla\delta n \tag{3.23}$$

where $r_{0,eq}$ is the transversal equilibrium radius of the BEC, and $x_{0,eq}$ its longitudinal dimension. For isotropic harmonic traps the general solution is a radial term multiplied by a spherical harmonic. For anisotropic confinement the equation can be reconducted to the previous case with a proper rescaling of the axes accompanied by a gauge transform for the momentum [65].

In the common cases of axial symmetry (*cigars* and *pancakes*) we have $\delta n = |\boldsymbol{r}|^n Y_{lm}(\theta,\psi)$ for $m = \pm l$ and $m = \pm(l-1)$, with the respective dispersion relations

$$\omega^2(m = \pm l) = l\omega_\perp^2 \qquad \text{and} \qquad \omega^2\big(m = \pm(l-1)\big) = \big[(l-1) + \lambda^2\big]\omega_\perp^2 \tag{3.24}$$

The first excitation we are interested in is the *dipole mode* with $l = 1$. As can be seen the oscillation frequencies are the same as the trap frequencies: the whole BEC moves then in the trap with the periodicity of a point-like particle.

Another collective motion is the *quadrupole mode*, with $l = 2$. For cigar-like trapping ($\lambda \ll 1$) eqn. 3.24 give the frequencies $\omega_1 = \sqrt{2}\omega_\perp$ and $\omega_2 = \omega_\perp$. Then we have the solutions for $m = 0$ [64] $\omega_3 = \sqrt{5/2}\omega_\parallel$ and $\omega_4 = \sqrt{2}\omega_\perp$. It is precisely the mode at ω_3 that gives us the necessary information on the longitudinal confinement (as done in section 10.3); for its dynamic pattern it is referred to as *breathing mode*.

3.5.2 Free expansion

The procedure of rescaling the axes with the time-dependent factors $b_x(t), b_y(t), b_z(t)$ can be applied also in presence of a harmonic time-dependent potential $V = \frac{1}{2}m\big[\omega_x^2(t)x^2 + \omega_y^2(t)y^2 + \omega_z^2(t)z^2\big]$. Moreover, with the appropriate gauge transformation in the momentum operator (as done in [65] or [66, 55, 67]) we can follow the evolution in time for every chosen coordinate $x_1(t) = b_x(t)x_1(0)$, $y_1(t) = b_y(t)y_1(0)$, $z_1(t) = b_z(t)z_1(0)$. This is valid also in the particular case of the cloud edge (telling us its spatial extension), when the trap is switched off instantaneously. The b_j ($j = x,y,z$) parameters have to satisfy:

$$\ddot{b}_j = \frac{\omega_j^2(0)}{b_j b_x b_y b_z} - \omega_j^2(t) b_j \qquad b_j(0) = 1 \qquad \dot{b}_j(0) = 0 \tag{3.25}$$

where the initial values on the b_j and on their derivative have been fixed by the equilibrium condition. For the case of free expansion ($\omega_j = 0$ for $t \geq 0$) from a cigar-shaped trap ($\omega_y = \omega_z \equiv \omega_\perp \gg \omega_\parallel \equiv \omega_x$) using the time variable $\tau = \omega_\perp(0)t$ and the parameter $\lambda = \omega_\parallel(0)/\omega_\perp(0) \ll 1$ we have in first approximation:

$$b_\perp(\tau) = \sqrt{1+\tau^2} \qquad b_\parallel(\tau) = 1 + \lambda^2\left[\tau \arctan\tau - \log\sqrt{1+\tau^2}\right] \tag{3.26}$$

If for $t = 0$ the confined BEC has the aspect ratio $\rho = r_{0,\parallel}/r_{0,\perp} = \omega_\perp(0)/\omega_\parallel(0) \equiv \lambda^{-1} \gg 1$, going in the limit of $\tau \gg 1/\lambda$, or $t \gg \omega_\parallel(0)^{-1}$, we have $\rho \simeq \lambda\big(\pi/2 + \log\tau\big) \ll 1$, effectively *inverting* the aspect ratio. This is one of the signatures that confirmed in the first experiments a BEC was produced. Experimentally this is observable only for traps with a sufficiently high longitudinal confinement, otherwise the cloud becomes too diluted to be observed. In the tight chip traps realized in our experiments we have $\nu_\perp \simeq 10^2 \pm 10^4$ Hz and $\nu_\perp \simeq 0 \pm 10$ Hz; with such confinements the aspect-ratio inversion is practically never reached; one exception is represented by traps close to the surface, where the *disorder potential* (see section 7.4.1) can fragmentate the BEC longitudinally in various *blobs*, with longitudinal trapping frequencies that can reach $\nu_\parallel = 100$ Hz (see sec. 11.2.3) and allow a faster evolution of ρ.

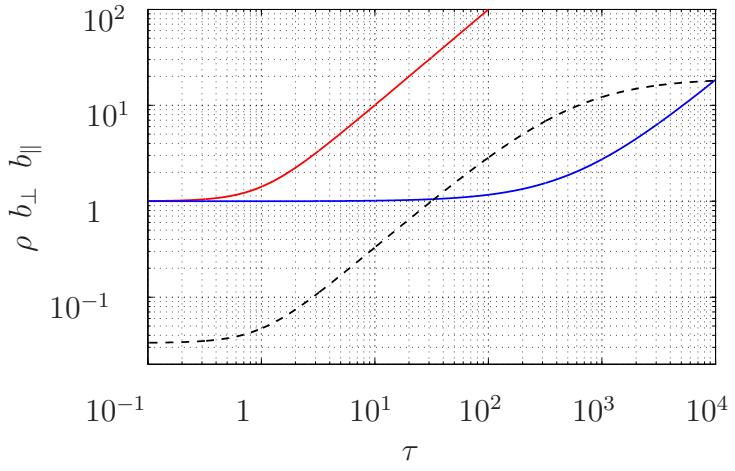

Figure 3.3: Aspect ratio of the interacting BEC cloud (black dashed curve), and its spatial extension scaling factors $b_\perp$ (red curve) and $b_\parallel$ (blue curve) for $\lambda = 1/30$. $b_\perp$ starts to rise around $\tau = 1$, while $b_\parallel$ at $\tau = \lambda^2$; in this time frame the observable aspect ratio ρ inversion takes place.

Chapter 4

Exotic ultracold matter

Among the many properties of a BEC the most notable one is probably the existence of a constant quantum-mechanical phase of its wave field; this is true throughout its whole spatial extension, that depending on atom number and trap frequencies can reach the mm scale.

However, quantum degenerate gases not necessarily are BECs. We relate here on situations in which the phase coherence is lost (quasicondensates), or in which the mutual interaction between atoms is so high that the single atoms are spatially localized and under a certain point of view behave as fermions (Tonks-Girardeau gas). Moreover, in presence of periodic potentials a finite excitation gap can be observed: we have a glassy system (Mott insulator).

4.1 1D [quasi]condensates, Tonks-Girardeau gas

If we increase the transversal confinement $\omega_\perp$ while keeping the longitudinal one $\omega_\parallel$ sufficiently low, as well as the total atom number N, we reduce the interaction energy and we get to the point where the chemical potential $\mu < \hbar\omega_\perp$. In such a situation the transversal atomic motion is effectively restricted to the harmonic potential zero-point oscillation, while the density distribution is the Gaussian one of the ground state: we are in an effective 1D regime for the BEC.

For ^{87}Rb and trapping frequencies regularly attainable in our chips $\omega_\perp \simeq 2\pi \cdot 10$ kHz the radial size of the waveform is $l_\perp = \sqrt{\hbar/m\omega_\perp} \simeq 100$ nm; as we are in the limit $l_\perp \gg a_s$ (with a_s being the scattering length), the interaction between atoms is still of 3D character. In this situation the system can be described by an **effective** 1D mutual interaction term that is obtained by averaging the interaction over the transversal density distribution [68, 69, 70]:

$$g_{1D} = \frac{2\hbar^2 a_s}{m l_\perp^2} \tag{4.1}$$

In order to describe the various regimes that the atoms are subject to in traps of 1D geometry it is useful to consider the following parameters:

$$T_D = N\hbar\omega_\parallel \qquad T_\phi = T_D \frac{\hbar\omega_\parallel}{\mu} \tag{4.2}$$

where n_{1D} is the 1D atom density (the other variables have already been introduced, and are listed in app. A). The first temperature, T_D (expressed in energy), is called the degeneracy temperature. Below T_D we start to accumulate particles in the lowest quantum oscillator levels (along the x direction); we consider only the situation where $T \ll T_D$.

Another important parameter is the temperature T_ϕ. It can be shown [70] that a gas trapped in 1D is a true condensate at $T = 0$. When we increase T phase fluctuations start to arise. The *phase coherence length* l_ϕ can be defined as the distance between two points in the condensate

below which we can assume phase coherence is kept; at $T = T_\phi$ it is as long as the condensate, while for higher temperatures it has a value of:

$$l_\phi(T) \simeq R_{TF} T_\phi / T \qquad R_{TF} = \sqrt{\frac{\mu}{m\omega_\parallel}} \tag{4.3}$$

where R_{TF} is the half length of the condensate. Strictly speaking the BEC does not exist above T_ϕ; although the density is still homogeneous, we can think of our atom cloud as composed of various condensates, with well defined phase coherence between points distant less than about l_ϕ. This quantum degenerate gas has been named *quasicondensate*. From the value of $\mu = \hbar\omega_\parallel \left(\frac{3N\alpha}{4\sqrt{2}}\right)^{2/3}$ and T_ϕ in eqn. 4.2 we get the transition temperature between condensate and quasicondensate, as shown in fig. 4.2 with the blue line.

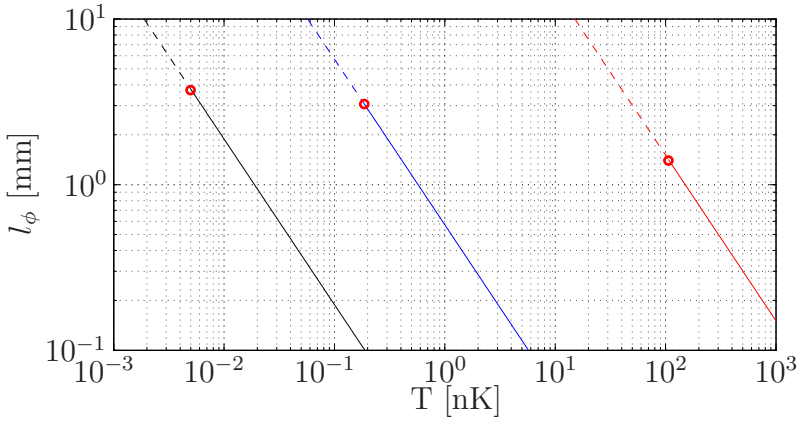

Figure 4.1: Coherence length l_ϕ in dependence of the temperature. Lines correspond to different traps and atom numbers; red circles indicate a coherence length as big as the atom cloud: $l_\phi = 2 \cdot R_{TF}$.
Red: typical copper $\boldsymbol{Z}$ trap, $\nu_\perp = 2\pi \cdot 1\,\text{kHz}$, $\nu_\parallel = 2\pi \cdot 20\,\text{Hz}$, $N_{atoms} = 150000$.
Blu: typical chip trap, $\nu_\perp = 2\pi \cdot 5\,\text{kHz}$, $\nu_\parallel = 2\pi \cdot 0.5\,\text{Hz}$, $N_{atoms} = 50000$.
Black: tight chip trap, with low atom number $\nu_\perp = 2\pi \cdot 20\,\text{kHz}$, $\nu_\parallel = 2\pi \cdot 0.1\,\text{Hz}$, $N_{atoms} = 10000$.

However, in order to really understand what happens to the phase distribution (as well as to the momentum) which describes the trapped ultracold quantum gas, we have to investigate the nature of the interaction between the atoms. In this context particular relevance is assumed by the following quantities:

$$\alpha = \frac{m g_{1D} l_\parallel}{\hbar^2} \qquad \gamma = \frac{m g_{1D}}{\hbar^2 n_{1D}} \tag{4.4}$$

α can also be expressed as $\alpha = l_\parallel / r_g$, where $l_\parallel$ is the zero-point oscillation length, and $r_g = \hbar^2 / m g_{1D}$ is the characteristic interaction length for two particles (it is the distance at which the zero-point kinetic energy compensates the interaction); α defines the relation between the interaction and the harmonic confinement. Two are the limits of interest for us:

- For $\alpha \simeq N^{-1}$ the interaction energy is comparable to the zero-point oscillator energy. Lower values of α result in a freezing of the BEC dynamics also along x, and the BEC longitudinal density has a Gaussian distribution; for chip traps this situation is not typical[1]. In the opposite limit, namely for $\alpha \gg N^{-1}$, we are working with a Thomas-Fermi BEC.

[1] We are limited by the detection sensitivity of a few $atoms/\mu$m; on the contrary in experiments with optical lattices as reported in [71] multiple 1D BEC are sampled at the same time and less atoms (in each single cigar) can be detected.

- For sufficiently high values of α the mutual interaction becomes dominant; in that limit the cold atoms behaviour depends on γ. If we want $\gamma < 1$ (limit for the TF or weak interaction regime), then we can find a minimum atom number N^* at which the inequality is satisfied: $N^* = \alpha^2$ [70].

The parameter $\gamma = U/K$ expresses the ratio between the interaction energy per particle $U = n_{1D} g_{1D}$ and the kinetic energy of a particle confined within $r = 1/n_{1D}$, so $K \simeq \hbar^2 n_{1D}^2/m$. It defines whether the dynamics is dominated by the mutual interaction ($\gamma \gg 1$) or not.

In the first case it is energetically more convenient to localize the atoms than to have the wave-function of each of them spread across the whole trap: the atoms behave effectively as impenetrable particles and share no common phase. For this reason bosons are said to *fermionize*. Differently to Fermions there is no Pauli exclusion principle for the momentum, so that Δp is smaller for strongly interacting Bosons than for Fermions in an equivalent confinement regime [71]. This quantum state of the matter is the so-called *Tonks-Girardeau gas* (TG for short). Signatures of the TG phase are changes on the density statistics (because localization fluctuations are suppressed) and on the momentum distribution (an atom in the BEC is distributed along the whole length of the trap; for the uncertainty principle its momentum distribution is significantly narrower than that of each localized atom). Moreover together with the loss of a global phase there is a decrease in higher order correlations: this has as direct effect the reduction of 3-body losses, leading to an increased lifetime [72].

If we observe γ closely, we see it is bigger for lower densities n_{1D}. This behaviour emerges from the 1D nature of the confinement. It is due to the slower decrease in U than in the kinetic energy K when n_{1D} is reduced. This is also the reason why it is so difficult to observe this quantum regime: with the achievable trapping frequencies of about $\nu_\perp = 10\ kHz$, we have a TG gas for $n_{1D} \ll 1$ atoms/μm, which is a density not detectable with our setup. There are however some tricks that can be employed to improve the situation (see for example sec. 4.2). A Tonks-Girardeau gas of ultracold ^{87}Rb atoms has been observed recently [71].

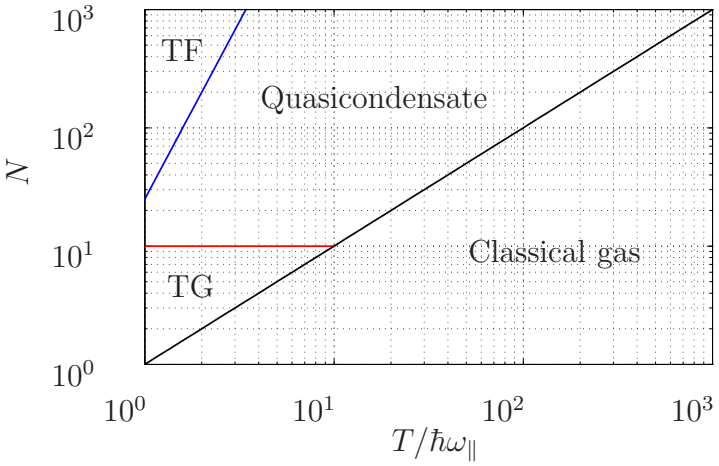

Figure 4.2: Diagram of states for a cold gas in 1D traps for $\alpha = 10$. True TF (Thomas-Fermi) condensate exists only at sufficiently low temperature, while Tonks-Girardeau gas is present when the density is so low that the interaction between atoms becomes dominant. The lower left part of the graph represents the atoms above degeneracy temperature T_D.

4.1.1 A word on weaker confinement

Before going on with other aspects of 1D and quantum degenerate gases, we would like to look at the case of weaker confinement. When analyzing the phases of the cold gases in 1D trapping we

assumed to be in the limit $\mu \ll \hbar\omega_\perp$. In the experiment we are often in the condition where μ is of the same order of $\hbar\omega_\perp$. In such a situation we do not really have 1D confinement, and the gas parameters (chemical potential μ, cloud size and density) do not follow the formulas derived for a 3D or a 1D case. It has been found [73, 74] that the condensate in such a transition regime can be described as an effective 1D (quasi)condensate, with a chemical potential of

$$\mu_{l.e.} = \hbar\omega_\perp \sqrt{1 + 4a_s n_{1D}} \tag{4.5}$$

where we used the subscript $l.e.$ (local equilibrium) to emphasize the fact that we are working with quasicondensates that do not possess a global phase, and whose measurables depend on the variation of the trapping potential along x : $\mu_{l.e.}(x) = \mu - V(x)$. The equation 4.5 will be used later (section 11.2.3) to derive the local trapping potential depending on the atom density $n_{1D}(x)$.

4.2 Mott insulator

If we modulate periodically the trapping potential along x with a modulation V_0 bigger than μ, the atoms are trapped in the local minima of the modulation, and show a probability to escape to neighbouring sites, with a tunneling time τ, and an associated energy J. If V_0 is sufficiently high, we can assume the atom is effectively trapped, and would have a momentum spread Δp_x defined by the size Δx of the local ground state.

Adding a second atom costs a finite energy U, a value fixed by the mutual interaction per particle and dependent on the longitudinal trapping frequency of the local potential $\nu_\parallel$. The two main consequences are:

- A finite energy gap is present, and in order to move an atom from a site to the neighbouring one we have to use energy. The superfluidity disappears, and we are left with a *Mott insulator* (MI), in which each atom is fully localized. In such a case the energy due to the localization of the atom in the local minimum (zero-point kinetic energy) is much smaller than the interaction energy per particle: $K \ll U$.

- The lowest energy state for the system is the one in which each site is occupied by the same integer number of atoms (*commensurate filling*). The phase coherence of the BEC condensate is completely lost, in favour of a quenching in the number oscillation: a *squeezed state* complementary to the phase-coherent superfluid.

Figure 4.3: Particles in a periodic potential. The ground level (in green) shifts to higher energy (red line), because of mutual interaction generating a finite energy gap U; this stops particles from hopping freely. Excitation is possible if, for example, a potential tilt compensates for U (right image).

The ability of the MI state to minimize the number fluctuation between different sites can be exploited in the preparation of controlled ensembles of atoms; this is a situation desirable for some quantum information processing schemes, where for example one single atom is required in each potential minimum.

The physics of a Bose gas in a sinusoidal potential has been investigated both theoretically and experimentally[75, 76, 77, 78, 79, 80, 81, 82, 8, 83]; it is described by a one-dimensional *Mathieu equation* and its solutions are referred to as *Wannier functions*.

A stationary system of weakly interacting bosons in 1D traps, with a sinusoidal potential modulation along the longitudinal x axis can be described by the GP equation 3.17, where we now have $V(\boldsymbol{r}(x)) = V_0 \sin(k_x x) + V_\parallel(x)$, with the leading term describing the periodic modulation of wave vector k_x plus a long-range confining term $V_\parallel$. The general solution $w(x)$ can be used to derive the important parameters of the system: the on site interaction energy for two atoms U, and the nearest neighbour tunneling J, that is the gain in kinetic energy due to that tunneling [77]. From another point of view [75] the system is equivalent to one with the Hamiltonian:

$$\hat{H} = -J \sum_{\langle ll' \rangle} \hat{b}_l^\dagger \hat{b}_{l'} + \frac{U}{2} \sum_l \hat{n}_l(\hat{n}_l - 1) + \sum_l \epsilon_l \hat{n}_l \tag{4.6}$$

where the indexes l, l' run on the lattice site number, $\langle ll' \rangle$ is used to indicate a sum over nearest neighbours and ϵ_l is an energy term that includes the effect of a slow varying potential (in the example above that giving longitudinal trapping $V_\parallel(x)$).

As natural energy unit we take the *recoil energy* $E_r(k_x) = \hbar^2 k_x^2 / 2m$. In the deep lattice limit $V_0 \gg E_r$, where each lattice site houses many *quasi-bound states*[2] the potential around the lattice minima can be approximated by that of harmonic oscillators of frequency $\nu_w = \sqrt{4E_r V_0}/\hbar$. In this limit each oscillator has a ground state that describes with a good accuracy the probability distribution for an atom (the time dependence has been left out):

$$w(x) = \sqrt[4]{\frac{a_w^2}{\pi}} \cdot e^{-a_w^2 x^2/2} \qquad \text{with} \qquad a_w = \sqrt{\frac{\hbar}{\nu_w m}} \tag{4.7}$$

with this solution the Mathieu equation can be solved analytically [79, 80, 81]. Using also as transversal distribution a Gaussian (strong transversal confinement compared to the chemical potential $h\nu_\perp \gg \mu$) and integrating [84] we get:

$$\begin{aligned} U &= g_{1D} \int |w(x)|^4 dx = 4\pi^{3/2} \frac{a_s}{a} \hbar \nu_\perp \left(\frac{V_0}{E_r}\right)^{1/4} \\ J &= \frac{4}{\sqrt{\pi}} E_r \left(\frac{V_0}{E_r}\right)^{3/4} \exp\left(-2\sqrt{V_0/E_r}\right) \\ r_{MI} &\equiv \frac{U}{J} \simeq 3.6 \cdot \nu_\perp a \frac{\exp\left(2\sqrt{V_0/E_r}\right)}{\sqrt{V_0/E_r}} \end{aligned} \tag{4.8}$$

The experimental parameters defining the values of J and U are the lattice step a_w, the peak-to-peak potential modulation V_0 and the transversal confinement $\nu_\perp$. The physic behaviour of the ultracold atomic sample is governed by the ratio r_{MI}. For $r_{MI} \simeq 1$ we are in the crossover between quasi-condensate (weak interaction limit, superfluid) and MI (strong interaction, glassy system). In 1D the exact crossover lies at $r_{MI} = 3.84$ for $\overline{n} = 1$, and $r_{MI} = 2.2 \cdot \overline{n}$ for $\overline{n} \gg 1$ (where $\overline{n}$ is the number of atoms per lattice minimum) [77]. Taking as example a lattice realized with a laser light close to resonance ($a = 780/2\,\text{nm}$ for Rb) and $\nu_\perp = 20\,\text{kHz}$, from fig. 4.4 we see that we need $V_0/E_r = 8.8$ for $\overline{n} = 1$ and $V_0/E_r = 16$ for $\overline{n} = 10$.

Recently some work has been devoted to the study of MI phases with more than one atom per site, $\overline{n} > 1$. If we have trapped atoms in the MI phase and increase the γ factor, novel and up to now unobserved phenomena can appear [85, 86, 87, 88]: the atoms can undergo a local TG-like transition in each lattice site and localize in spatially separated distributions.

[2] Although $w(x)$ is periodic, for times much shorter than the tunneling time we can think that a particle deposited in a single site does not tunnel out of it, and occupies locally defined states.

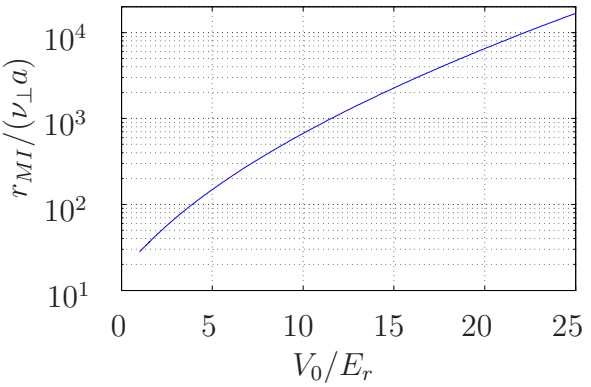

Figure 4.4: Dependence of $\frac{r_{MI}}{\nu_\perp a}$ on V_0/E_r . The exponential trend shows how fast the interaction becomes dominant with V_0 .

The magnetic lattice potential proposed in section 11.2.5, or the light potential discussed in chapter 12 can be used to investigate these regimes.

Part II

TECHNOLOGY

Chapter 5

The vacuum chamber

5.1 A double MOT chamber

The stainless steel chamber where we Bose-Einstein condense the atoms is based on a *double MOT* setup [89]: it is composed by two vacuum chambers separated by a differential pumping stage. As it has already been described in detail in [90, 91], we only shortly point out its main characteristics.

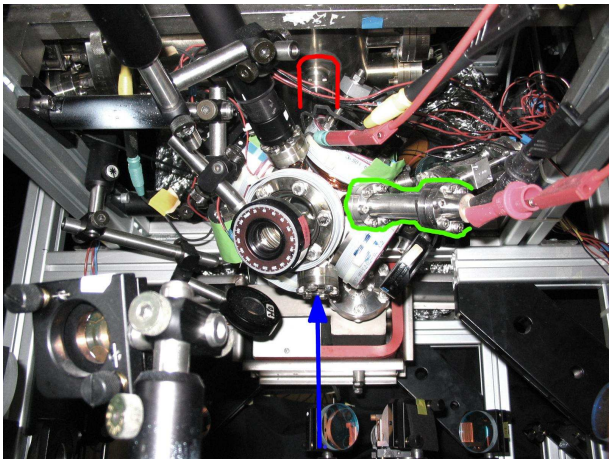

Figure 5.1: The lower MOT chamber. We outlined in green the dispenser position; the blue arrow indicates the direction of the push beam, while the thin nozzle is inside the upper red-marked region.

In the lower part there is a small chamber; here we have the Rb dispenser: a bar that upon ohmic heating releases atoms of Rb in gaseous form. Three laser beams, retroreflected by mirrors, and three couples of coils are used to generate a first MOT, to load and cool the atoms. The relatively small size of the chamber has the advantage that we can achieve high fields gradients with limited currents (no need of water cooling for quadrupole coils). A 20 l/s ion pump keeps the low pressure needed for the MOT to operate. The background gas loads continuously the MOT. The atoms need then to be transferred to the second MOT, where they will be condensed. For this purpose the radiation pressure of a laser beam outcoupled from a single mode optical fiber (output diameter $\varnothing \simeq 1.5\,\mathrm{mm}$) pushes them out of it, toward the upper MOT: we call it the *push beam*.

A long metal rod with a thin nozzle allows the cold atomic beam generated by the push beam to pass through, and limits the flow of background gas out of the lower chamber, to enable a pressure gradient.

In the center of the chamber, between the two MOTs, the feedthroughs for pressure measurement, valves required to open and evacuate the chamber, a 260 l/s ion pump and the 515 l/s

Titan sublimation pump are attached. We measure here a pressure under the lower gauge limit of $4 \cdot 10^{-12}$ mBar.

Finally, in the upper part, we have the chip, placed face-down on a specially designed holder (sec. 6.4). This positioning allows to observe the evolution of the BEC during free fall (*Time Of Flight*, or TOF imaging). The reflecting face of the chip is used to realize a *reflection MOT* [92, 93]. Good optical access is ensured by the small chamber size around the chip and by four $CF40$ (2 vertical and 2 for the 45° MOT beams) plus two $\varnothing = 65\,\text{mm}$ (vertical) windows.

Differently from the setup described in [90, 91], the upper chamber quadrupole coil is no longer in use. The magnetic field it produced is now generated by a copper structure in the mounting: the $\boldsymbol{U}$ (see sec. 6.4). The MOT can be loaded at about $2 - 4 \cdot 10^7$ atoms/s.

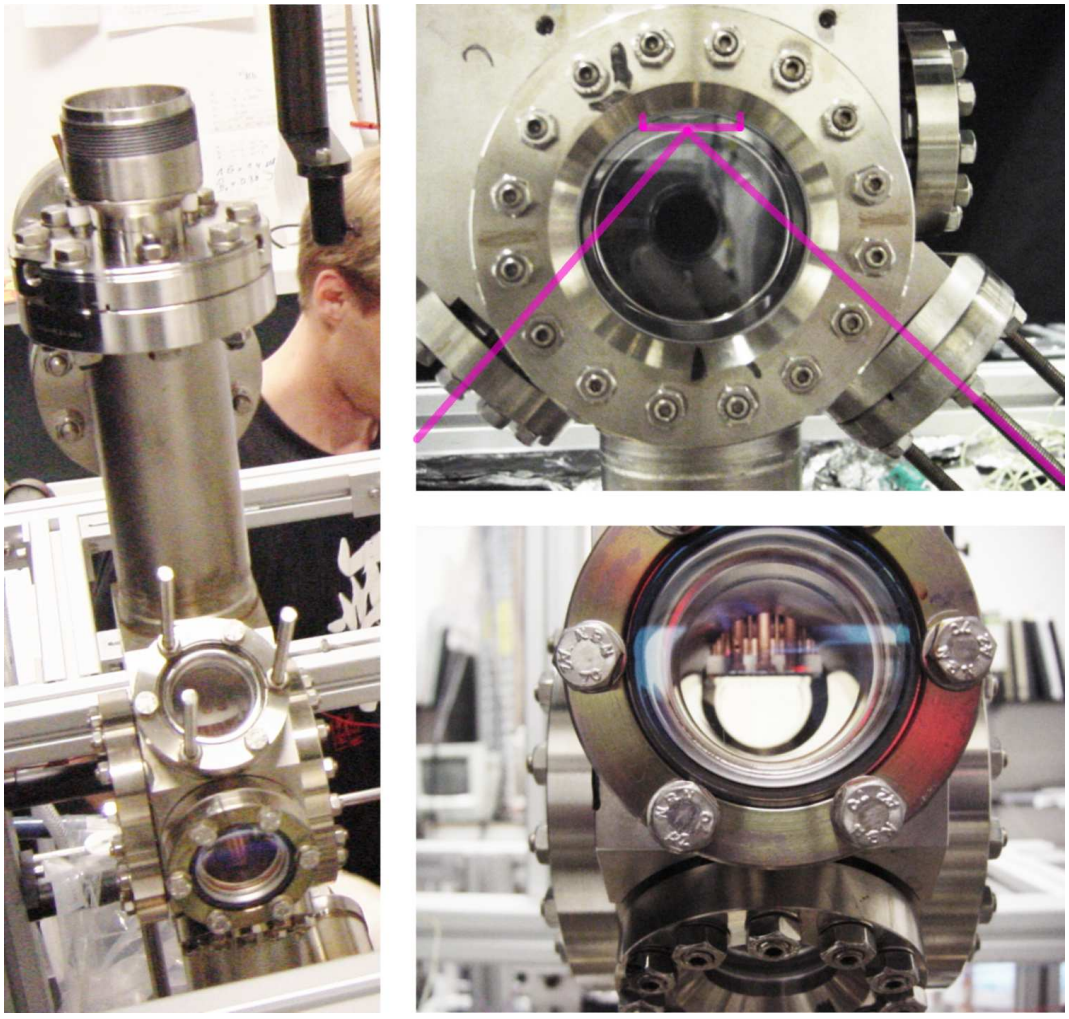

Figure 5.2: The bare chamber when the second chip was mounted: the upper MOT region is visible.
Left: top/side view of the chamber. The upper vacuum flange has electrical feedthroughs that are connected to the chip and the copper structures placed below it. The white ceramic in the chip mounting is visible from the upper window, on which three long screws provide support from one of the two quadrupole coils. The imaging beam enters through the lower window in the picture (direction: y).
Top, right: the big window, through which we send the horizontal MOT beams (direction x); the paths for the 45° MOT beams and the position of the chip (not yet into the chamber) are marked in purple.
Bottom, right: the imaging window. The chip mounting is visible: the three copper bars for the Z and H structures on the upper part and the ceramic mounting (below which the chip is glued) at the center.

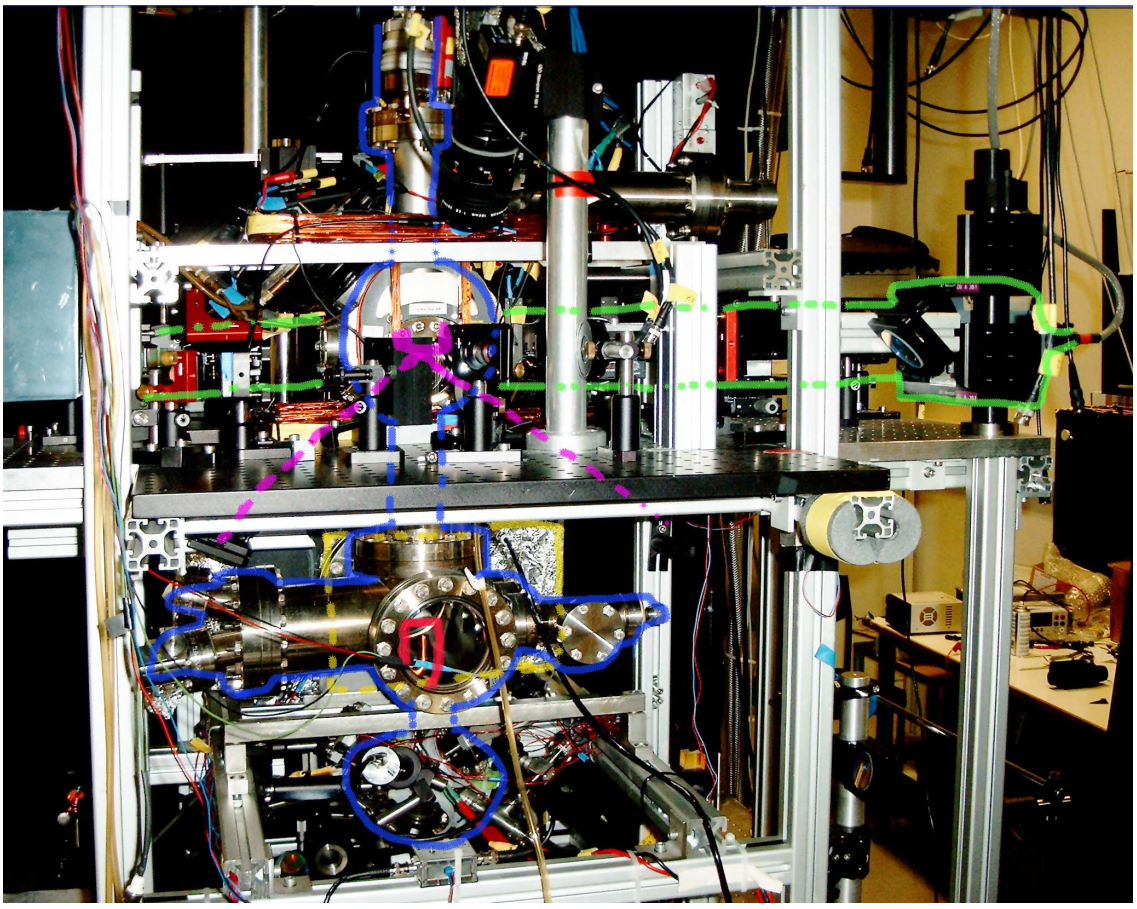

Figure 5.3: The whole vacuum chamber. The steel chamber is highlighted with a blue line; the direction along which we perform imaging and the CCD camera (right, hidden behind a mirror) are outlined in green, in red the nozzle between the two MOTs; in yellow the 260 l/s pump and in purple the chip (not visible) with the two 45° beams.

Chapter 6

Fields

6.1 Magnetic fields

The realization of a MOT needs magnetic field gradients of a few Gauss per mm (see eqn. 2.4) The consequences for the experimental setup are shortly outlined in the following section.

The required field gradients are created with a Copper $\boldsymbol{U}$ structure in the mounting underneath the chip surface (see section 6.4). For an estimate of its field magnitude, let us consider the one of a thin infinite wire, B, carrying the current I at a distance r from it: $B = \frac{\mu_0 I}{2\pi r}$. If we position the MOT center at $r = 3.5\,\mathrm{mm}$ (approximate separation MOT-trapping wire) for a radial gradient of $\frac{dB}{dr} = 2\,\mathrm{G/mm}$ we need $I \simeq 12\,\mathrm{A}$, corresponding to a value $B = 7\,\mathrm{G}$. To have the center of the MOT at such r, we need then to create there a minimum in $|\boldsymbol{B}|$: we generate a constant external field of the same magnitude and opposite direction, with a coil. In the center of a coil of radius $R = 150\,\mathrm{mm}$, with 50 windings, that field is obtained with a current $I = 3.3\,\mathrm{A}$. A copper coil, realized with a wire of cross section $1\,\mathrm{mm}^2$ has thus to dissipate a total of $P = 9\,\mathrm{W}$. For the magnetic trap, where we need higher gradients, we have already $P = 330\,\mathrm{W}$ for $I = 20\,\mathrm{A}$.

Although these estimates are quite rough, they show what power has to be dissipated on the coils. As a consequence the coils heat up and change their resistance. Given only the temperature coefficient for the copper resistivity, we estimate a relative resistance change in the coils of $\rho = 0.39\,\%/^{\circ}\mathrm{K}$.

6.2 Current stabilization feedback

A stable experiment requires reproducible control parameters.

In order to guarantee the lowest electrical noise possible, the power supplies we use[1] are operated in controlled voltage mode (CV). This means that the output, for constant control signal, is a constant voltage. This electrical potential difference causes currents to flow in coils and wires, that in turn generate the magnetic fields necessary for the atom traps.

The whole design is thus sensitive to changes in coils and wires resistance value. As an example, the maximum current we apply on the trapping Z is $I = 60\,\mathrm{A}$, and the Z cross section at its center is only $0.9\,\mathrm{mm}^2$ (for a schema see fig. 6.14 or app. E). During operation its resistivity (and maybe to a great extent that of the contacts for the connections) can change of a few percent. Similar problems are encountered in the coils, as seen above, and particularly in the B_y bias coil, which sustains a maximum of $I = 20\,\mathrm{A}$. As a result when the experiment is first switched on this load change (caused by ohmic heating) has the effect of decreasing the currents, and in turn the magnetic fields. We observe a drift in the trap parameters (mainly trap bottom), with a time constant of around $\tau = 30'$. Such a drift, although to a less extent, can be observed every time important

[1] Company: Agilent, models: 6634A 6641A 6642A 6651A

parameters are changed, as for example the overall experiment duration. This has an impact on the time lost every time the setup has to be adjusted or changed. Where possible water cooling helps improving the situation. However it is not possible to cool efficiently the structures inside the vacuum chamber, for which we observe current drifts of up to 300 mA (on currents of 60 A).

We developed a feedback circuit to stabilize currents and overcome such limitations, as described in the following section.

6.2.1 Feedback concepts

The power supplies used accept a voltage as input control signal V_a, and provide a voltage V_L and a current I_L at their output. For the feedback circuit a a current sensor measures I_L and converts it to a voltage V_2. An amplification loop compares the control signal V_1 with V_2. This in turn produces the voltage (V_a) to control the Agilent power supply, with the aim of minimizing the error signal $\Delta V = V_2 - V_1$.

DC

The feedback loop is outlined in figure 6.1.

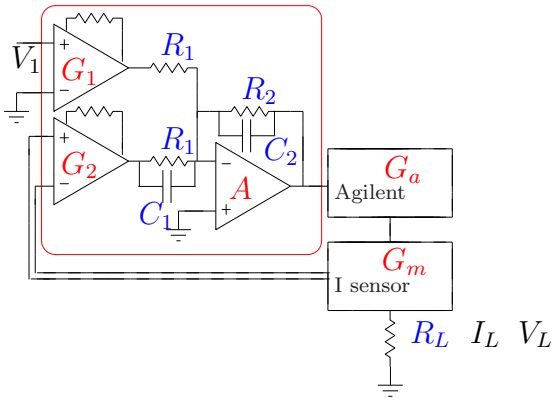

Figure 6.1: Feedback for our current driver; active controls in the loop are outlined in red, passive are marked with blue letters.

The power supply generates the current I_L, that flows across the load resistance R_L. A sensor G_m monitors the current, and sends its output to the input of the feedback loop (V_2 at the input of the amplifier marked G_2). V_1 has to control I_L. In fig. 6.1 the active elements and the sensor are indicated by their gain (red text); passive elements are in blue. The input differential amplifiers G_1 and G_2 make the circuit a bit more complex, but have been introduced in order to decouple the ground in V_1 with that at the Agilent output, and to multiply V_1 and V_2 for convenient factors. The current transducer amplification G_m is given in V/A; all other amplifications are in V/V.

The loop is analyzed between the inputs of G_2 and the output of the sensor G_m; only this path will be studied for performance and stability.

For the loop to work correctly, its gain G_L has to be negative and much greater than one [94]. For demonstration we can choose a typical value of:

$$G_L \simeq 4000 \tag{6.1}$$

Then a drift $\Delta I = 400\,\text{mA}$, on a nominal current of 60 A, is reduced by the feedback to only $\delta I_{feedback} \simeq \Delta I / G_L = 0.1\,\text{A}$. At DC the loopgain is given by:

$$G_L = G_2 G_r \cdot G_a \frac{G_m}{R_L} = G_2 G_r \cdot c \qquad \text{with} \qquad G_r \equiv \frac{R_2}{R_1} \quad , \quad c \equiv G_a \frac{G_m}{R_L} \tag{6.2}$$

In our case R_L is realized by a wire or by a coil ($R_{wire} = 30m\,\Omega$ $R_{coil} = 1\,\Omega$), with the Agilent 6551A and the current transducer LA 100[2] already built in our homebuilt current switches[3] $G_m = 0.01\text{V/A}$, $G_a = -1.6$. The condition 6.1 on G_L is satisfied when $G_2 G_r|_{wire} \simeq 7500$ and $G_2 G_r|_{coil} \simeq 250000$. The current I_L (at DC) is easily calculated:

$$\begin{cases} I_L = \frac{V_L}{R_L} = (V_1 \cdot G_1 - V_m \cdot G_2) \cdot \frac{G_r \cdot G_a}{R_L} \\ V_m = \frac{V_L}{R_L} G_m \end{cases} \Rightarrow I_L = V_1 \cdot \frac{G_1}{G_2 \cdot G_m} \cdot \frac{1}{1 + \frac{R_L}{G_m \cdot G_2 \cdot G_r \cdot G_a}} \tag{6.3}$$

Where V_L is the voltage at the output of Agilent power supply, V_m the voltage at the output of the monitor. For $G_L \gg 1$

$$\begin{cases} I_L \simeq V_1 \cdot \frac{G_1}{G_2 \cdot G_m} = V_1 \cdot \frac{G_1}{G_2 \cdot 0.01} \\ \frac{dI_L}{dR_L} / I_L \simeq -\frac{1}{G_m G_2 G_r G_a} \end{cases} \tag{6.4}$$

- G_1 is defined by the requirement that we would like to use the full output span of Adwin control voltages ($-10\,\text{V}$ to $+10\,\text{V}$; see chapter 9 for more details) to define our current, and that we have to avoid clipping at the output of G_1.
- G_2 is fixed when we consider that the $10\,\text{V}$ on Adwin have to correspond to the max desired current on the wire/coils.
- $|G_r|$ can be chosen to respect the condition $G_L \simeq 4000$.

In order to have maximum currents around $I_{L\,coil} = 20\,\text{A}$ and $I_{L\,wire} = 60\,\text{A}$ we calculate then $G_1 = 1.2$, $G_{2\,coil} = 60$ and $G_{2\,wire} = 20$. Together with eqn. 6.1 and 6.2 this gives: $G_{r\,coil} = 4200$ and $G_{r\,wire} = 380$. We can already see that the gain requested in the case of the coil is quite big for a single opamp, and we have to use an extra stage (more on this in the section on AC behaviour), obtaining a circuit as in fig. 6.2.

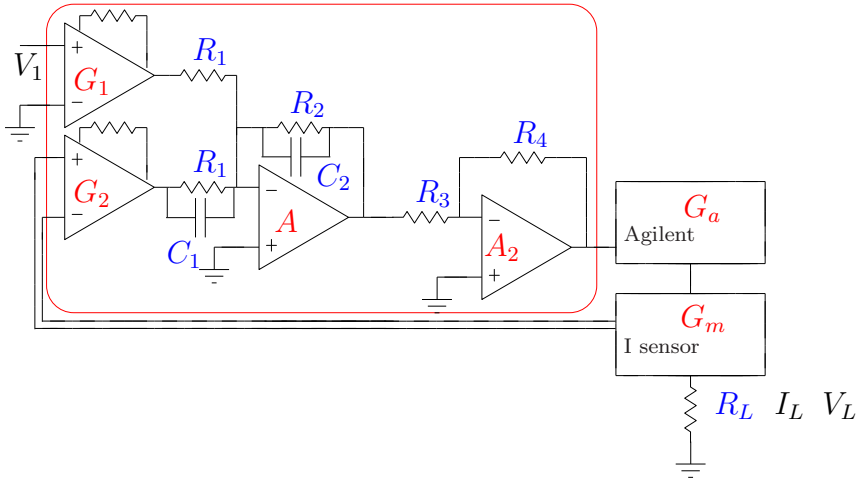

Figure 6.2: Coil feedback: an extra amplification stage A_2 has been introduced.

Another source of drifts in the currents is the inevitable drift in the offset of amplifiers/sensors. Every amplifier has some offset, specified as two independent sources (voltage and current) at its inputs, that can exhibit a temperature drift. It is important to consider the effect they have on

[2] Company: LEM, model: LA 100-P; conversion-ratio 1:2000, Bandwidth 200kHz
[3] Developed in house and based on IGBT solid state switches; model A366x_DS

I_L, and choose suitable opamps, like the TL071[4]. As a reference this opamp has an input offset voltage of $V_o = 3\,\mathrm{mV}$ with drift $V_{drift} = 18\,\mu\mathrm{V}/^\circ\mathrm{C}$ and current offset of $I_O \leq 10\,\mathrm{nA}$.

Now that we have an idea of how the feedback circuit will look like, let us analyze its stability and speed.

AC

Characterization. For the complete characterization of our feedback loop we need to know the frequency response of instruments, opamps, sensors.

From measures on our Agilent power supply we observe a dominating pole at a frequency dependent on the load, typically $50 \leq \nu_{cut} \leq 500\,\mathrm{Hz}$ (fig.6.3).

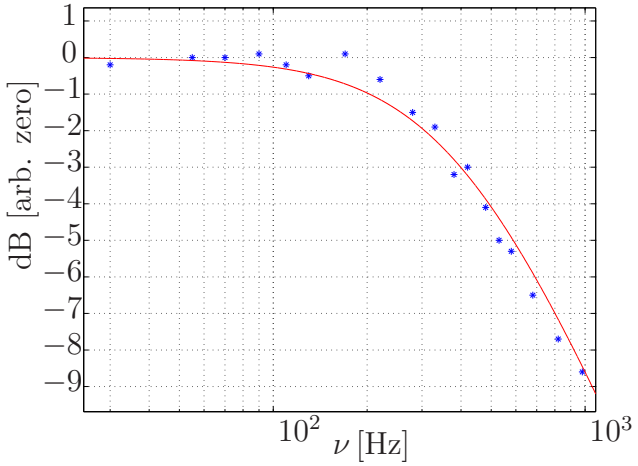

Figure 6.3: AC response of Agilent for frequencies $\nu < 1\,\mathrm{kHz}$; $\nu_{cut} = 400\,\mathrm{Hz}$; *blue dots*: measurements - *red line*: fit with a single pole response function

The fastest possible settling time can be obtained if we introduce in the AC response of the feedback a zero at ν_{cut}, by the RC couple $R_1 - C_1$ in fig. 6.1. To allow some flexibility (i.e.: Power supply change) C_1 can be varied plugging/unplugging capacitors, without interfering with the DC loopgain.

Then we have the current sensor. However its cutoff frequency lies at a much higher value (around 200 kHz), and we would not consider it any longer.

At last, we need the characteristics of the amplifiers used in the feedback circuit. Those for some commonly used amplifiers are summarized in table 6.1. The INA114[5] is used because of its differential inputs, the others[6] [7] are quite general ones, with slightly different characteristics.

Model	Max Gain	ν_0[Hz]$\equiv GBW$
INA114	1k	1M
μA741	200k	1M
TL071	200k	3M
OP07	500k	0.6M

Table 6.1: Opamp data

[4]Company: Texas Instrument; model: TL071, JFET-input operational amplifier
[5]Company: Burr-Brown; model INA114, Precision Instrumentation Amplifier
[6]Company: Philips Semiconductors; model $\mu A741$, general purpose operational amplifier
[7]Company: ANALOG DEVICES; model OP07, Ultraprecision Operational Amplifier

Stability. As we said a feedback loop needs to have an open-loop gain high in modulus, and negative in sign; this has to be true at DC, but needs to be considered further in the frequency domain.

An important effect is the introduction of a phase delay of $\pi/2$ for every pole in the Bode diagram of the building blocks of the feedback circuit. In order to know the dominating cutoff frequency $\nu_{1.pole}$ we have to consider their connection: for resistive loads $\nu_{1.pole} = GBW/|G_{fb}|$, where G_{fb} is the gain of the amplifier at DC once mounted in a feedback loop. For example if we do not consider the capacitors the amplifier A in fig.6.1 has $G_{fb} = G_r = -R_2/R_1$ (as fig. 6.4). With complex impedances we can also introduce extra poles/zeros; in first approximation the second pole (which sits above ν_0) does not move.

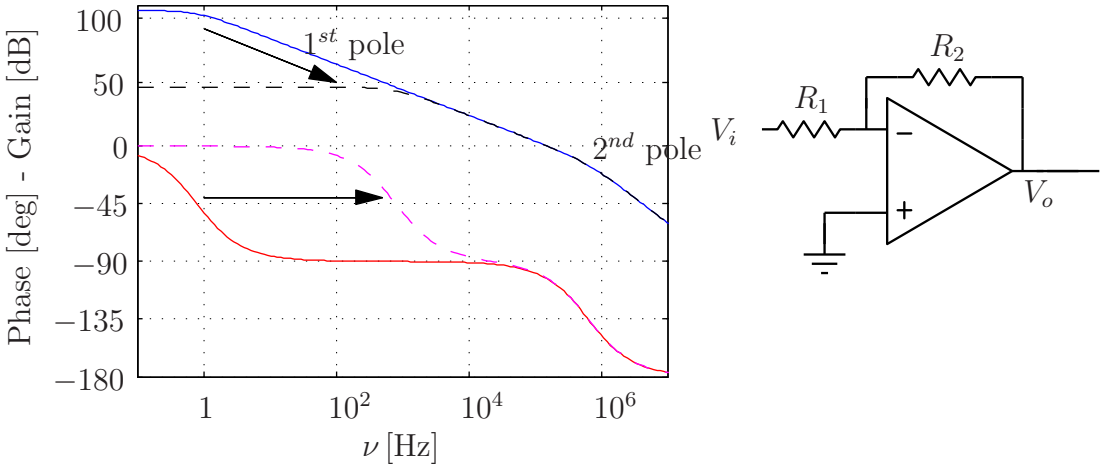

Figure 6.4: $\mu A741$ Bode plot simulation for the circuit at the right: decreasing the gain $|G_r| = \frac{R_2}{R_1}$ moves first pole to higher frequencies. Dashed lines: lower gain. Upper curves: gain, lower curves: phase.

Above $\nu = \nu_{2.pole}$ the phase delay introduced is π, so the signal is inverted and the feedback becomes positive; a small noise can be amplified, leading to oscillations in the system. There are two empirical conditions that these systems need to satisfy in order to be stable:

- *Gain margin*: when the phase delay is π the gain must be $|G| < 2$
- *Phase margin*: when $|G| = 1$ the phase delay must be lower than $\frac{3}{4}\pi$ rad. ($\frac{1}{4}\pi$ phase margin).

In the previous subsection 6.2.1 and eqn. 6.1 we fixed the loopgain G_L. The stability conditions are satisfied by the introduction of a dominating pole at a sufficiently low frequency and a zero in correspondence of the first pole (that of the Agilent, see fig.6.3) so that as the unit gain frequency also the speed of the feedback will be maximized.

Noise

Noise considerations strongly influence the choice of the correct circuit components. We see that the main noise contribution comes from the current monitor; in order to avoid other sources the low noise instrumentational amplifier INA114 is to be used as input stage. The amplifiers following in the feedback chain are less important in this respect. In fact their noise contribution, if considered for comparison at the input of the loop (*equivalent input noise*), has to be divided by the gain of the preceding stages.

Operating conditions

The Agilent 6551A accepts a control voltage between -5 and 0 V: output voltages of the feedback have to be limited to this range. This consideration is important when the current is interrupted by a switch, and the control signal reaches full swing.

In the environment there will be also a lot of RF power, with sweeps across a range of frequencies; if we have a resonance at only one of these frequencies the feedback will be unreliable. Moreover instrumentation amplifiers tend to convert RF common mode signals at their inputs (picked up by cables) to a DC at the output: this problem has to be addressed too.

6.2.2 Realization: Simple wire load

AC

Resuming what we said in 6.2.1 , and considering a μA741 as second stage amplifier, with a fixed gain of 400, we have what shown in table 6.2

Stage	DC gain [V/V]	1^{st}pole [Hz]	2^{nd}pole[Hz]
Input amplifier	20	1M/20=500k	2M
Opamp A	400	1M/400=2500	2M
Agilent	$1.6/R_L$=480	400	$\gtrsim 10k$
Monitor	0.01	200k	Not important

Table 6.2: Summary of the main values characterizing the feedback circuitry.

With $G_L = 4000$ and a first pole around 400 Hz, we would have a unitary gain at $\nu_0 = 1.6\,\mathrm{MHz}$. Before that frequency there are at least two other poles. We shape thus the feedback transfer function, with a zero in opamp A at $\nu_{zero} = 400\,\mathrm{Hz}$ (to cancel the power supply pole) and a dominating pole at $\nu_{1.pole} < 400\,\mathrm{Hz}$. This is done, respectively, with the capacitor C_2 and C_1 (fig.6.1). In fig. 6.5 we can see the effect on the transfer function of A if we increase $C1$ (moving from the continuous line to the dashed magenta) or $C2$ (moving from the continuous curve to the dashed blue one).

DC

As can be seen in fig.6.6 left, the feedback is working as expected. Also for test loads much higher than $R_{wire} = 30\,m\Omega$ measurements show that I_L changes $0.91 \pm 0.03\%/\Omega$, or 3.2 mA on $I_L = 60\,\mathrm{A}$ for a 20% change in R_{wire} (see fig. 6.6). The time stability is also satisfactory, as can be seen in fig. 6.6 right, showing what happens after switching on the whole experiment (after some hours being off); part of the drift is here fictitious and due to drifts in the electronics monitoring dI_L/dt. This result has to be compared with the situation without the feedback, where in the first 30 min a drop in the current of about 300 mA was observed.

Transients

Lastly we provide some images on transients. In general the current behaves as expected. The only problem noted was an undershoot in stepwise current changes, only in case of large and negative changes (fig. 6.7 left). This is because the feedback circuitry leaves the linear range. The problem can be avoided by driving the change with a ramp (in this case of duration $t \simeq 500\mu s$). On the right graph the overshoot in the red curve after the switches close is due to a wrong pole-zero cancellation, and it is easily corrected. Limitation of the tension V_a driving the supply is accomplished with a Zener diode ($-4.1 < V_a < 0.8$).

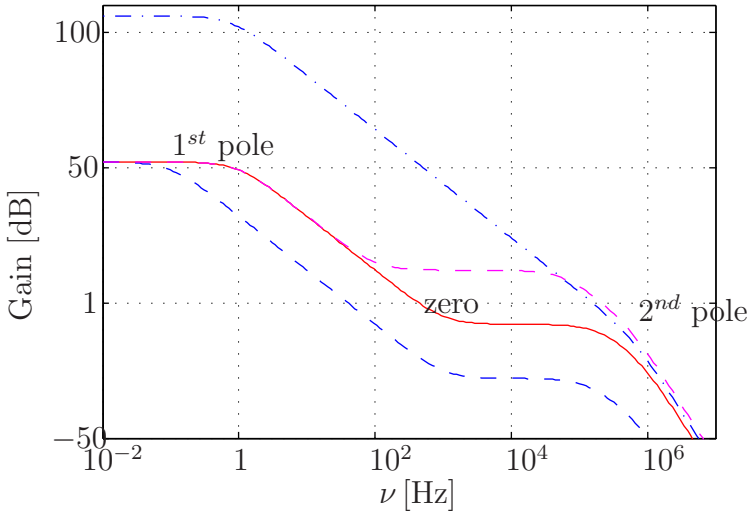

Figure 6.5: Bode diagram for $\mu A741$. Blue dash-dotted curve shows the open loop gain of the amplifier $A_0(\nu)$. Red continuous curve is for a feedback configuration with $\nu_{1.pole} = 1\,\text{Hz}$ and $\nu_{zero} = 1\,\text{kHz}$. Lower blue and upper magenta dashed curves are obtained, respectively, going to $\nu_{1.pole} = 0.1\,\text{Hz}$ and $\nu_{zero} = 100\,\text{Hz}$. The second pole stays constant in frequency.

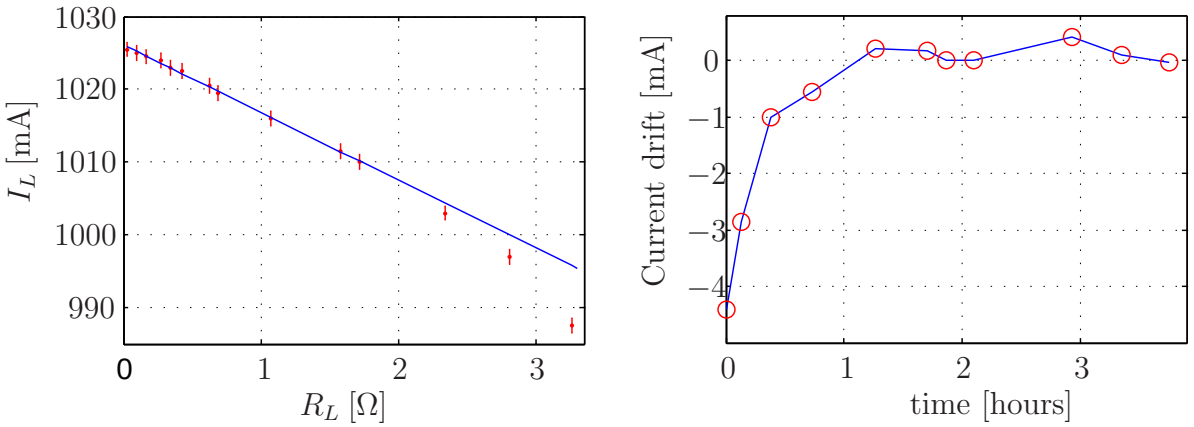

Figure 6.6: Current drift with a resistive load; left: around $I_L = 1025\,\text{mA}$ in dependence of R_L; blue line: fit up to $R_L = 1.7\,\Omega$. Left: time stability at $I_L = 20\,\text{A}$; continuous line as eye guide.

Noise

We measured the noise in the copper $\boldsymbol{Z}$ structure with different sensors and a network analyzer with a sufficiently low noise floor[8]. The SR 770 can go up to a frequency of 100 kHz, much above the actual trap frequencies we realize on the atomchip. In series with the current transducer for the feedback and with the copper $\boldsymbol{Z}$ we added:

- A second standard current transducer (monitor).
- An enhanced current monitor (see fig. 6.9, left) with 7 wire windings instead of 2 (increase of 3.5 in signal).
- A $10\,m\Omega$ resistor.

[8] Company: Stanford Research System; model: SR 770, FFT Network Analyzer

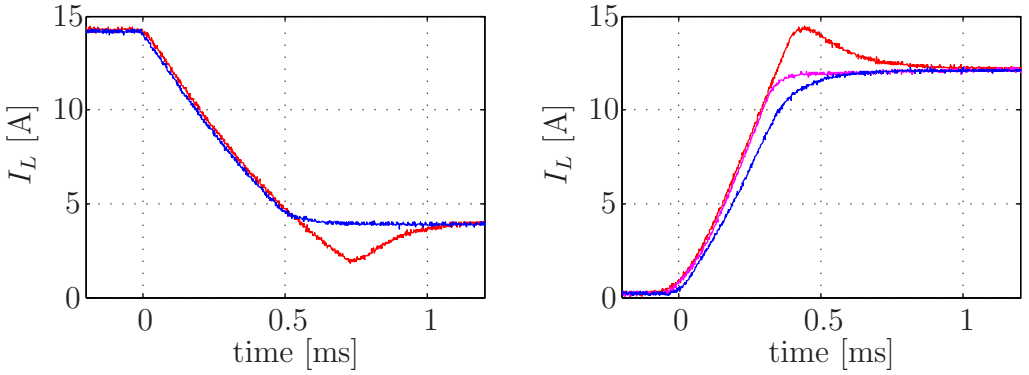

Figure 6.7: Left: undershoot with large negative transients (red curve), avoidable by driving the supply with a ramp. Right: transient after closing the switches, with overshoot due to wrong pole-zero cancellation (red curve) and after correction of the time constants (magenta); the feedback is marginally faster. In blue the transient without feedback.

As seen in previous tests done in house [95], the power supply output noise is essentially a voltage noise, thus increasing the load resistance decreases the overall current noise; we take care that the total load R_L during test matches the conditions we have in the experiment.

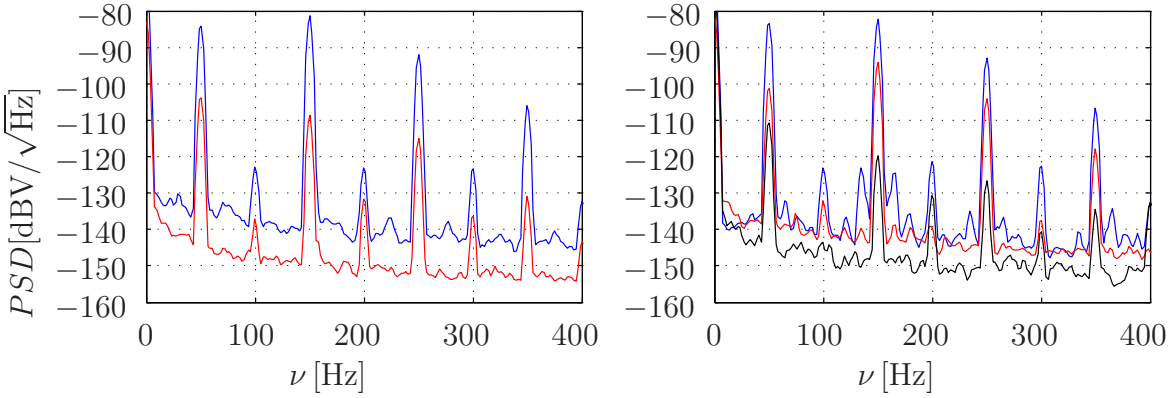

Figure 6.8: Low frequency noise on the copper $\boldsymbol{Z}$ measured with different sensors. *Left*: without feedback. *Right*: with feedback. Curves' color corresponds to: *blue*, bare monitor; *red*, enhanced current monitor; *black*, new feedback with sensor IT-600[9]. The bare current monitor noise levels are too high to measure a change in the peaks. The Enhanced monitor shows the feedback is noisier. Only using the new sensor[9] in the feedback loop we notice a decrease in the peaks. 10 mV correspond to 1 A

In fig. 6.8 we can observe the effect of the feedback on the noise. The measurements with the 10 mV/A monitor (blue curves) do not change with the feedback, because their noise level is higher than the noise floor which we want to measure. The measures with the 10 $m\Omega$ resistor show the same result; both sensors are thus insufficient. The enhanced monitor has a better response (red curve), and indicates that the feedback introduces some noise and needs to be improved. To lower its value below what we have without feedback we need to increase the signal to noise ratio in the sensor of a factor 3.5 (about 10 dB); we can not use a 35 $m\Omega$ resistance (too high load to reach 60 A) or a monitor with 7 wire windings ($I_{total} = 7 \cdot 60$ A is above the sensor limit of 150 A). As solution we choose a better sensor: the IT 600-S[9] (see fig. 6.9, center) proved to be the working solution.

[9]Company: LEM, model IT 600-S, high accuracy current transducer.

The black curve shows the noise floor achieved with the new sensor in the feedback. Because of the transfer function of the feedback circuit, above 3 kHz no noise reduction can be seen.

Figure 6.9: Current sensors; *left*: LA 100-P 'enhanced' solution, with 7 windings (double wiring); *center*: IT 600-S with three windings; *right*: transducers supply (developed in house)

RF

The copper structures connected to the power supply are used also to generate the fields necessary for RF evaporation. We found some resonances in the feedback circuit around $\nu_{RF} = 5\,\text{MHz}$ and 17 MHz, leading to DC shifts and higher noise levels.

The problem resides in a weakness of the instrumentation amplifiers: a RF frequency in common mode is amplified or rectified, giving a DC component. We can improve the performance by grounding one of the inputs of each INA114. In order to avoid ground loops at low frequencies we do this via a capacitor ($C + Load \simeq 100\,\text{nF}$ between the 'ground' at the inputs and that at the output[10].

6.2.3 Realization: Coils

As said before, coils have a higher impedance than a short wire, and we are forced to use another amplifier stage in the feedback circuitry.

AC

The extra stage introduces other poles. We have thus to be careful in designing a stable feedback, by balancing the gains of A and A_2 in fig. 6.2 to obtain $G_{r\,coil} = 4200$.

Moreover to keep stability with a higher loopgain we have to reduce the frequency of the first pole, defined by the time constant of R_1 and C_1 in fig. 6.2, below the value we used to drive the copper structure.

DC

The behaviour at DC is similar to what was observed with the low impedance load. Current drifts are around 0.5 mA. Experiments with condensate confirm the trap bottom stays constant, with shot-to-shot oscillations in the RF end frequency (for condensation, or complete evaporation) lower than $\Delta\nu_{RF} \simeq 200\,\text{Hz}$.

Transients

As done for the wire we have to limit the control voltage. The current we want to drive corresponds to almost the maximum control voltage at the input of the Agilent. Thus the Zener diode has to be

[10] With such a solution the input is no more fully differential, but this happens at frequencies much higher than those typical of our signal.

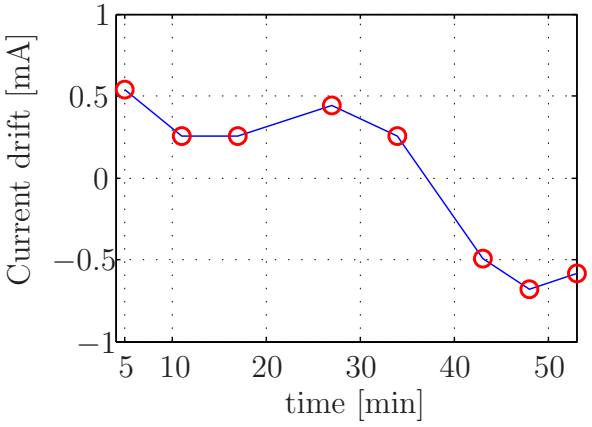

Figure 6.10: Initial drift in coils, depending on time/temperature

an open circuit down to about -5V without compromising the circuit functionality, and then avoid a control voltage below -5V before the power supplies go into protected mode. The diode used in the case of the simple wire ($V_Z = 3.6\,\mathrm{V}$ would severely limit the maximum current achievable.

We ran into a problem with an opamp TL071, because of its output resistance of about $128\,\Omega$ (not documented in all specs), that smooths out the V/I curve of the diode. In this case we used an opamp with low output resistance[11].

The overshoot seen in the case of the wire (fig. 6.7) is not present with the coil, because its slow response gives enough time to the feedback to return to the linear region (fig. 6.11; again, blue: no feedback, red: feedback.).

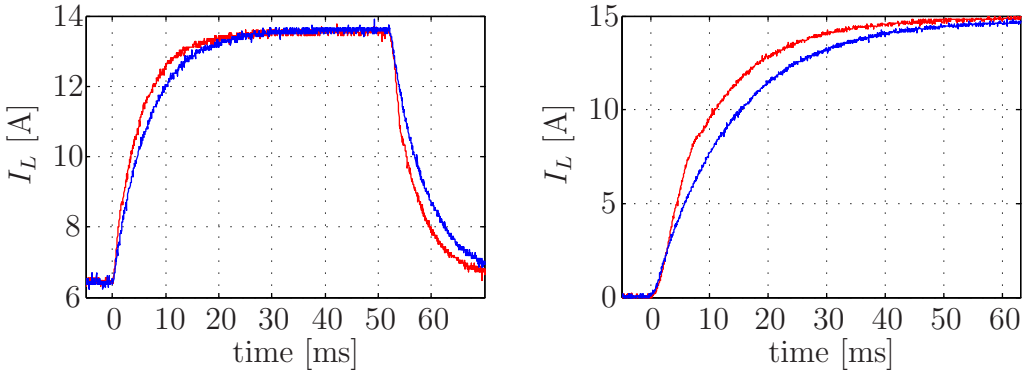

Figure 6.11: Transient in coils; *red*: with feedback, *blue*: no feedback. *Left*: step response, *right*: at the moment when the switch closes the circuit. Also with the coil the feedback is marginally faster.

Noise

From what we have seen in [95] we expect the noise in the coil to be lower than that in the copper structure, thus the original current monitor cannot be used. Again, we employ the LA 100-P current transducer with 7 wire windings instead of 2 and a sensitivity of $35\,\mathrm{mV/A}$. With the feedback the noise at 50 Hz and its higher harmonics is somewhat smaller than before, while we do

[11] Company: Intersil; model: CA3140, 4.5MHz, BiMOS Operational Amplifier with MOSFET Input/Bipolar Out

not observe changes in the background (fig. 6.12). Its level is in any case lower than that in the copper structure.

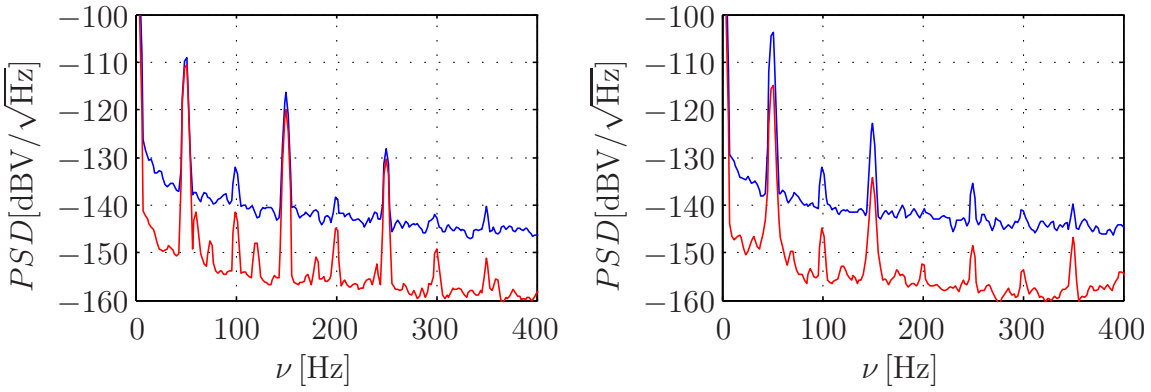

Figure 6.12: Low frequency noise in coils measured with different sensors; *left*: without feedback, *right*: with feedback. Curves' color corresponds to: *blue*: bare monitor (10 mV/A), *red*: enhanced current monitor (35 mV/A, rescaled for comparison with the other curve). The bare current monitor noise levels are too high to measure the decrease in the peaks. The enhanced monitor is able to show the improvement of the feedback solution. All data taken with $I_L = 10$ A. 10 mV correspond to 1 A

Other problems

During operation, passing from low to high currents and back, we noted a hysteresis behaviour. After inspection it was found that it was caused by capacitors C_1 and C_2 (changing amplifiers had no effect). The following steps were taken in order to avoid this problem:

- We used a couple of diodes across C_2, to limit the voltage.
- We changed C_1 and C_2 types, from tantal to ceramic.

Due to the extreme stability achieved in the currents an exhaustive test of the feedback circuit can be performed only by using the BEC in the magnetic trap as an inspection tool. Some measurements on the trap stability are given in chap. 10. The other important problem (noise in fields) is usually not an issue: the lifetime of the condensate in the close proximity of the chip surface (where we actually perform our experiment) is limited by other factors, as thermal currents in the chip conducting structures (causing heating and losses through spin flips).

6.3 Currents on the chip

To realize microscopic atom traps, no ordinary wires can be used, as the precision with what they can be modeled is not enough. The solution is employing standard lithography techniques, using a carefully polished silicium chip as a framework on which gold conducting structures can be deposited or grown; this chip provides the necessary structural stability, and is a valuable (and necessary) heat sink when currents flow. Minimizing the contact heat resistance between conductors and the substrate (for example decreasing the oxide thickness) allows to reach current densities of about 10^{11} A/m^2; moreover voltages as high as 500 V can be applied [96].

However the maximum currents attainable (a few A in structures of a few μm thickness and a few hundreds μm width) are too low for trapping enough atoms in the MOT and in the first phase of the RF cooling. For this reason, the mounting that holds the chip in the vacuum chamber

is provided of massive copper structures, in the close vicinity of the chip, that can continuously sustain currents of up to 60 A.

For more informations on the chip refer to the chapter 7, where we describe it in greater detail.

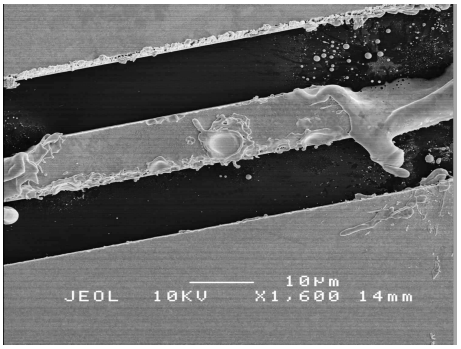

Figure 6.13: An excessive current can lead to the melting of conductors

6.4 Mounting and copper wires

The chip mounting is fixed on a vacuum flange with electrical feedthroughs for the signals to be delivered (trapping currents, voltages, RF signals). The chip holder (white structure in the picts. 6.14) is oriented downwards, so when we remove the magnetic fields the atoms are released in a free fall.

A thick copper column in the center provides mechanical stability and acts as a thermal sink. The $\boldsymbol{H}$ and $\boldsymbol{Z}$ copper structures underneath the chip (in figure 6.14: left and right pictures in red and yellow, center figures as they look once realized) are electrically/thermally fixed to six massive copper rods, and set into a ceramic holder. The materials we use for this are Macor®, and Shapal$^{\text{TM}}$in the second chip. The choice has been done consideringor their UHV (ultra-high vacuum) capability, machinability and high heat conductance that allows good heat flow away of the conducting structures. Everything is realized with the highest precision possible in our mechanical workshop (about 100 μm), to allow the best thermal contact. Once the mounting is ready, the chip is fixed on top of it, with a thermally conductive epoxy glue.

Following the experience acquired while running the experiment and the setup modifications of other experiments in the group [97], we slightly changed the mounting for holding the second chip we realized. In particular the monolithic $\boldsymbol{H}$ + $\boldsymbol{Z}$ copper structure employed has been split in an independent $\boldsymbol{Z}$ block (in red in fig. 6.14), plus a separated $\boldsymbol{H}$ (in yellow in fig. 6.14); its central connection is now broader. While the $\boldsymbol{Z}$ works as before, the new $\boldsymbol{H}$ (or better said the $\boldsymbol{U}$ constituted by the central connection plus two arms) allows to have a magnetic field for the MOT that more closely approaches a quadrupole field. As a consequence we can trap enough atoms already with this structure, avoiding the use of the massive quadrupole coils. This simplifies the experiment and reduces the hardware requirements. As downside the $\boldsymbol{H}$ structure now needs to be driven with 20% more current. However, as we employ the current stabilization feedback, we can use the same supply alternatively with the copper $\boldsymbol{U}$ or with the $\boldsymbol{Z}$ (thanks to a couple of switches) and have in both cases the same voltage/current characteristic. In this way we further reduce the number of power supplies. The other two free connections in the $\boldsymbol{H}$ are used to apply the RF cooling signal. As other modification we moved the bonding pins apart so that the central section of the chip (where the BEC traps are located) has better optical access. They have a zig-zag disposition to increase the distance between them and ease machining. A shallow trench runs over the ceramic edge, to help in the alignment procedure during the gluing of the chip and improve

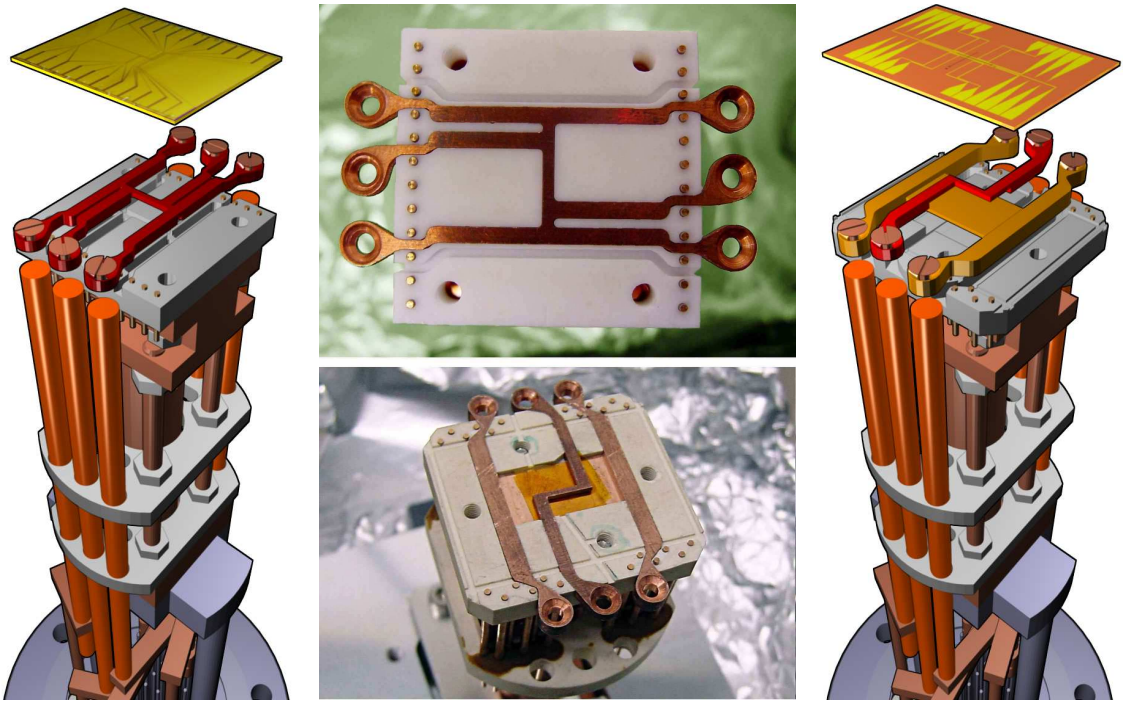

Figure 6.14: The mounting. *Left* and *center-top*: the original copper structure on the mounting. *Right* and *center-bottom*: the improved structure, with independent $\boldsymbol{H}$ and $\boldsymbol{Z}$ (in gold and red) realized for the second chip. Two of the arms of the $\boldsymbol{H}$ plus the central slab constitute the $\boldsymbol{U}$ used for trapping atoms in the MOT; the other two arms are AC-coupled to the RF source for evaporation. Positioning of the chip bonding pins also changed, to leave free optical access to the central part of the chip, where the atomic trap is located. A metal base (partially visible in in the picture at the bottom, center) is used to fix the mounting during bonding, in order to provide stability (see also section 7.3).

position matching with the copper structures. Photographs of the mounted chip show their centers have an offset of only 100 μm; the relative angle between chip and mounting is around 3 mRad, although the alignment was done by bare eye. Measures with atoms also show the minimum of a copper and of a chip trap have a mismatch around 150 μm (see fig. 12.6).

6.5 RF cooling

The copper structures used to realize the U-MOT and the magnetic trap are also employed for the RF evaporative cooling: the RF signal is AC-coupled to the two arms of the $\boldsymbol{H}$ structure not used for the U-MOT. As the power supply used in the copper $\boldsymbol{U}$ is disconnected during magnetic trapping all the current provided by the RF source can be efficiently coupled to the broad copper slab underneath the trap, very close to the atoms. Tests were also done with the radio frequency signal applied directly to a chip wire; evaporation efficiencies were similar. In our experiment we sweep the RF in the range $32 > \nu_{RF} > 0.7$ MHz in 12.4 s, while increasing the transversal confinement $\nu_\perp$ from 110 to 1300 Hz, as indicated in fig. 6.15. At the same time, with the decrease of the cloud size, we move the trap toward the chip. In this way the higher transversal trapping frequency speeds up the rethermalization of atoms during evaporation, and the loading of the BEC or ultracold sample in the various microtraps is facilitated.

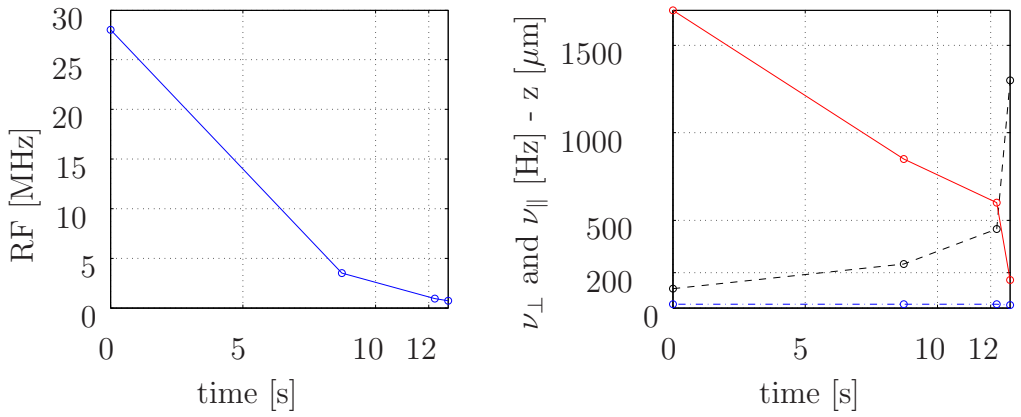

Figure 6.15: Trap parameters used in the experiment during evaporation. *Left*: The radio frequency signal. *Right*: the transversal frequency $\nu_\perp$ (black dashed curve) is constantly increased and $\nu_\parallel$ is always below 20 Hz (blue dash-dotted curve). The atoms-chip distance is reduced to about $z = 160\mu$m (red curve); From here the BEC can be easily transferred to the chip traps.

Chapter 7

The Atomchip

The cooling techniques developed in the last decades and the use of free standing wires to manipulate and to trap atoms [98] has brought to reality a whole new realm of physics, that was previously confined to textbook examples and thought experiments. To fully develop the potential of ultracold atom manipulation, dwelling into the reach of experimental quantum mechanics, structures on the micrometer scale are necessary.

The different processes developed in the microelectronic industry to create circuits of extreme complexity can be reused to reach this goal [93]. Conducting surfaces are easily created on top of standard Si, SiGe or sapphire chips by evaporation alone, or followed by electroplating. The advantages are numerous:

- The precision in the definition of the structures and in positioning the various elements can be of better than $1\,\mu$m
- The chip provides mechanical stabilization and acts as a thermal sink for the conducting structures.
- Different technologies can be built in: permanent magnets, optical fibers and resonators are only a few examples.
- Reproducibility is guaranteed; this characteristic can be important in all the cases a vast production of samples is desired (an example can be the engineering of BEC-based sensors, like accelerometers [99, 100, 9]).

7.1 The first chip

The first chip we employed is made by a 25×30 mm^2 Si substrate on which Si dioxide is made. Upon it a single gold layer of thickness $d = 2.5 \pm 0.1\,\mu$m is evaporated[1] (see fig. 7.1). The gold has a uniform quality, and under the electron microscope it shows to be constituted by nanocrystals of size around $\varnothing = 100\,$nm. Precision in the definition of the edges is around $100 - 200\,$nm .

The main structure on it is a $200\,\mu$m wide 2 mm long $\boldsymbol{Z}$, that we use for trapping atoms with a current of up to 1 A; the current is limited by the number of bondings we could successfully realize and not by the maximum current density tolerable by the chip. Around this $\boldsymbol{Z}$ there are a number of $10\,\mu$m wide wires, that generally run parallel to it, and are interconnected on a few points. On this conductors we etched microscopic structures, as explained in section 11.1.

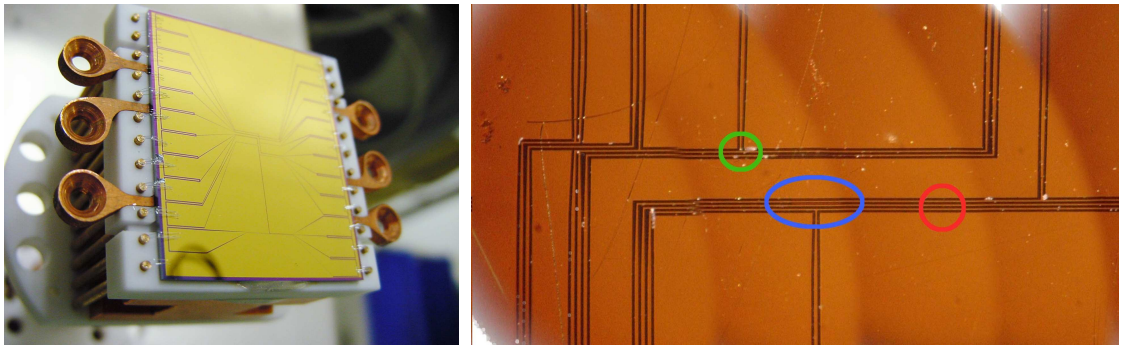

Figure 7.1: The first chip; *right*: the central part, with the wide ***Z*** at the center (width 200 μm, length 2 mm), surrounded by several 5 to 10 μm wide conductors; in color the FIBbed regions (see section 11.1); image produced by superposition of different photos.

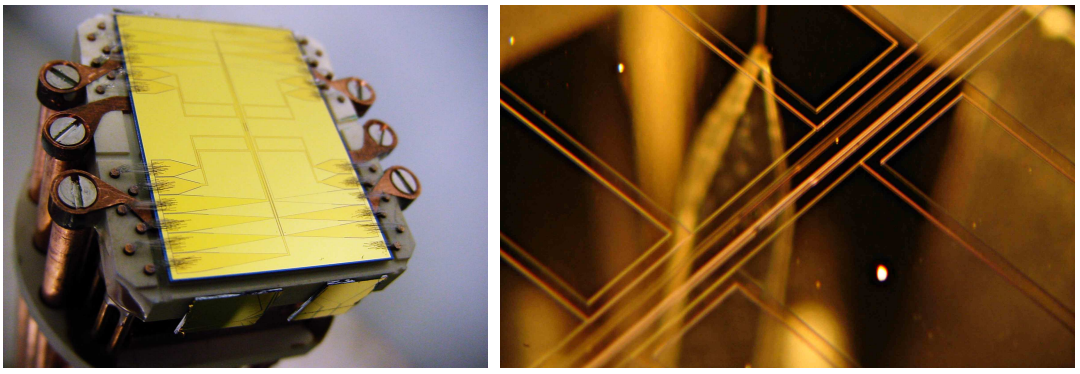

Figure 7.2: The second chip; *right*: photo of the central part of the chip, with the straight wires providing transversal trapping (*side guide*) and the four ***U*** for longitudinal confinement. In the reflection the bonding tip is visible.

7.2 The second chip

The second chip (25×35 mm^2) was designed primarily to provide a testbed for the wires' quality. At the center there are 7 straight gold wires, with widths of 200, 25, and 5 μm, and thicknesses of 250 nm or 2.5 μm. They work as sideguides for the cold atoms. Four structures with a ***U*** shape, toward the center of the chip, provide the required longitudinal confinement.

This design provides a degree of freedom more than the traditional ***Z*** trap: the longitudinal and transversal trapping frequencies can be set independently.

An important process explored in the realization of this chip is the deposition. As gold grows on the silicon dioxide and on the already deposited gold, it forms monocrystalline grains of diameter in the range $10 - 300$ nm. The fine tuning of various physical parameters during gold evaporation has allowed us to have gold sheets with different grain sizes[2]; the data on the wires we have deposited is summarized on the table below fig. 7.3. A deeper analysis on the effects of the gold grains' size on the quality of the trapping magnetic field can be found on [101].

We also packed the pins closer, to have the central chip area open to optical access.

The typical trapping wire in an atomchip is a thin slab of conductor, with a width of $5-200$ μm, running on the surface and connected to the outside world with bondings (see chap. 7). In the

[1]Developed by S. Groth on 20.05.2002, chip number *BXVIII*
[2]Chips realized by the group of R. Folman, BGU facility, 08.2005

Wire	1	2	3	4	5	6	7	U	M
Width [μm]	200	25	5	200	5	25	200	200	-
Height [μm]	.25	.25	.25	2.5	2.5	2.5	2.5	2.5	.25
Grain size [nm]	250	250	250	40	40	40	40	40	40

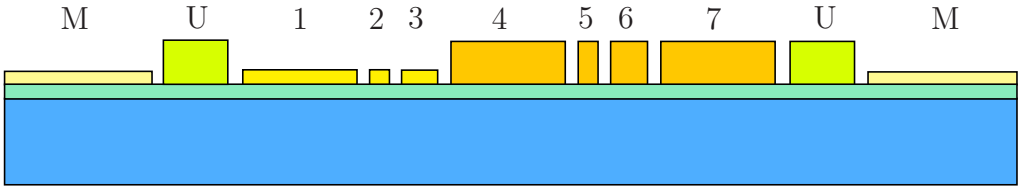

Figure 7.3: Dimensions of the chip structures: 1 to 7 are the straight wires, U for the ***U*** structures, M for the mirror surface

following we will often call such current-carrying structures *wires*.

7.3 Bonding

The current flowing in the chip wires can be (in the case of the main trapping wire) as high as a few Amperes. To sustain it there need to be a low ohmic contact between the chip and the pins along its border. These are in turn connected to the chamber's flange electrical feedthroughs and in this way accessible to the experimenter. The chip is bonded manually, with $\varnothing = 25\,\mu$m aluminium wire (see fig. 7.4, center). The contacts are realized thanks to ultrasonic vibrations, that heat and melt or cut the wire. If the number of bondings per pin is too low, or if the contacts' quality is bad, the current flowing through heats them up, and can in extreme cases lead to the destruction of the electrical contact.

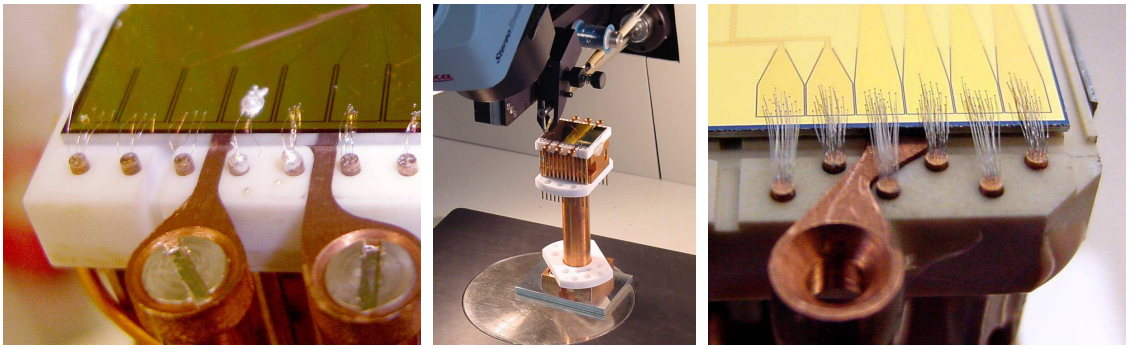

Figure 7.4: *Left* bondings on the first chip, with conductive epoxy glue to fix some contacts. *Center* the bonding machine; the absence of a proper stabilizing base as well as microscopic vibrations of the pins (not glued as in the second chip) compromised the quality of the bondings. *Right* detail on the pins of the second chip; proper stabilization of mounting and gluing of the pins was a decisive step in realizing easily high quality connections.

To have good bondings it is important to choose the correct energy and time duration of the ultrasounds, with different settings for the cases of bonding on the chip (gold) or on the pins (copper-beryllium)and the pins' cap have to be polished (or in case gold coated). But most of all the chip needs to be properly stabilized, and should not vibrate with the ultrasounds. Vibrations are sometimes spotted by eye (i.e. if the pin is moving), but often go undetected, because of their

high frequency and low amplitude of oscillation. In the picture 7.4, left, the bondings realized on the first chip are visible; their number (per pin) is always below 5 and the quality of the contacts is not good. After baking the chip in the test chamber some connections broke, and we repaired them with conductive epoxy glue. During operation many other connections failed. The second chip (fig. 7.4, right) was fixed to a heavy metallic block prior to bonding, to avoid movements and vibrations. All the pins have been fixed to the ceramic mounting with UHV epoxy glue. A minimum of 18 bonds could be realized on each pin ($\varnothing = 0.9\,\mathrm{mm}$).

7.4 Technological limits

There are various ways of growing a metallic structure on a surface. For atom chips we often need gold conducting sheets with a thickness of a few μm. Usually a thin ($\sim 20\,\mathrm{nm}$) Titan adhesion layer is deposited on top of a $100 - 200\,\mathrm{nm}$ thick silicon dioxide; two different methods are then followed to grow conducting sheets.

A first one is evaporating a thin metallic layer, and then electroplate a thicker one on top of it; this procedure has been used by several groups, and generates structures with an edge roughness of about $1\,\mu$m, as can be seen in fig. 7.5, left[3]. This is the fastest method, but it has the highest surface roughness. A second, thin gold layer is often required if good reflecting surfaces (at optical wavelengths) are needed (as in the case of the mirror MOT[92, 93]).

Another solution is evaporating the whole gold sheet; the quality of the deposited structure is much higher, with granularity on the order of 100 nm, as visible in fig. 7.5, left[4] (the scale inside the red circle is 100 nm). Some defects can be present (as the hole in the picture) but are minimized by proper clean room operation; chips can be however inspected and defective samples bumped. For more information on the whole process, please refer to [103].

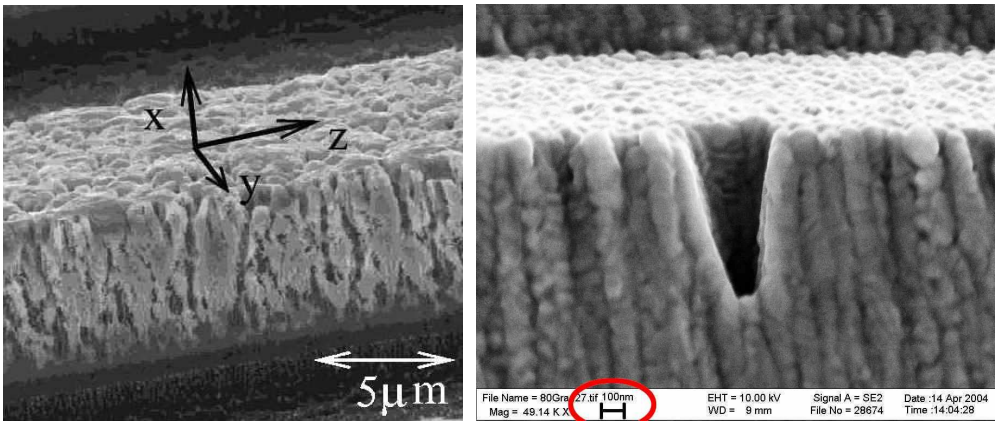

Figure 7.5: The corrugation. *Left*, an electroplated structure. *Right*, one of our atomchips, with deposition by evaporation, in correspondence of a defect; columnar structures are visible. Red sign marks the length scale of 100 nm.

7.4.1 Disorder potential

The poor definition of the wire edges, as well as defects or inhomogeneities in its bulk cause the current to deviate from its straight, uniform flow, giving rise to a current component perpendicular to it; this in turn modulates the trap bottom. As result the potential, along the longitudinal trap direction, will present a noisy component.

[3] photo from the group of A.Aspect [102]
[4] photo courtesy of Söenke Groth

Such spatial fluctuations have been first observed in copper wires [104] and then also on electroplated chips[105, 106, 102]. As the BEC approaches the surface the disorder potential at the trap position increases, first modulating the BEC density (at a distance of around $z = 100\,\mu$m), then fragmentating the condensate in distinct blobs. Because of this effect it is often referred to as *fragmentating potential*. The higher quality of our atom chips allows to have a smooth BEC down to $z = 30\,\mu$m, with fragmentation appearing below $z = 10\,\mu$m.

If the disorder potential in electroplated chips is mainly due to irregularities in its edges definition, there are still open questions in the case of our evaporated wires. There are however indications that it originates from inhomogeneity of the material bulk [13]. The possibilities to further investigate this point are essentially two. The first one, explored in this thesis (chapter 11), is *cleaning* the edges in a portion of a wire, and comparing the fragmentating potential in the polished and in the bare wire section. The second one, also investigated in our group, is realizing different wires, by tuning the parameters influencing the gold deposition process, and finally the bulk wire quality. The second chip was realized with this purpose in mind and its analisys is the subject of a second PhD thesis [101].

7.4.2 BEC lifetime

Another important limitation in the manipulation of BECs with chips is due to the loss of atoms by thermal induced spin-flip.

The electrons in the chip conductors have random thermal motions, that give rise to time varying currents. These currents in turn generate oscillating magnetic fields, that cause spin flips of the trapped atoms and losses [107, 108, 109, 110, 111, 112, 113]. The effect is dependent on surface distance, more pronounced for small z; below a few μm a BEC lifetime of a few tens of ms can effectively limit the experiments possible.

Cooling down the chip surface does not have the effect desired; if the free electrons' thermal energy is reduced proportionally to T, the resistivity of the gold conductors is reduced as well (in general not proportionally with T), and the net effect is an *increase* in the thermal currents and thus in the magnetic noise; different behaviour is expected in other materials [114].

The thermal currents are instead absent in insulators; we see that we can optimize the BEC lifetime by minimizing the amount of conductors close to the condensate and using wires as thin as possible (compatibly with the required trap parameters) [112]. Such considerations are necessary when we want to perform experiments with strongly confining traps (close to the surface), and have to be taken into account to verify the feasibility of experiments as those proposed in 11.2.5.

Chapter 8

The laser system

8.1 Cooling and imaging lasers

The configuration of the lasers in the experiment is described in detail in [101]; we give here only a short presentation of the setup we are using.

The lasers are kept in a wooden box, isolating them from light and temperature variations in the lab environment, and from air flows. The majority of them are diode lasers mounted in an external cavity Littman configuration, where a piezoelectric actuator modulates the laser wavelength by moving a diffraction grating; typically laser frequencies can be scanned of some GHz without the occurrence of mode-jumps; linewidths usually are below 1 MHz [115].

There are three main blocks in the laser box:

- A couple of diode lasers (*probe beam*), mounted as master and slave, locked to the transition between the $5s_{1/2}, F = 1$ and the $5p_{e/2}, F'$, and exactly to the crossover between $F' = 2$ and $F' = 3$ (fig.8.1 at the left); a double pass Rb vapour cell provides the spectroscopy signals, that are detected in a normal photodiode (returning the Doppler valley and the hyperfine signals) plus an avalanche one (for the error signal), visible in the top, left of the picture. The outputs of the lasers are used for the optical pumping of the atoms (see section 2.3) and for the imaging light, respectively (1) and (2).

- Another master/slave unit (fig.8.1, center) provides at (3) the sufficient light intensity for the repumper light for the two MOTs. A single plus a double pass spectroscopy configuration returns, thanks to simple photodiodes, the electronic signals for the control of the wavelength.

- The last unit is a tapered amplifier[1], giving about 300 mW of power to be split between the lower and the upper MOT, in (4) and (5). A spectroscopy Rb cell is used to recognize the optical transitions, while the lasers are locked by analyzing the beating with the probe beam, with an avalanche photodiode.

Outside the laser box each beam goes through an AOM, that sets the correct frequency and is used to shut down the intensity when necessary; various shutters help to extinguish completely any remaining light (see fig. 8.2).

Part of the light from the cooler for the lower MOT is sent to a fiber (for profile shaping) in (8) to be used as push beam; this will extract the atoms from the lower MOT, sending them upwards to the upper chamber.

The remaining intensity is mixed in a polarizing beam splitter (or PBS) with the 50% of the repumper light (coming from a non-polarizing beam splitter) and sent to a telescope, in (9). It is then split in the three MOT beams and each of them is retroreflected with a $\lambda/4 - mirror$ unit.

[1] Company: Toptica, model n. 110

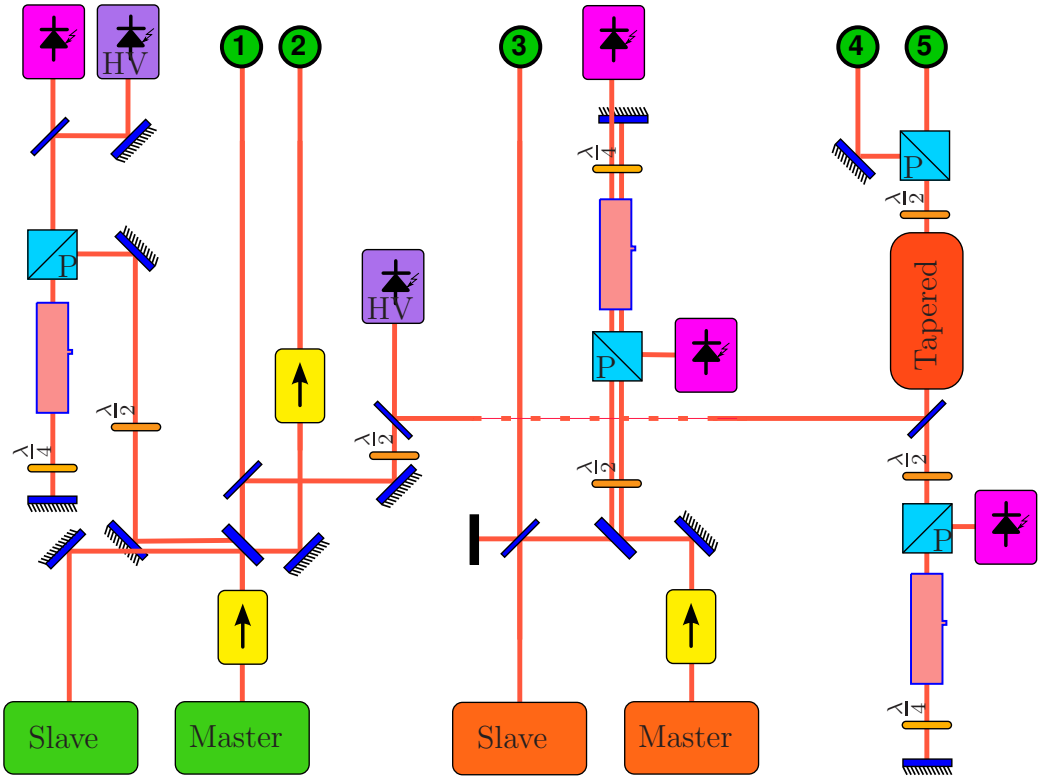

Figure 8.1: The lasers in the experiment. *Left*: the master-slave diode lasers for the optical pumping (1) and imaging (2) light. *Center*: the master-slave configuration providing the repumper light. *Right*: the tapered-amplifier laser box[1] for the two MOTs cooling light.
The yellow boxes are optical isolators; mirrors and glass plates are in dark blue; the polarizing (P) beam splitters are shown in pale blue, in orange the $\lambda/2$ and $\lambda/4$ plates and in rosa the Rb cells for the spectroscopy. Finally we have in purple and violet respectively photodiodes and avalanche (HV) photodiodes.

The other 50% of the repumper light of ③ is mixed with the cooler for the upper MOT; the beam is then expanded, in ⑩, before being split in three. As this is a *mirror MOT* one beam will run parallel to the chip, and the other two will be reflected at 45° on its gold covered surface and counterpropagating.

We have then a beam for the optical pumping (output in ⑦) and the light for the imaging; this last one is the only beam with double-pass AOM. It is coupled into a single-mode fiber, ⑥, to provide a clean profile and stable positioning; in order to avoid unnecessary light scattering and minimize the noise in the pictures the beam diameter is of the same order of magnitude of the length of the condensed atoms in the trap, $\varnothing \simeq 1\,\text{mm}$. It is expanded with a removable lens when we want to inspect the loading efficiency of the MOT (bigger in size).

8.2 The Ti:Sa laser

Aside from the cooling and imaging lasers we have another system, that provides far detuned light for optical potentials.

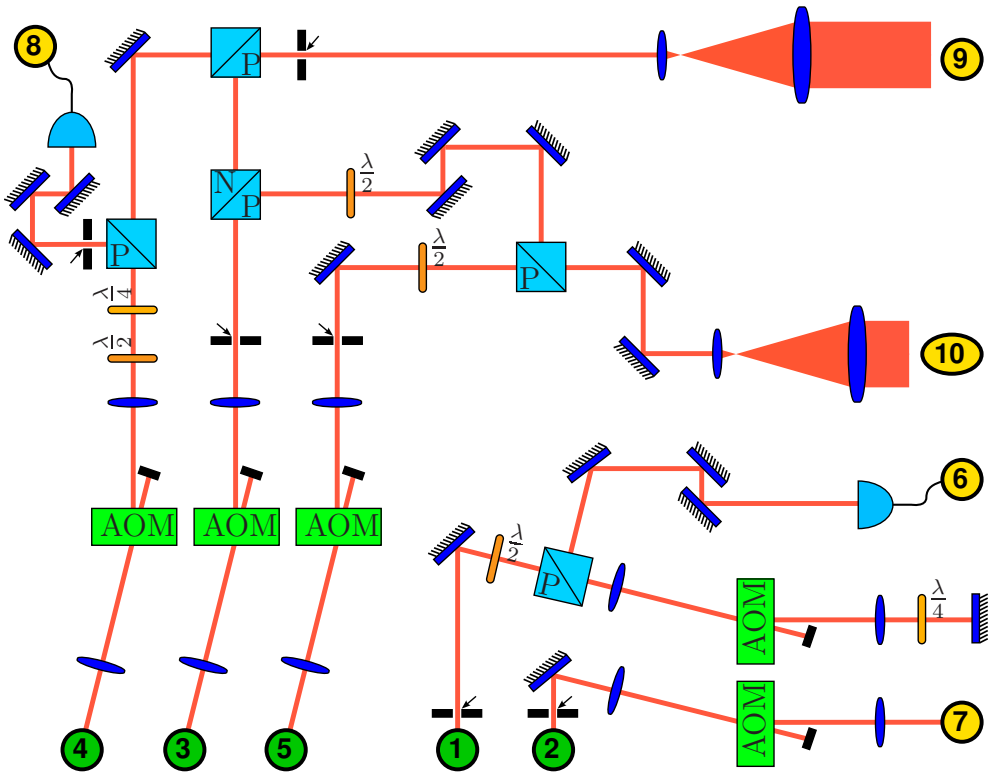

Figure 8.2: Laser light coming from the laser box (numbers 1-5, see also fig. 8.1) is guided through acusto-optical modulators (AOM, in green) in order to control its frequency and intensity; where necessary shutters are used (black units with an arrow). The treatment of light is performed also with lenses and mirrors (dark blue), polarizing (P) and non polarizing (NP) beam splitters, $\lambda/2$ and $\lambda/4$ plates (orange). The push and imaging beam profiles (6, 8) are Gaussian-shaped by passing them through single-mode optical fibers.

A Verdi solid state laser is used to pump (with 8 W laser power) a Ti:Sa ring cavity[2], visible in fig. 8.3. The output light has a wavelength of $\lambda_{Ti:Sa} = 778\,\text{nm}$, that can be easily changed of a few nanometers without noticeable effect on the output power, and an intensity of $I = 300\,\text{mW}$. After the ring resonator an optical isolator was required to avoid oscillations in the power caused by retroreflections from the fiber incoupler at the highest intensity levels.

The beam passes then through an AOM (see fig. 8.4, left) with a 200 MHz driver, that gives control over light intensity on a timescale of $0.3\,\mu s$, and is coupled into a polarization-maintaining single-mode optical fiber, that delivers at its output a 130 mW Gaussian beam.

The AOM, together with the small angular aperture of the fiber incoupling gives an extinguishing ratio of more than $\rho_{on/off} = 10^5$. The power, without active stabilization, has oscillations below 1%. The wavelength $\lambda_{Ti:Sa}$ is quite stable, and for our purposes does not need a stabilizing feedback control: with a $1-2\,\text{nm}$ detuning from resonance the relative drift during one day can be below 1%, and mode jumps are observed on periods longer than about a week. Vibrations of the laser cavity (leading to wavelength modulations and in turn to shaking of the lattice, see chap. 12) should be reduced to a minimum by the stiff construction of the unit; we expect relatively bigger vibrations in the chip mounting.

[2]Company: Coherent; models: Verdi V-10, and **899** Ring Laser

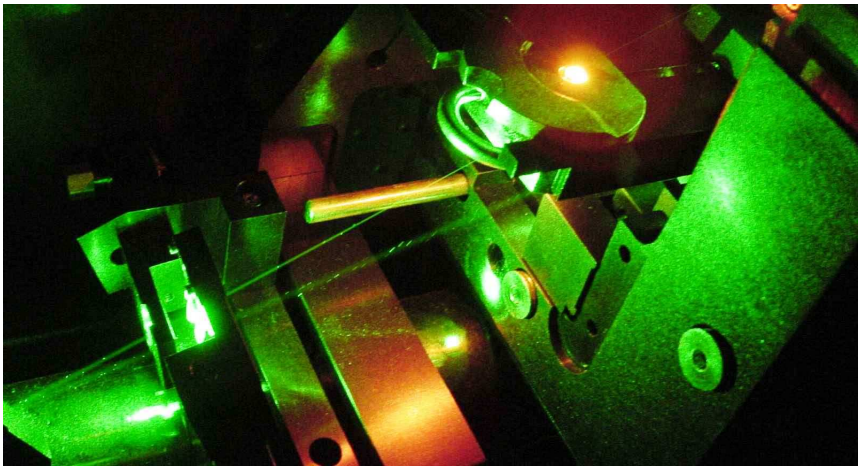

Figure 8.3: The core of the Ti:Sa laser ring cavity, with the crystal in bright green at the left, bottom.

With this linearly-polarized and far-detuned from resonance laser light we create the standing wave that generate the required potentials (see also chap. 2.5 for the physics of atoms-light interaction and 12 for the outcomes of the experiment).

A non polarizing beam splitter (fig. 8.4, right) separates the laser into two beams, that are focused by $f = 500\,\text{mm}$ lenses (spot $\varnothing = 500 \pm 100\,\mu\text{m}$) and reflected on the chip surface under a small angle $50 < \alpha < 150\,\text{mRad}$.

When using two counterpropagating beams of intensity I_0 a standing wave is created, with alternating intensity maxima and minima along the light propagation direction and a periodicity of $\lambda_{Ti:Sa}/2$. In our case (in the region immediately above the chip surface) we have effectively four beams, as both are reflected from the surface, and thus generate two other beams. This gives rise to a modulation of the standing wave intensity I_{sw} along the direction z perpendicular to the chip, with a minimum of $I_{sw} = 0$ at $z = 0$ (for the boundary conditions on the metal) and a periodicity of $\lambda_{Ti:Sa}/(2\cos\alpha)$. The maxima of the 2-dimensional standing wave lie where all the four beams amplitudes superpose constructively; it has there an intensity $I_{Max} = 16 \cdot I_0$. Assuming balanced uniform beams, perfect reflection and linearly polarized light the light field close to the surface can be described by the formula:

$$I_{sw} = 16 \cdot I_0 \cos^2\left(\frac{2\pi\, x \cos(\alpha)}{\lambda_{Ti:Sa}}\right) \sin^2\left(\frac{2\pi\, z \sin(\alpha)}{\lambda_{Ti:Sa}}\right) \tag{8.1}$$

The above formula is valid only in the case of a uniform beam. For the Gaussian profile we are using the situation is sligthly more complex. In fact the amplitudes of the four beams creating the standing wave can be different in different regions of the trap. This gives rise to a lattice of varying depth, plus a running wave whose amplitude is also space-dependent.

In our experiments we will work with a relatively short condensate, so that the lattice amplitude modulation along the x direction can be neglected for our purposes. We place the BEC in positions where the standing wave is deeper, so the running wave (generating attractive or repulsive potentials) is minimized; its effect is however negligible when compared to that of the lattice. More details on Gaussian beams reflected by a surface can be found on a previous work done in our group [116].

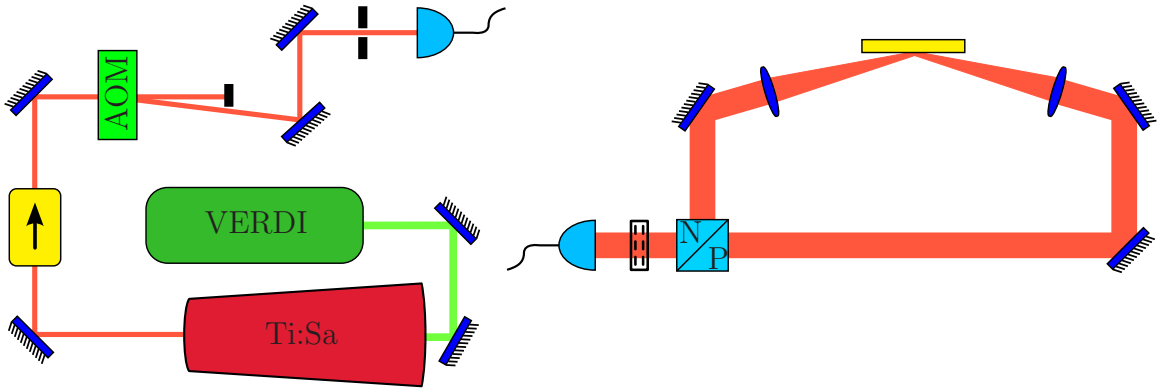

Figure 8.4: *Left*: The Ti:Sa tunable laser setup. A Ti:Sa ring laser, pumped by the solid state laser VERDI, generates the laserlight at the required wavelength. The beam goes through an optical isolator (to avoid power oscillations from back-reflected light), an AOM for intensity control, and (after passing through an iris) is coupled into a single mode polarization maintaining optical fiber. *Right*: The standing wave on the chip. Light outcoupled from the single mode fiber is passed through a polarizer, splitted by a 50/50 non polarizing beam splitter and focused on the chip by two $f = 500\,\mathrm{mm}$ lenses, with an incidence angle α.

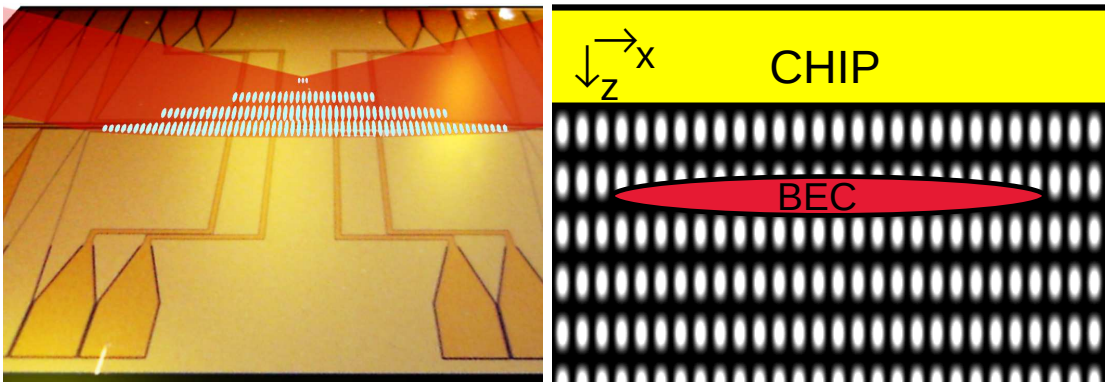

Figure 8.5: Schematic view of the standing wave reflected by the chip. *Right*: Depending on the trap position in z the BEC cloud can sit in a region of maximum or of minimum of the standing wave amplitude; if the cloud transversal size is comparable to $\lambda_{Ti:Sa}/(2\cos\alpha)$ (like in the picture) the light field acting on the atoms is not uniform along its spatial z extension.

Chapter 9

Bec: B.E.C. Experimental Control

9.1 Introduction

As already seen in the theoretical part of this work (Part I) the realization of a Bose-Einstein condensate needs a precisely defined environment. This means various parameters have to be controlled, both in value and in time evolution. We schematically summarize them in the following list:

- *Laser light.* The amplitude and frequency of various beams have to be specified and in case modulated (with acusto-optical modulators AOM and shutters). The fastest signals have a duration of only a few μs (standing wave). Jitter needs to be much lower than that value.

- *Magnetic fields.* Currents in coils and wires should be as noise free as possible; update frequencies are typically $\nu < 10\,\mathrm{kHz}$. Synchronization in the switching off requires jitter between different channels $\Delta t \ll 100\,\mu s$.

- *Atoms.* Trap frequencies of $\nu = 10 - 20\,\mathrm{kHz}$ can be achieved. To explore the dynamics of trapped atoms a time resolution of $t \ll 100\,\mu s$ is needed.

- *Duration*: the whole experiment lasts for $20 - 30\,s$. Most of the analog and digital channels need to be continuously updated for the whole experiment duration, at a frequency high enough to satisfy the previous requests.

To fulfill the requirements, a *real time* system is needed, with outputs for analog and digital signals, a sufficiently fast update frequency and the capability of driving an experimental cycle of at least $30\,s$.

The standard solution of using PCI I/O cards shows its limits, mainly because of the high noise from the PC power supplies and the cross coupling of various clock signals into the analog lines. To overcome this and other limitations, and to allow the possibility of increasing the complexity of the experiment we started implementing a different solution. A detailed description of the first realization can be found in the diploma thesis of Mihael Brajdic [117]. Here we shortly describe the structure of hardware and software, and new features implemented.

For channels requiring the highest update frequencies (the light pulses of the standing wave) we use a home-developed USB-programmable system, as explained in section 9.2. This allows to reduce the speed requirement for the whole system (only synchronization of the parts is important).

9.2 The experiment core

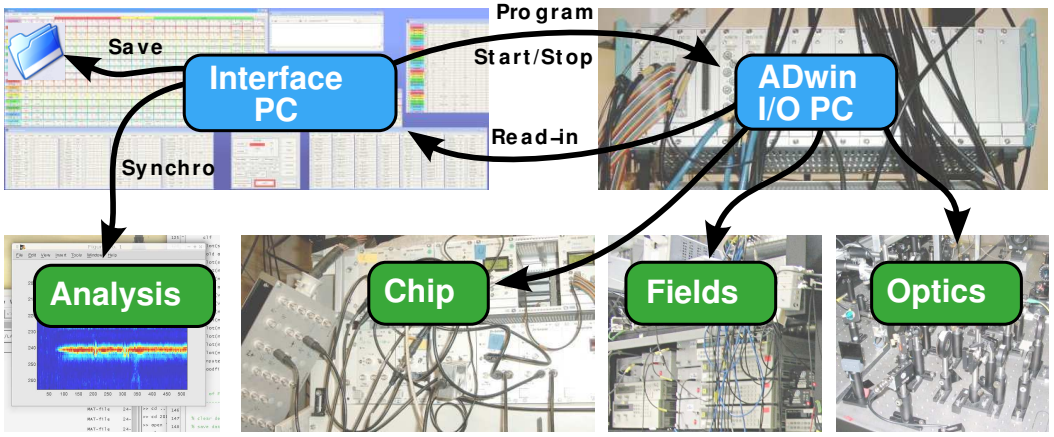

Figure 9.1: Schema of the experiment control. A PC runs the interface and saves the settings of each experimental run. It communicates also with the PC that analizes the images taken, and drives the ADwin box. This last one is the real-time I/O system that actively controls the whole experiment.

The core of the experiment is a standalone *ADwin Pro* system[1] with a SHARC-DSP processor running at 80 MHz, 512 kB cache and 128 MB RAM. The box is provided of various 16-bit 8 channel input or output analog modules and 32-bit digital I/O cards. The system can communicate with other PCs with an ethernet interface (TCP/IP protocol) and is provided of a digital input for a triggering clock. To drive the whole experiment we use another computer, where a program (*Bec*) written in *Matlab* m-files records the inputs from the experimenters in a graphical user interface (GUI). The values entered in the interface are read and converted to a proper format for the ADwin box.

At the same time, Matlab checks if the experiment runs or if it has reached the end. If it is the case it sends to ADwin the parameters for the next cycle, and triggers the start of the experiment. The data of each experiment is saved in text files. When the ADwin box receives the triggering signal from Matlab, it starts analyzing the experiment parameters and calculating the values for the first 50000 steps, putting them in a FIFO data vector. Once the FIFO is full, if the start conditions are met (see the note on triggers in section 9.3), the output voltages are driven, as requested by the experiment. A high priority process takes care of updating regularly them, while a low priority one runs in the processor spare time calculating the next ones and refilling the FIFO. At the same time a lower priority process reads and saves the analog inputs. Once the experiment has terminated, the outputs are reset to the default value, and the ADwin box awaits new data from Matlab. All the programs for ADwin have been written in a modified version of the BASIC programming language (ADBASIC). A schematic view of the software running in the PC providing the graphical user interface (GUI) and in the ADwin computer is presented in app. C, together with images of the individual GUI windows.

9.3 The interface

The control center

[1] ADwin-Pro-System, Company Jäger, Computergesteuerte Messtechnik GmbH

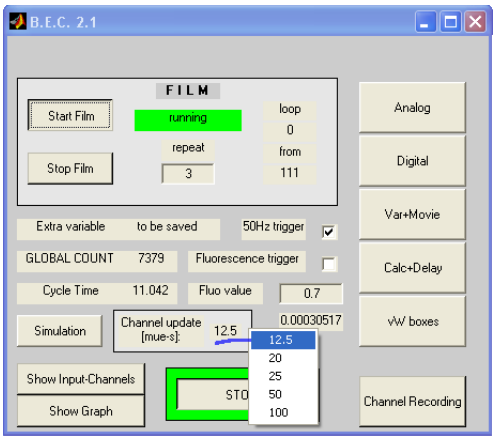

Figure 9.2: The control interface

In fig. 9.2 is depicted the control center interface. Apart from the big buttons, that toggle the visibility of other windows, many novelties introduced in the program can be accessed by the buttons in this window. A *Fluorescence trigger* is used to trigger the experiment at the beginning of the cycle. If it is enabled, the experiment remains in the MOT loading phase, until the required fluorescence intensity of the Rb cloud is reached; its intensity, converted by a photodiode, is read in by the analog card and compared with the *Fluo value* setting (in the figure set to 0.7 V). This trigger can be used to stabilize the atom number before the starting of the experiment.

Another factor that may lead to oscillations in the observed data is the 50 Hz noise from the 220 V network. In some cases it is important to synchronize the experiment with this important source of signals. However, due to the high-power loads in our lab and in the neighbouring ones, the 50 Hz has a correlation time $\tau_{50Hz} \simeq 3\,s$, so it is not possible to keep the synchronization for the whole cycle duration. The solution we adopt is to introduce a *50Hz trigger* toward the end of the RF evaporation: The ADwin box pauses, and starts reading one analog input channel, with a frequency $\nu = 20\,\text{kHz}$; when it finds a raising edge (in a signal filtered and AC-transformed from the 220 V line) the experiment can proceed.

Finally a note on time constraints. As the ADwin CPU is busy at the limit of its capacity, and to allow for extra flexibility (for example to add other analog and digital I/O cards), we updated the whole code, to allow changes of the clock frequency for the output channels. With $12.5\,\mu s$ time step we can control up to $\times 8$ channels analog inputs, 2×32 digital inputs , and read up to 8 analog inputs with $\nu_{read} = 200\,\text{Hz}$

Pull-down menus and pop-up windows, like the one to choose the channel update frequency in fig. 9.2, are accessible with the third mouse button.

The variables

Flexibility in modifying the experiment setup is given by the use of variables to define time durations and output values. Simple *variables* (now up to 60, fig. 9.3, **B**) have a numeric value and can be swept automatically to realize a *film*. A linear sweep can be easily defined by entering start/stop values and a step size in the GUI; optionally a text file can be opened (*edit manual*) where the sweep sequence can be freely defined. The variables enabled for film are swept by pressing the *Start Film* button in fig. 9.2. Moreover, 90 *Calculated variables* are also present (up to 90, fig. 9.3, **C**). Their value is calculated in a m-file that follows the Matlab syntax. Calculated variables are used, for example, to correctly re-set the timing when the overall experiment duration is varied. Another typical application is the automatic calculation and change of fields, in cases where we want to keep a fixed distance trap-chip (z) while scanning the position across the trapping wire (y). Finally we have 30 *delays*; they have a fixed value, and are used mainly to synchronize shutters with AOMs.

The signals

The interface for defining the time evolution of the various voltages (fig. 9.3, **D**) has two fields for each channel (at the left) to define a conversion slope and offset; in this way we can work with the most appropriate units (Amperes, Hz...). The whole interface is built up of an array of rectangles, with one field for defining a time duration, one for the amplitude and a small one for the curve shape. Tooltips indicate the value of the variables used, or the name of the calculated variables.

The allowed curve shapes have been extended to allow the use of splines for smooth transitions; as splines can over-/under-shoot checks are performed that the allowed ranges are not exceeded.

Variables and calculated variables are entered by choosing them from a popup menu (fig. 9.3, **F**). The digital signals are inherently simpler, so no curve shape and amplitude are defined, but only time durations before next toggle (fig. 9.3, **E**).

In all the cases where faster controls are needed, as for example for the $23\,\mu s$ pulses of the standing wave (seen in sec. 8.2), USB analog and digital modules (fig. 9.3, **G**, **H**) have been developed in house by our electronics department. The controllable update frequency can be pushed up to 8 MHz, with 16 bit resolution in the analog channels. An on-board RAM stores the data for the output signals. Being of low noise by design and thanks to battery-powering they are particularly suited for the control of the currents in the chip. The programming via USB takes a few seconds, that may interfere with the experiment (if still underway when the boxes need to be triggered). For this reason the automatic mode (running at the beginning of each cycle) can be disabled, and manual programming is done (green button).

Input recording

Apart from checking triggering conditions, as seen above, the input analog channels can be used to record signals. The data, collected by the ADwin PC during the experiment, is read-in by Matlab at the end of the cycle and can be saved for documentation, or even fed back to program *calculated variables*, for example to correct for long-term drifts. The maximum sampling frequency is at the moment limited to about 400 Hz, but the new ADwin processors (the T11 for example) and non-multiplexed A/D modules can increase that value considerably.

Signals overview

A last window shows the signals (analog+digital output) as they should be generated by the ADwin box. The vector to be sent to ADwin is used in order to plot the waveforms; in this way we test for errors in the routines converting the data of the GUI.

Below the surface

Much work has also been done in restructuring the source code. The main improvements have gone the in direction of:

- *Simplification.* All the important variables have been grouped in a single file and commented; variables naming and calls to specialized scripts improve overall code readability.
- *Flexibility.* The number of analog (1 to 4) and digital (1 or 2) cards can be changed by modifying a few flag variables. The same applies for the USB boxes. The GUI and the communication with ADwin are automatically handled.
- *Portability.* The software is now used in various experiments in our group. Changes have been done to improve the portability and adapt to different setups. The software runs now on both Windows and Linux, and in a test mode even without the ADwin box connected.

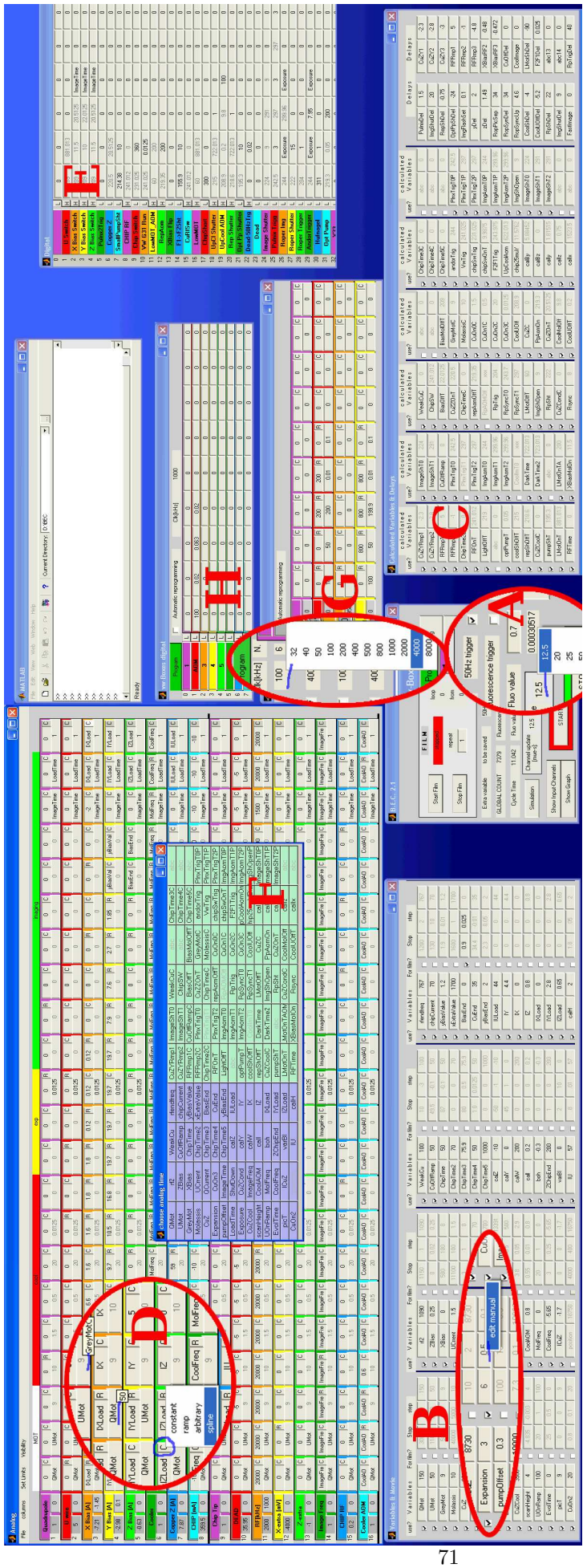

Figure 9.3: The complete GUI to control the experiment.
A: the control center. On the zoom the pull-down menu to choose the clock update time and the experiment triggers.
B: the variables; with the film step set to zero a m-file is read to set the film sequence.
C: the calculated variables/delays interface.
D: the analog channels matrix. In the zoomed area: spline signals have been added; variables (QMot) have a popup indicating their value; calculated variables have a popup indicating their name (GreyMotC).
E: the digital channels matrix.
F: the pop-up window to select variables/calculated variables for the channels.
G: the interface for the USB module analog channels, with pull-down menu for selecting individual clock frequencies.
H: the interface for the USB module digital channels.

Part III

RESULTS

Chapter 10

Measuring (with) atoms

The first chapters of this work covered the physics of the condensate, describing how to obtain it and what are its characteristic features (dimensions, oscillation frequency, expansion behaviour, chemical potential,...); a section follows, relating on the experimental apparatus (vacuum, fields, the chip, software). We do not know yet what are the procedures to actually measure physical quantities from a small, cold atomic cloud: this will be the subject of the current chapter.

10.1 Experimental cycle

The first thing we do when we start the experiment is switch on the rubidium dispenser on the lower MOT: a current heats it up releasing a gas of Rb atoms. The gas builds up in the chamber; already after a few seconds we have enough rubidium and we are in principle able to Bose condense. We now turn on the magnetic field of the lower MOT.

The lasers are then checked; if the power is too low (due to drift in the optics alignment) they need to be readjusted, after which we proceed to lock them on the required wavelengths.

At this point we should have a MOT in the lower chamber, and we are ready to proceed to what is the experimental cycle.

1. The fields (B_y and that produced by thecurrent in the copper $\boldsymbol{Z}$) and lasers for the upper MOT are switched on.

2. The push beam is turned on; atoms ejected from the lower MOT start to load the upper one.

3. When $1 - 2 \cdot 10^8$ atoms have been collected (in typically $10''$) the push beam is removed.

4. Fields are ramped up (60 ms), to compress the atoms and increase the density in the region where the magnetic trap will be located.

5. Fields are removed. In this phase (10 ms) the dissipative force of the laser light cools down further the compressed atom cloud; this phase is named *optical molasses*.

6. The lasers are switched off; then B_y is turned on again, to define a quantization axis for the atomic spin. We shine now a short pulse (100 μs) of σ^+ polarized light, to pump the atoms in the $F = 2$, $m_F = 2$ spin state; this process is called *optical pumping*. The whole step has a duration of 1.5 ms

7. Now the *magnetic trap* is created, by letting current flow in the copper $\boldsymbol{Z}$. The current reaches a value of 50 A in about 150 μs, at which point the trap is formed with its minimum where the ultracold atom cloud is located.

8. We start then to evaporate the atoms: the RF signal takes 12 s to go from 32 MHz to its final value of about 750 kHz.

9. At the same time we *close* the magnetic trap: compressing the atoms by increasing the trap frequencies has the effect of speeding up the rethermalization rate, enabling a more efficient evaporation process. As the cloud size reduces, we can move the trap closer to the surface, making easier to load the atoms on the chip. During the whole evaporation process for every factor k of decrease in the temperature we loose almost the same factor in atom number. We end up with $0.5 - 2 \cdot 10^5$ atoms in the condensed state.

10. Currents are now ramped up in the chip wires; we reduce synchronously that of the $\boldsymbol{Z}$, and accommodate the fields accordingly. If the trap parameters vary smoothly and slowly enough we have a BEC trapped on the chip in $100 - 500$ ms.

11. If necessary we apply other RF evaporation phases, to remove atoms that may have been excited in the process. We perform then the experiment on the chip, by moving the BEC to the desired position and stimulating it with proper signals.

12. The BEC is then released. After a variable free fall time an absorption image of the cloud is taken. The experimental cycle starts again.

10.2 Imaging

The ultracold BEC cannot be accessed for sampling with any real detector: any solid state device of dimensions around the μm is composed by about $N = 10^9$ atoms, a factor 10^4 more than the BEC, and (apart for the difficulty of using something of that sort to sample a gas) it would immediately heat the BEC, before being able to measure anything.

If we cannot measure with atoms, we can still use photons; at the end we already have lasers for cooling and trapping. Moreover their wavelength is defined with a precision better of 1 MHz, a factor already 6 times better than the ^{87}Rb optical D2 transition (see app. B). With such a high quality light source, it is possible to access the imaginary index of refraction of the atom (for a dilute system, where $|n_{ref}| \simeq 1$, and low light intensities):

$$n_{ref} = 1 + \frac{\sigma_0 n \lambda}{4\pi} \left(\frac{i}{1+\delta^2} - \frac{\delta}{1+\delta^2} \right) \tag{10.1}$$

with δ as the detuning from resonance, n as atom density and $\sigma_0 \simeq 6\pi\lambda^2$ as resonant cross section.

Various methods have been developed to image an atomic cloud, based on the imaginary part of n_{ref} (*Absorption imaging* and *fluorescence imaging*) or on the phase delays introduced by the real part of n_{ref} (*Dark ground imaging* and *phase contrast imaging*); a review can be found on [118].

The method we are employing is the most widespread one, the absorption imaging. By operating on the *acusto-optical modulator* (or AOM, see more details on the laser system in chap. 8) we can tune the imaging light exactly on resonance; this is done by finding the maximum in the absorption through a Rb cloud. In this case we have $\delta = 0$, and the equation above simplifies. The light, propagating along the y direction across the atomic cloud will experience an attenuation of the factor:

$$t_{att} = e^{-\tilde{D}/2} \qquad \text{with} \qquad \begin{cases} \tilde{D} = \tilde{n}\sigma_0 \\ \\ \tilde{n} = \int n \cdot dz \end{cases} \tag{10.2}$$

where $\tilde{D}$ is the on-resonance optical density and $\tilde{n}$ the column density. The observed attenuation t_{att} is then sufficient to derive $\tilde{n}$, the density integrated along the light propagation direction.

Having to deal with a microscopic cloud[1] it is important to have an imaging system with enough resolution; in our system we use as imaging light a *Gaussian beam* ($\varnothing \simeq 2\,\mathrm{mm}$) outcoupled from an optical fiber, and a telescope with a magnification of up to 7, with a first achromatic lens at $f = 100$ mm from the condensate. Spatial resolution is about 3 μm.

The light passing through the atoms is subsequently collected by a *CCD* camera, cooled to $T = -40\ ^\circ C$ to reduce at the minimum its noise floor. Depending on the camera type used[2,3] we have about $2-3$ μm/pixel. The camera type has to be chosen with attention to its noise floor and to its quantum efficiency at the used light wavelength.

The BEC lie quite close to the chip surface (their mutual distance is $z \simeq 1-500$ μm); to image it we send the light beam at an incidence angle of $\alpha \simeq 10$ mRad [90]. The reflection on the surface produces also a mirror image of the cloud (see schema on fig. 10.1). For small α the distance between the two images is equal to $2z$, and a direct measure of z is thus possible.

In fig. 10.1 most of the characteristic features of the atom detection are visible:

- The picture on the left shows the beam profile, with some shadows on the upper part due to various atomic clouds. The big fringe above is caused by diffraction and interference from the chip wires; periodic fringes like those on the lower part are generated by diffraction from the sharp chip edge or by interference between the imaging beam directly coming into the camera and part of it reflected from the chip. Defects (probably on the chamber window out of the focal plane) create the diffraction rings.

- The central picture is taken after 7 ms , and contains all the necessary information on the beam profile but no atom shadow. If we divide the first image by this one we recover the attenuation factor t_{att}, and can invert eqn. 10.2 to recover $\tilde{n}$. In order to minimize the beam intensity, profile and position oscillations the two pictures have to be taken with the minimum time delay, by speeding up the processing of the image in the CCD. At the fastest speed possible the noise level of the camera is increased in a band passing for the beam maximum, so we image the atoms elsewhere.

- The processed image shows the atoms and their reflected image; the noise floor is higher where the light levels have been lower.

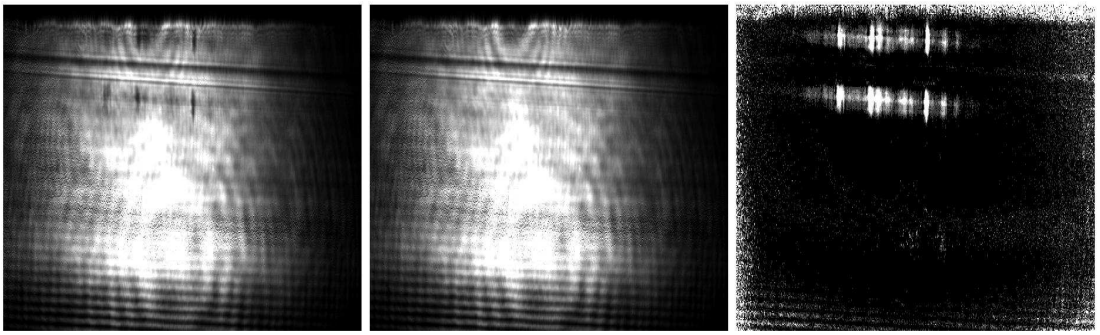

Figure 10.1: Atom absorption image (left), beam profile (center) and processed data, showing the BEC cloud; each picture is 1100×500 μm, in the horizontal and vertical direction respectively.

What said above is valid only grossly, and a proper calibration of the imaging sensitivity has to be performed. The factors influencing it can be summarized in the following points:

[1] although the cloud has a longitudinal dimension that can be of up to 1 mm, its transversal size is of the order of 1 μm.

[2] Company:Roper Scientific; model: TE/CCD1152-EM/1

[3] Company:ANDOR DV435-BV-958; model: TE/CCD1152-EM/1

- *The scattered light* (spontaneously emitted after the first excitation) is partly reabsorbed by other atoms, reducing the attenuation of the original beam.
- *The scattered light* is also collected by the imaging system, further reducing the amplitude of the absorption signal; in the limit of a lens close to the atoms (small F number), necessary to have a good spatial resolution, up to 50% (2π solid angle) of the emitted light is collected.
- *The light intensity* has to be kept high, in order to minimize the statistical noise. Moreover the photons scattered by each atom N_{sc} give it a diffusion velocity $v_{diff} = \sqrt{N_{sc}} v_{rec}$ that blurs the image: a short imaging time (high intensity) is preferable. For such reasons it is easy to move close to the saturation intensity I_s, where eqn. 10.2 is no longer valid.
- *The chip* reflects at an angle α the imaging beam (of wavelength λ), creating a beam standing wave parallel to its surface (see schema in fig. 10.2 left), with periodicity $a = \lambda/2 \sin\alpha$; in the minima there is no light, while in the maxima it is 4 times the beam intensity, causing a modulation of the perceived atom number, depending on their position relative to the fringes.

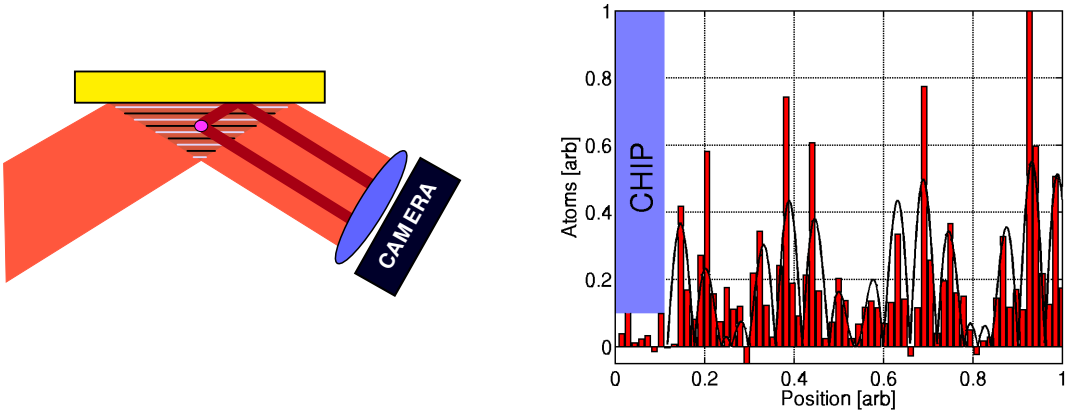

Figure 10.2: *Left*: the light, incident from the left, is reflected by the chip, creating a standing wave parallel to it; two absorption shadows (one direct, one from the reflected light) are generated and recorded in the camera. *Right*: Apparent atom number modulation (beating) due to two beams with different reflection angles α and α_1 (see text). Black continuous curve: fit with the trial function $Atoms = a \cdot |\sin(k_1 z + \phi_1) \sin(k_2 z + \phi_2)|$

In order to show this last effect we added a second beam to pump the atoms out of the imaging transition, and aligned it as the imaging beam, but with a higher incidence angle $\alpha_1 > \alpha$; we look at the atoms in the trap (*in situ*), for various positions z. The measured atom number shows a beating, with the periodicity expected from the measured α and α_1.

One last thing: in order to derive the atom number N, eqn. 10.2 requires the knowledge of a scale factor, implicit in the densities: the number of micrometers per pixel. One possibility of calibrating the imaging system magnification would be, where applicable, to image a geometric pattern on the chip (a wire, two bondings) whose size is well known. A different procedure, that we are regularly using, is outlined in sec. 10.6.

10.3 Trap frequencies

When atoms are trapped magnetically (sec. 2.3), the more important parameters that influence their behaviour are the trapping frequencies $\nu_\perp$ and $\nu_\parallel$, defined at the minimum of the local (harmonic) potential.

A first possibility for their determination is the perfect knowledge of the structures generating the magnetic fields (wires and coils) and of the current flowing in them. However, a direct assessment is desirable, and can be used to cross-check if the calibration for the fields is correct.

The most obvious way for measuring them is perturbing the trapping potential, and then observing the oscillations induced in the atom cloud; working with a BEC has the advantage that the stimulated oscillations are coherent and decay very slowly compared to the case of a thermal cloud. Measuring a transversal frequency of a few kHz for a few seconds can lead to very precise frequency determinations, and drifts caused by particular effects (like *Van der Waals* interactions close to a surface) can be evaluated.

The easiest frequency to be measured is $\nu_\perp$. For $\nu_\perp = 1$ kHz we have a transversal extension of the oscillator ground state below 1 μm, so an *in situ* observation is not an option. But oscillation velocities $v_\perp$ of a few mm/s are easily reached: this suggests the possibility of imaging the transversal *momentum* of the cloud; if we suddenly switch off the fields, after a variable oscillation time in the trap, and let the atom free fall for a time t_{TOF} (TOF, time of flight) the vertical position of the cloud in respect to the unperturbed case will be proportional to $v_\perp(t) \cdot t_{TOF}$, where we indicated with $v_\perp(t)$ the velocity of the BEC in the trap at time t.

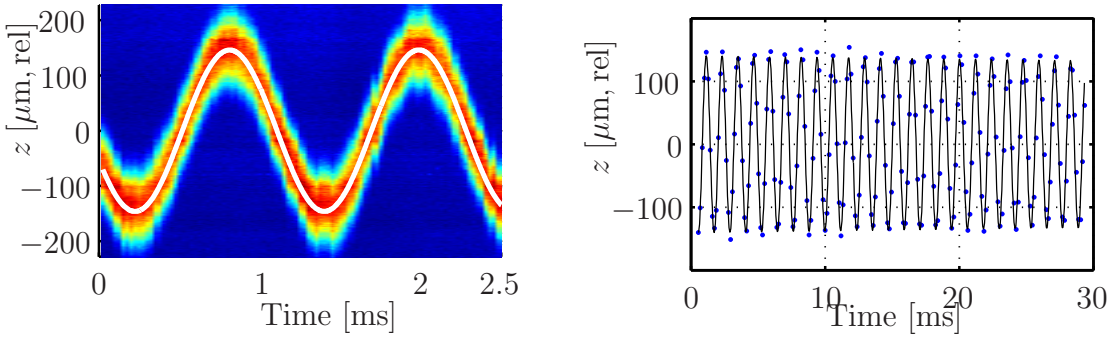

Figure 10.3: Transversal oscillations. *Left*: a sequence of around 100 experiments for an oscillation time in the trap of $0 < t < 2.5$ ms after the excitation pulses; each vertical slab corresponds to the atom density along z, after integration along the other direction y (by the orientation of the imaging system) and x (numerically from the images); the white line is a sinus fit. *Right*: the same oscillation observed for longer time (30 ms). Atoms have been imaged after a $TOF = 14$ ms.

A sequence of experiments, represented in fig. 10.3 shows the measure of oscillations in the *copper-Z* trap, (sec. 6.4) with a current $I_Z = 37$ A, an external field of $B_y = 71$ G and a trap bottom of 740 kHz[4]. The fit returns $\nu_\perp = 844.22 \pm .19$ Hz, consistent with the simulations of the trapping fields. We observe an attenuation of the visibility with a time constant of $\tau = 247 \pm 73$ ms; however we stimulated the oscillation with a single cick in the trapping wire current, and it is possible that other high lying modes have been excited. By employing a smaller perturbation and repeating it with the correct frequency the oscillation decays more slowly. Also the presence of thermal non condensed atoms reduces the coherent oscillation duration; this is easily verified in experiment, by changing the final RF evaporation value (and thus the sample temperature).

The longitudinal frequency $\nu_\parallel$ can be a factor 1000 smaller than $\nu_\perp$, and that gives for the excited center of mass velocity $v_\parallel \simeq v_\perp/\sqrt{1000}$ (order of magnitude). As the condensate is also much longer along x we do not have a big signal (oscillation/length). But we can modulate the trap bottom, changing thus $\nu_\perp$ and squeezing the BEC along x. As a result a *breathing mode* is excited (see sec. 3.5.1).

[4] the units used although not SI have widespread adoption in the field. In particular the trap bottom is found at the end of the RF cooling, and is thus directly readable in the instruments as frequency value; it can be converted to Tesla considering the magnetic coupling strength: $\hbar\omega_{RF} = g_F m_F \mu_B B_y$.

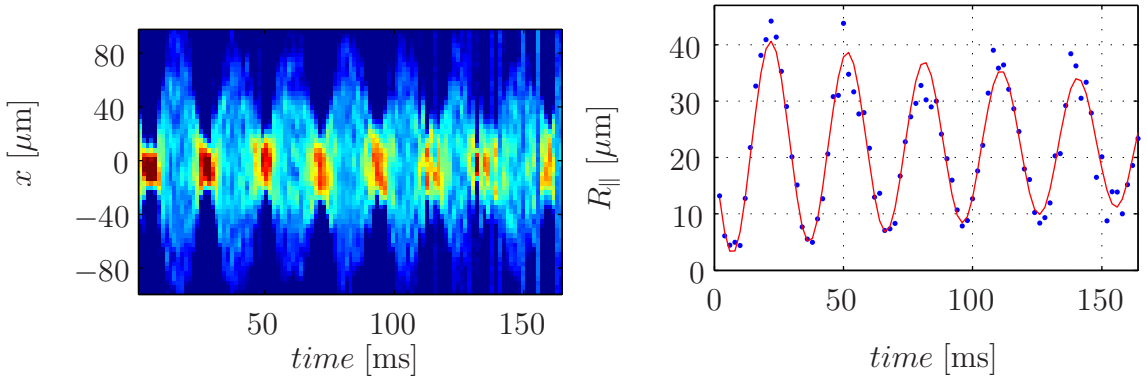

Figure 10.4: Breathing mode. *Left*: a sequence of around 80 experiments for an oscillation time in the trap of $0 < t < 160$ ms; each vertical slab corresponds to the atom density along x, after integration along the other direction y (by the orientation of the imaging system) and z (numerically from the images). *Right*: the condensate halfwidth (blue dots) with a superposed fit (red curve).

Figure 10.4 shows how the BEC longitudinal size changes for different trapping times after the perturbation. From the left image (longitudinal density of atoms n_1 developing in time) we can get a clear visualization of the process. The fit of the BEC widths shows a damped sinusoidal trend, with frequency $\nu_{breath} = 33.65 \pm .20$ Hz and damping time constant $\tau = 269 \pm 90$ ms. Due to the factor $\sqrt{2/5}$ (sec. 3.5.1, [65]) this gives us $\nu_{\|} = 21.28 \pm .12$ Hz.

10.4 Field calibration

We mentioned above that the trap frequencies (and the condensate position in space) can be calculated once we know the magnetic fields. These are in turn determined by a measure of the currents used and by the knowledge of the geometry of the current-carrying structures.

Part of this procedure consists of knowing exactly the currents flowing I_j, in dependence of the control voltages. In absence of a feedback to stabilize I_j (see sec. 6.2) the dependence of them on the control voltages can be far from linearity (fig. 10.5, left), mainly due to the electric properties of the switches integrated in the loop[5]

We measured the V-I response for the coils and the wires (green curves in fig. 10.5 for the coils giving the fields B_z and B_y along the directions z and y), and fitted these values with a trial function derived from the knowledge of the electrical elements in the loop (black curves).

As next step we trapped cold atoms close to the chip, with various currents I_z on the coil for the bias field along z; changing I_z rotates the trap position around the trapping wire, and changes the distance z, which we measured (blue dots in fig. 10.5) The shift of the maximum to $I_z = 0.39$ A is due to a not completely cancelled stray field, that can be compensated (if desired) with extra coils we integrated for this purpose (they should compensate the earth magnetic field). The red dashed line on the figure shows the position expected, and is obtained by a simulation of the current-carrying structures with the currents used in the experiment. The only free parameter was the zero of the field along z.

This calibration procedure is very important in view of the measurements described in 11.2.3. It is used for example to calculate the fields needed to scan the trap position horizontally (along y) while keeping the same z. The red markers in fig. 10.5 show the current values used in the coils for B_y and B_z for this purpose.

[5]IGBT switches; Company:RS; Model: IRG4PH505

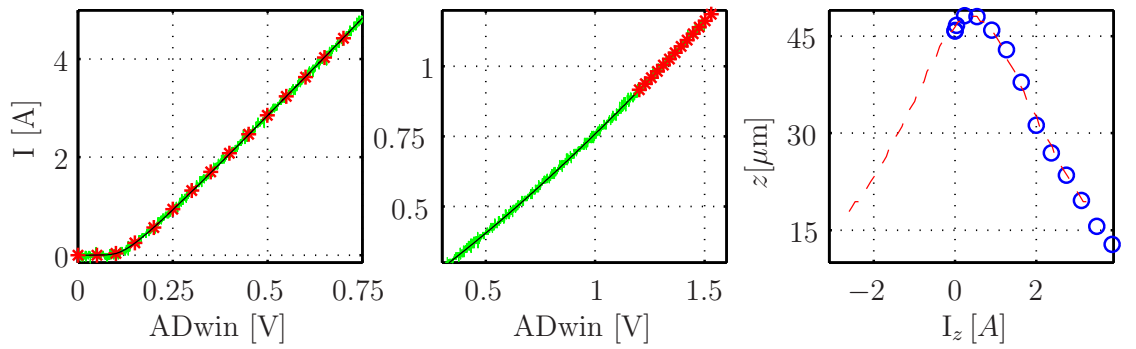

Figure 10.5: Currents calibration. *Left, (center)*: Currents in the coils for the fields along z (y), against the control voltage; green curve: measured current; black line: fit; red dots: settings used to have a trap at a constant z. *Right*: distance atom-chip z in dependence of the current on the coil for the bias field along z.

10.5 Trap bottom stability

For having a good accuracy in the experiment results, another important thing to control with absolute precision is the trap bottom: in fact this has an influence on the transversal trap frequency and on the atom number. The RF frequency used for evaporating the atoms (sec. 2.4) has an end value usually around $RF_{end} = 750$ kHz, and the chemical potential of the condensate is around $\mu = 5$ kHz. If we want to have an atom number N constant to within 10% then, due to the relation $N \propto \mu^{5/2}$ (In the Thomas-Fermi approximation in 3D condensates) we need an accuracy of the 4% in μ, corresponding to $\mu = 5000 \pm 200$ Hz.

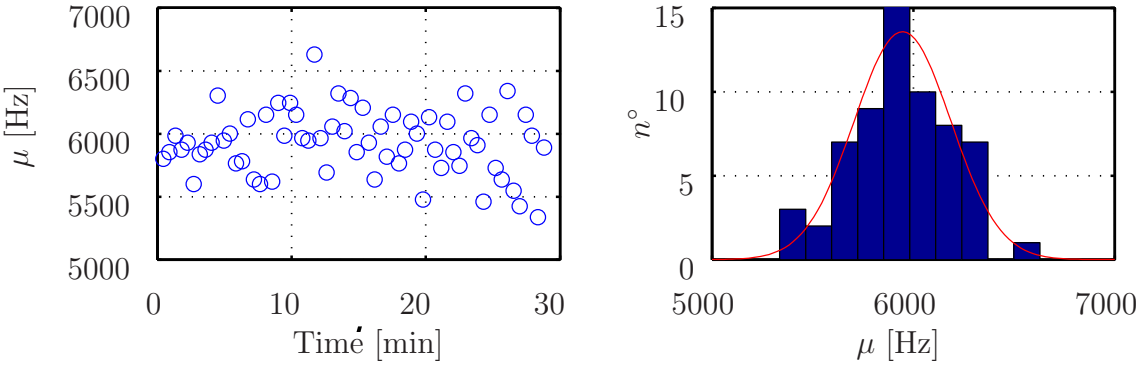

Figure 10.6: Trap bottom stability. *Left*: measured chemical potential during 30 min of observation, corresponding to 66 experimental realizations. *Left*: Histogram of the measured μ, grouped in 10 bins, with superposed a Gaussian fit (red curve).

We realized a BEC in the 3D Thomas-Fermi regime ($\mu \simeq 6000$ Hz, measured setting the RF end frequency 6 kHz above the trap bottom of $\nu_\perp = 840$ Hz). From the fit of the BEC longitudinal width and the knowledge of $\nu_\parallel$ we derived a mean value of μ consistent with the RF observations. The standard deviation $\Delta\mu = 240 \pm 80$ Hz is close to what required. The time drift (during the 30 minutes of the observation) is compatible with zero. A plot of the results can be seen in fig. 10.6

The stability of μ was done by observing the atoms immediately at the end of the main cooling process (see figures in sec. 2.4), using only the copper $\boldsymbol{Z}$ as trapping structure. In this situation oscillations in the trap bottom are due to noise in all the coils and in the trapping wire currents. The previous measurement was done after the implementation of the feedback control of the currents

in the $\boldsymbol{Z}$ and in the y bias field, and confirms it is functioning correctly. Performing tests after allowing the BEC to reach dynamic equilibrium (by keeping it in a constant trap with a RF shield to remove the excited particles) we were able to measure a stability of about 100 Hz. Compared to the value of RF_{end} it corresponds to a long-term stability of one part in 10^4.

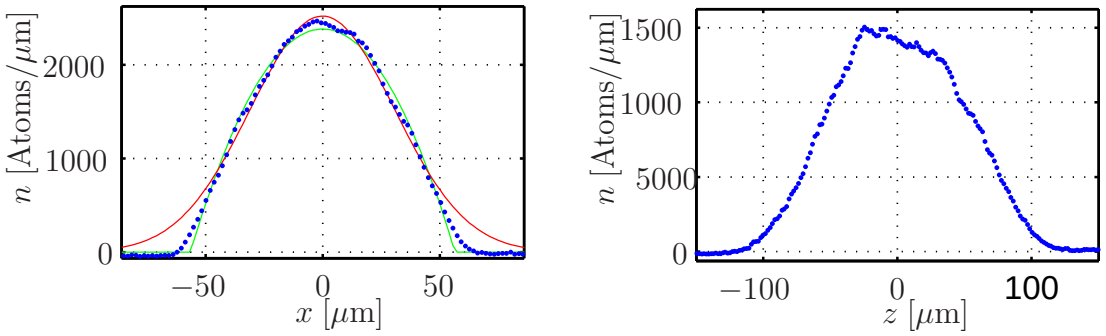

Figure 10.7: *Left*: columnar atom density along x (blue dots), and fit with a parabola (TG regime, green curve); red curve shows for comparison what expected in the case $\mu \ll \hbar\omega_{\parallel}$. *Right*: columnar atom density along z; broadening of the maximum due to long exposition time and non perfect synchronization in the fields switching off (Stern-Gerlach).

The chemical potential can be derived from an image of a condensate in two different ways; the one we used above was measuring its length along the longitudinal direction x, by fitting the 1D density n_1 with an inverted parabola. Fig. 10.7 left shows the data (blue dots), plus a parabolic fit (green curve) expected from TF approximation, and a Gaussian to show the situation expected in the case $\mu \ll \hbar\omega_{\parallel}$.

The image on the right represents the columnar density along z; as we have $\mu \simeq 7 \cdot \hbar\omega_{\perp}$ (as seen above) we should expect a profile described by TF theory; however the tails are smooth, as in the case of a Gaussian, and the width corresponds to a value of $\mu = 9.7$ kHz, higher than the data obtained from two independent measurements (RF spectroscopy and longitudinal size/potential relation). Two are the causes for this observation, and must be taken into account in all the observations we perform:

- The relatively long time of flight $TOF = 14$ ms, coupled with an imaging time of $t = 300$ μs causes a moving of the BEC during observation of $\Delta z = 41$ μm, that blurs the image, and in particular the edges, causing the smooth transition.

- At the moment of releasing the atoms if there is a delay between the switching off of B_y and of the $\boldsymbol{Z}$ a field gradient can be created at the position of the atoms; if this process is fast (compared to the timescale given by the *Larmor frequency* $\omega_l = B_0\mu_B g/\hbar$), and the new field is no longer aligned with x we get a projection of the atomic spin to the various m_F and each substate will be accelerated differently. In time the velocity acquired leads to a different position of each spin component. Such an effect (too small here for having a spatial resolution of the various components) can cause a broadening of the cloud size with the flattened feature observed on the top the plot in fig. 10.7, right. Reducing the width of the figure of a value equal to the half size of this top feature gives a μ compatible with 6 kHz.

10.6 Stern-Gerlach experiments

The Stern-Gerlach effect observed above can be avoided by a proper synchronization of the fields' switching off, but can even be enhanced, so that we can resolve the different spin components.

In a first series of experiments with a thermal cloud we opened for a short time the switch for the B_y field, causing a fast negative spike in the current modulus, followed by a slow recovering of the previous current value (limited by the speed of the power supply). The atoms are thus projected in the various spin states, and are then taken adiabatically to the previous trapping conditions, allowing the spin to follow. The spin projection is associated with a center of mass displacement, that causes oscillations of the clouds in the trap.

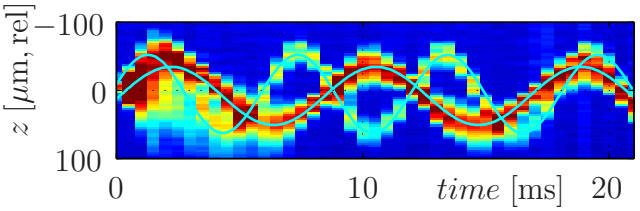

Figure 10.8: Center of mass oscillations of various spin components in an atomic trap. Cyan curves: sine functions, as guide for the eye, whose frequencies have a ratio of $\sqrt{2}$. TOF imaging.

As can be seen in fig. 10.8 there are clearly two trapped spin states ($m_F = 2$ and $m_F = 1$) that oscillate in the trap at different frequencies; the cyan lines are guide for the eye, and the ratio of their frequencies has been chosen $\rho = \sqrt{2}$, as expected from theory. Untrapped spin states leave the trap during the first 5 ms, and contribute to the higher background signal observed in the left part of the graph.

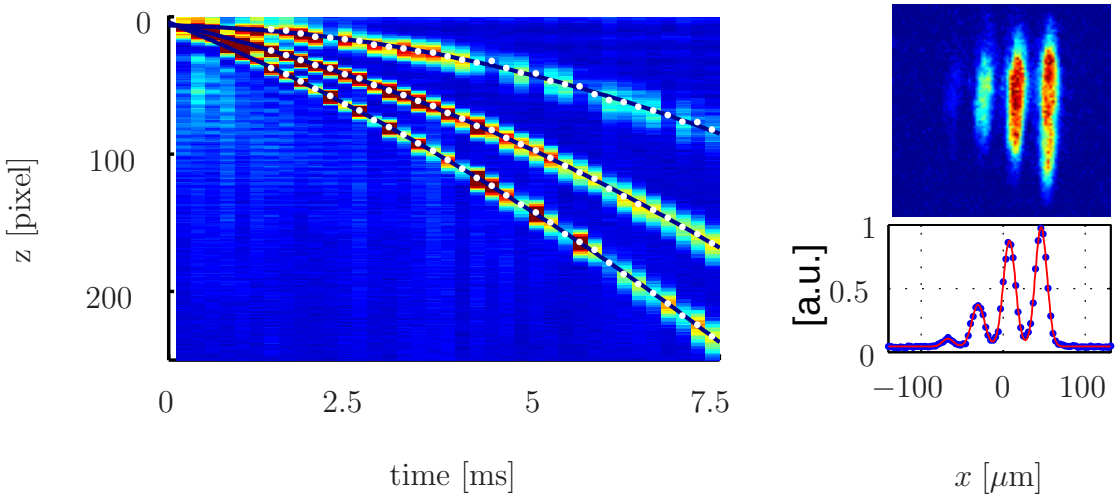

Figure 10.9: Stern-Gerlach experiments on two perpendicular directions. *Left*: a TOF sequence of three different spin states; white dots: fitted central position of the clouds; blue curves: fit with a free-fall equation of motion, using the same acceleration for the three curves. *Right*: single shot of a Stern-Gerlach experiment along the x direction (picture size is 270×250 μm). Lower graph shows the 1D atom density (blue dots) with a fit of four Gaussian (red curve); one spin component has zero population.

In a second series of measurements we performed a pure Stern-Gerlach experiment and observed the different spin states after a variable $0 < TOF < 7.5$ ms. Fig. 10.9, left, shows the time evolution of the three detected m_F populated states. Here the BEC center of mass positions along z, for every measured TOF have been derived with a fit (white dots). Then their values in time have been fit with a free fall equation of motion, using the same gravitational acceleration for each spin component; initial position and velocity have been left as free parameters, to include the effect

of the non-linear m_F-dependent acceleration at the beginning of the fall. The blue curves is the resulting fit, and shows excellent agreement with the data points. By entering in the equation of motion the local gravity acceleration we can use the measurements performed to estimate the spatial resolution of a CCD pixel. The previous experimental series gives $\Delta z = 3.91 \pm 0.19$ μm/pixel. Avoiding to perform a Stern-Gerlach experiment, with the strong non-linear acceleration regime at the beginning and observing the fall for longer times (up to when the BEC goes out of the visible region) we can increase the precision of the calibration, with relative errors around 1%.

We are not limited to performing spin splitting along a single direction. A copper wire perpendicular to the trap axis has been used in a last test, to provide a field along z with a gradient in x; again, the procedure used to project the $m_x = 2$ state to different spin states along another direction (z) is a varying sequence of fast (diabatic) and slow (adiabatic) magnetic field reorientations, with which we respectively project and rotate the spin components. After a sufficient TOF we can observe four BEC clouds (see fig. 10.9, right; one of the five possible spin states is not populated); as the copper wire is quite far away from the BEC (in respect to the transversal separation of its spin components) we can assume the field gradient is constant in the region where the experiment is performed; this leads to a linear separation of the spinor BEC. From a fit with Gaussian trial functions of the 1D atom density along x we get a separation between the clouds of $\Delta x = 37.5 \pm .5$ μm

10.7 Drifts

There are many other sources of errors and of drifts in such a precise and delicate experiment. As only example we take a drift in the atom cloud position observed over a two hour period. The shots were taken in the morning, after switching on the experiment. The shift does not show a damping during the two hours of observation, and we may expect it to affect the experiment over a long period. As the temperature in the lab is relatively stable (to better than $1°C$ over the whole day) we can attribute it either to temperature dependent dilatation in the chip mounting and in the chamber (due to the ohmic heating of the currents flowing) or to mechanical relaxations (maybe in the imaging optics).

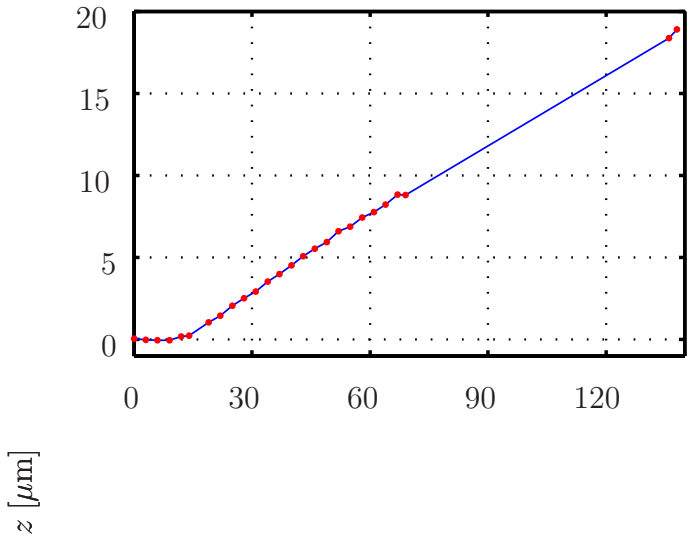

Figure 10.10: Cloud position drift, in situ imaging; blue curve as guide for the eye.

To reduce the effect of this and of other drifts, various countermeasures are regularly taken.

- The experimental loop is kept at the required settings for a sufficiently long period, in order for transients to settle. Then measurements are taken.
- Disturbances are reduced to a minimum; even a person moving in and out of the lab can perturbate the environment: interferometric measurements show that the chip mounting can oscillate in the kHz regime if vibrations (even sounds and voices) are present. The automation of data acquisition and experiment control is a great help in the situation (see sec. 9.2).
- If we scan a variable linearly during the experiment, then unwanted drifts will be embedded in the measurements and can easily go unnoticed. Choosing the correct sequence for the different experimental conditions we can remove the influence of linear drifts (similarly to what is done in the design of digital integrated circuits to match above the technological tolerances couples of elements).

Chapter 11

Sculptured wires

We have already seen in chapter 7 what the main characteristic of our atomchips are. We present here a method we devided [119, 120] to go beyond what the production technology offers, and analyze some of the fields that can be realized.

11.1 F.I.B.

There is the possibility of machining the deposited metals also after chip fabrication. In particular we used a *Focused Ion Beam* machine (FIB for short) to cut through the metal. A thin ion beam, with diameter down to about 10 nm, accelerated by an electric potential of some tens of kV, can be used to dig into the gold sheet. We can for example make a hole of the desired geometry, or cut a slab from an edge.

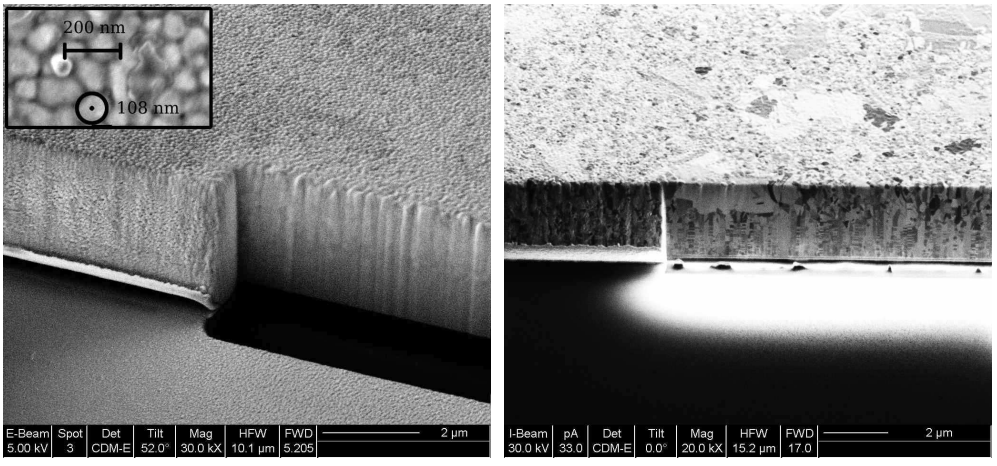

Figure 11.1: Two gold sheets FIBbed along an edge; *left*: electron microscopy showing the columnar structures formed on the cut edge for a too high ion beam current; insert to show the typical size of the gold grains constituting the wire; *right*: another FIBbed wire, imaged by collecting the scattered ions of a low intensity scanning ion beam; contrast is given by changes in the ion reflection coefficient, and is strongly dependent on the gold nanocrystal axes orientation.

In fig. 11.1 left, a first test shows that the polishing of the wire edge rugosity does not really work: a columnar pattern is visible on the left part of the image, where the edge has been cut. Choosing a too high ion beam current had the effect of projecting the gold grain structure on the top edge of the sheet all the way down to the chip surface. In the insert a particular of the top face gold grains (pictures obtained by electron microscopy).

The image on the right shows a different landscape: it has been obtained by scanning the ion beam on the sample, and the gray level is a measure of the ion absorption rate. The polishing looks better now. Various columnar structures are visible, that show how the layer grew from the initial gold grains in contact with the titan adhesion layer. Moreover there are some 'islands' of length up to $2\,\mu$m. The differences in the ion absorptivity depend strongly on the orientation of the gold nanocrystals. The relative orientation between neighbouring grains influences also the electron conductivity [121], and eventually poses a limit in the homogeneity of the current flows.

The FIB technique is used extensively in the microelectronic industry for chip inspection (quality and failure analysis), and has applications in many more fields. Usually gallium is used to etch, and platinum can be deposited. An overview on the technology can be found in [122].

11.1.1 Polishing

The first operation we did with the FIB on the atom chip was polishing the edges of a gold plane conductor. The conductor is in this case a thin $\boldsymbol{Z}$ structure of length $l = 2\,$mm, width $w = 10\,\mu$m and thickness $t = 2.5\,\mu$m; for simplicity we will call it *wire*.

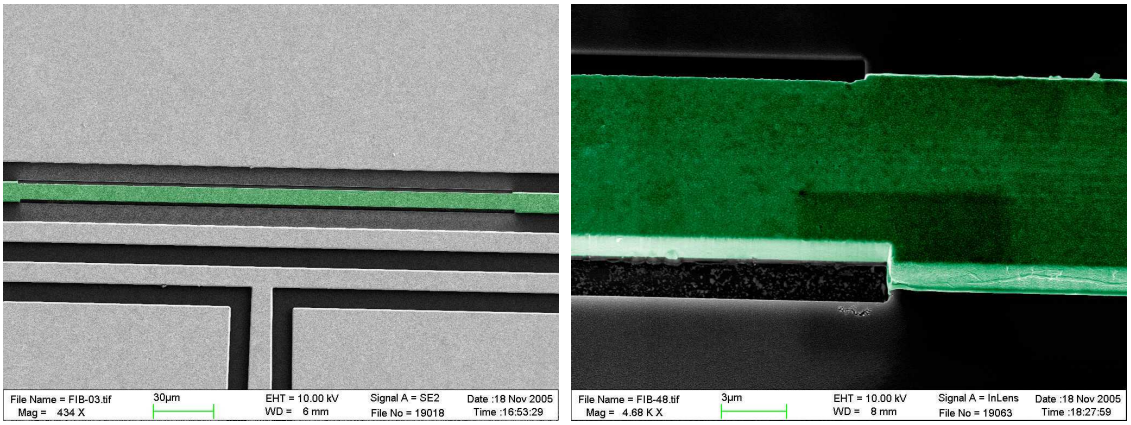

Figure 11.2: The polished wire: *left*, the whole area cleaned; *right*, a closeup of the steps created at the right end of the cuts.

We can see it in fig. 7.1 left, with the polished region marked by the blue ellipse. An electron microscopy of the FIBbed area is visible in fig. 11.2, with a closeup of the end of the $250\,\mu$m polished part in the image at the right. The purpose of this FIB is double:

- The steps at the end of the polished regions induce a change in the current densities; this gives rise to a modulation in the wire magnetic field that can be sampled using the atomic cloud as a magnetic microscope [123]. This modulation can be used to trap atoms with a higher longitudinal confinement than in a usual $\boldsymbol{Z}$ trap.

- A rough wire edge gives rise to current density modulations that cause fragmentation of the BEC, as observed in various experiments [104, 105, 106, 102, 13]. By polishing the wire we hope to reduce the disorder potential originated by the imperfections in the wire edges; a direct comparison can be done between this part of the wire and the untouched one (for our experimental results see chapter 11).

11.1.2 The notches

Instead of polishing, the FIB can be used to artificially deviate the current flow. On wires of thickness bigger than about $1\,\mu$m optical lithography can achieve structures of aspect ratios ($\rho \equiv$

height/width) below $\rho \simeq 1.5$; the thin ion beam of the FIB machine is not diffraction limited (limit in precision cutting are caused by different etch speeds, dependent on relative nanocrystal orientations), and can etch metals efficiently, so that $\rho = 30$ is possible.

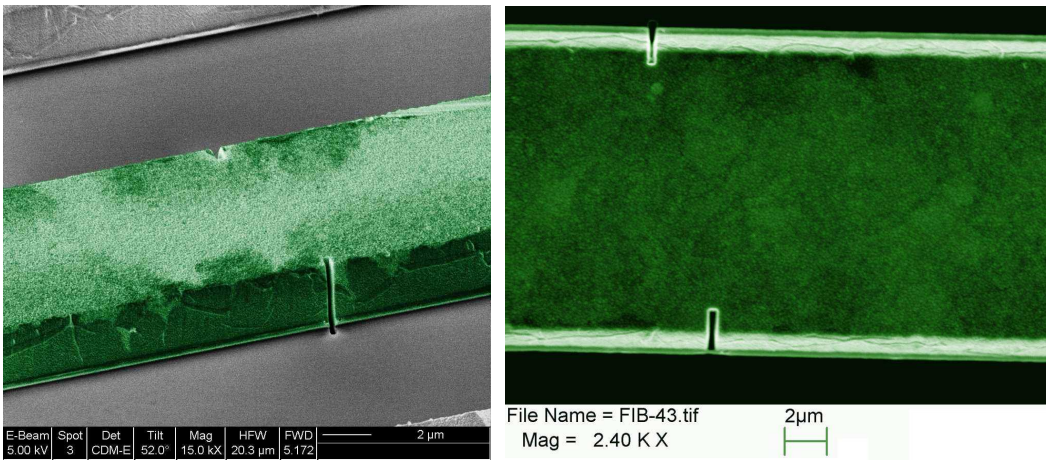

Figure 11.3: The notches

Two notches of about $900 \times 200\,\text{nm}$ ($\pm 15\,\%$)were cut in a $10\,\mu\text{m}$ wide $2.5\,\mu\text{m}$ thick wire. They are the basis for a double well or a barrier potential, as explained in 11.2.4. The cuts are visible in fig. 11.3, while their position on the chip is marked in red in fig. 7.1.

11.1.3 The tip

The electric field close to a charged surface grows with the curvature of the surface (the derivation of this relation can be found on any textbook on electrostatics) and is then higher close to sharp tips. Rubidium atoms, in presence of an electric field feel an attractive force, due to their electrical polarizability. The FIB assists us in creating microscopic sharp structures that can be employed to realize complex fields for the atoms.

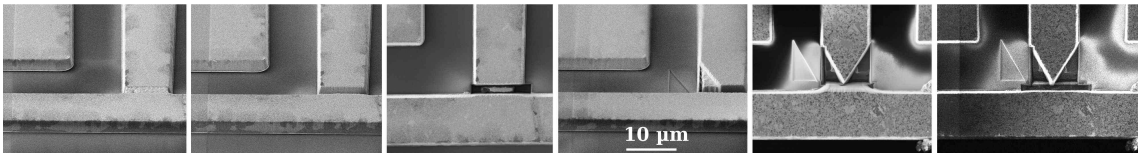

Figure 11.4: FIBbing the tip

To test these ideas we chose on the atomchip a $\boldsymbol{T}$ joint, made up of $10\,\mu\text{m}$ wide and $2.5\,\mu\text{m}$ thick conductors, and we etched the gold until we obtained a straight conductor and a sharp tip at about $1\,\mu\text{m}$ distance; the various steps of the procedure are shown in fig. 11.4.

Figure 11.5, left, is a side view of the tip and its surroundings. The sharpest edge of the tip has a radius of curvature around 150 nm (not far from the mean gold grain size, around 100 nm). The differently coloured conductors can be set to different electric potentials, and the blue one is the wire realizing the trap for the ultracold atoms. Although we proceeded carefully, the tip was destroyed, most probably already during bonding. The thin silicon dioxide insulation layer removed during the fibbing does not isolate the gold structures from the semiconducting silicon below them. As visible in fig. 11.5, right, short circuits melted part of the gold and the silicium in the substrate, compromising the tip functionality. Although we could not collect experimental

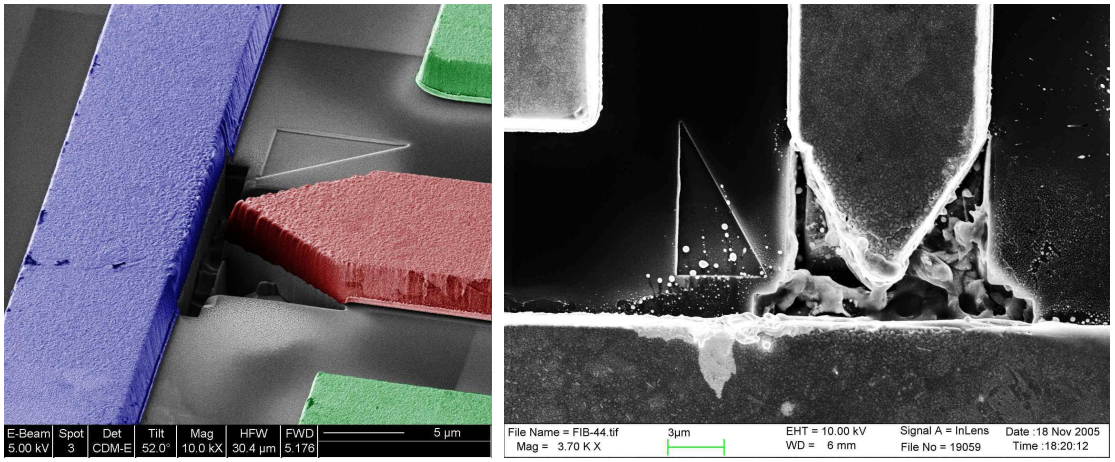

Figure 11.5: The tip: *left*, after realization, with electrically independent gold structures coloured differently; *right*, the melted tip and substrate after breakdown

data, it is however interesting to investigate the fields realizable with this tip; we present them in section 11.2.1.

11.2 Analysis of the FIBbed structures

11.2.1 E tip

It is well known from the *Maxwell equations* that the charge density σ on the surface of a conductor is higher where the radius of curvature r of the body is smaller (in first approximation $\sigma \propto r^{-1}$). As the electric field E on the surface is also proportional to σ, by realizing sharp structures we can then obtain high electric fields, localized around precise locations.

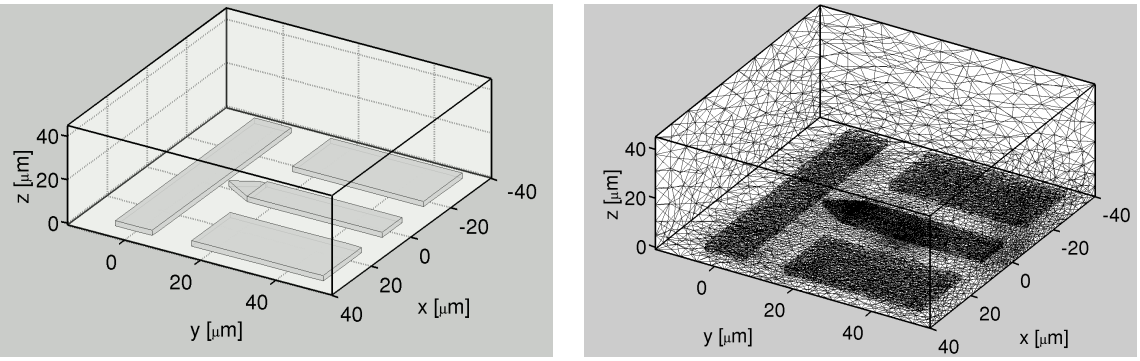

Figure 11.6: *Left*: the electric tip model, surrounded by the other conductors on the chip; the bigger box containing all the structures sets the boundary conditions for the potential ($V = 0$), as used in our simulations. *Right*: the mesh for the finite size element calculation, before the last refining; higher precision is guaranteed close to the conductors.

The tip, already described in sec. 11.1.3, is ideal for generating electric fields with modulations in the micrometer range. In fig. 11.6 we show the model used for the calculation of its electric field. The big box containing all the structures is used to give the correct boundary conditions, and its lower face corresponds to the chip substrate, connected to a pin set to $V = 0$. Three are the independent structures whose voltage can be set:

- The tip itself.
- The trapping wire, directly in front of the tip.
- The mirror on the chip, represented in the image by the two structures at the side of the tip; although no current flows in the mirror (covering almost the whole chip), its electric potential can be set with two pins.

In the next analysis we will consider the tension in the trapping wire and in the substrate to be the reference, at $V = 0$.

The simulation of the electric field around 3D structures is an intensive task for a desktop PC, and some expedients have to be taken in order to obtain fast and accurate results. We started by considering a small volume around the tip, and increased then it up to the point where the calculated field (in the region of interest) showed no dependence on the size of the boundary box. Validity checks with bigger volumes or finer spatial resolution can be done in 2D, by considering sections of the volume to be simulated.

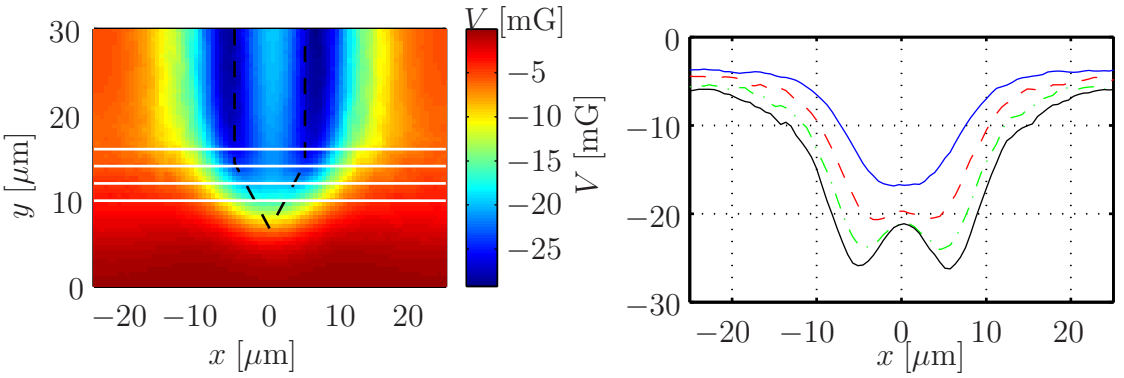

Figure 11.7: Potential due to the electric field, at $z = 7$ μm, tip set at $V_t = 1V$, mirror at $V_m = -0.7\,\mathrm{V}$. The origin of the y axis is at the center of the trapping wire, as clearly visible in fig, 11.6. *Left*: the 2D plot of the attractive potential; the tip geometry is outlined in black; white lines show the positions considered for the graph on the right. *Right*: cut showing the attractive potential at $y = [10,\ 12,\ 14,\ 16]$ μm, respectively in blue, red, green, black.

In fig. 11.7 left we see a 2D image of the potential[1] felt by the ^{87}Rb atoms, trapped at $z = 7$ μm. The dashed black line outlines the tip geometry. As the force the atoms feel in a static electric field is always attractive toward regions of higher field modulus, the minima of the potential follow the edges in the geometry (higher curvature). The potential in correspondence of the sharp tip looks blurred, due to the distance from the structure. Taking a section of the potential, at $y = [10,\ 12,\ 14,\ 16]$ μm, $z = 7$ μm we can move smoothly from a single well (fig. 11.7 right, blue curve), to a double well (black line); experimentally this is done by moving the magnetic trap position (changing B_z and B_y).

We can obtain similar results only working on electric potentials. Fig. 11.8 shows what happens when we move from $V_m = 0.5\,\mathrm{V}$ (single well) to $V_m = -0.83\,\mathrm{V}$ (double well); the low voltages applied are perfectly compatible with the atomchips[2] and easily controllable; due to the quadratic dependence of the modulating potential from E values much higher than what presented here are possible.

We were however not able to test this microdesigned potential, due to a short-circuit destroying the tip (see fig. 11.5), maybe already during the lengthy procedure of bonding the chip (sec. 7.3).

[1] The potential is given in Gauss, to ease the comparison with the magnetic potentials used for trapping.
[2] Atom manipulation in atomchips has already been shown with voltages of up to 100 V [124]

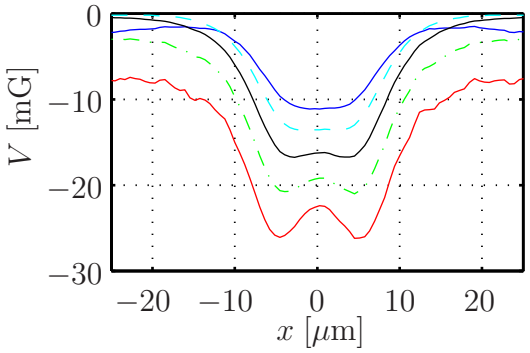

Figure 11.8: Potential modulation due to the tip, at $z = 7\,\mu$m, $y = 14\,\mu$m, $V_t = 1\,$V. Mirror structures set to $V_m = [0.5,\ 0.17,\ -0.17,\ -0.5,\ -0.83]$ V produce the potentials, respectively, of the blue (upper single well), cyan, black, green, red (lower double well) curves.

More complex structures can be thought of; by only allowing the two mirror structures to be electrically independent we could for example realize asymmetric double wells, as those envisaged in [125].

Dynamic potential modulation can be easily applied, with frequencies deep into the MHz range, well above the Larmor frequency. With a correct layout design even microwave signals can be taken on the chip, and create microscopic variable potentials. Such a subject requires however an own treatment and, apart from suggesting such developments, we will not go further into details.

11.2.2 B modulations

The conducting structures designed up to now on atomchips are generally assimilable to wires: the overall magnetic field $\boldsymbol{B}$ they realize depends only on how they are *bent*. If we want to know to a better degree $\boldsymbol{B}$ in the close vicinity of a current-carrying structure we usually assume the current density is constant across the wire section, and derive $\boldsymbol{B}$ using the *Ampére-Laplace/Biot-Savart* law.

But we have to understand that we should not limit ourselves to such a vision. What has been seen for the potentials due to electric fields can be repeated, mutatis mutanda, here.

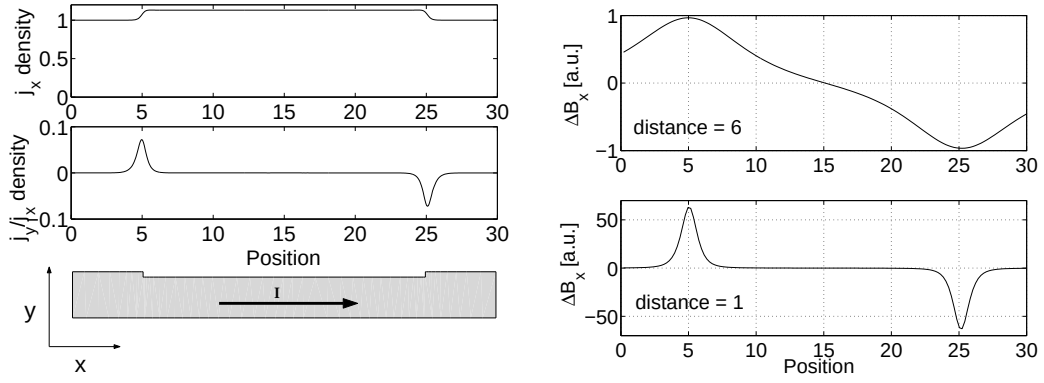

Figure 11.9: *Left*: Schematic model of the wire, with a 10% of it removed (bottom); current density components along x and y (top, center) are shown, measured along the center of the wire. *Right*: magnetic field modulation caused by j_y at two different heights z; fast decay of the amplitude and smoothing is evident.

We start by considering a simple trapping wire on which the current I flows, along x as usual. Let us now remove part of the conductor, from a border, for a certain length. In correspondence of the cut the current density j_x along x will increase, and we will have also a component j_y in the orthogonal direction, as schematically represented in fig. 11.9, left. The effect we are interested in is due to the current density j_y arising in correspondence of the edges of the cut: it will give rise to a magnetic field modulation ΔB_x oriented along x, the longitudinal trapping axis. This field modulation is directly mapped into a local modulation of the trapping potential, as B_x, at every position x along the trap axis, is rather constant and defines the trap bottom.

Apart from this effect, j_y and the local modulation on j_x will contribute also to variations of B_y and B_z, along the direction of strongest confinement for the atoms. But y and z are the directions of strongest confinement because the gradient $\nabla \boldsymbol{B}$ is bigger along y and z: what happens effectively is a slight transversal shift of the trap position, cancelling the modulation of B_y and B_z along the trap minimum.

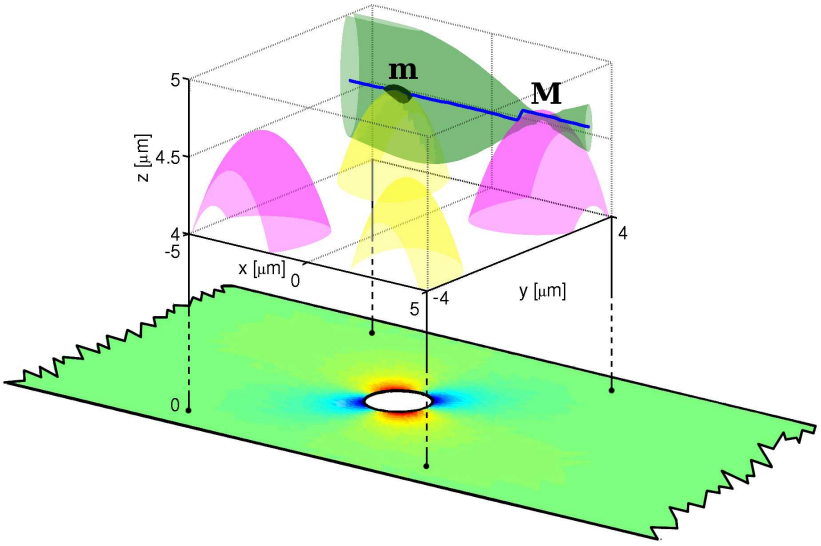

Figure 11.10: Current density modulation j_y due to a $\varnothing = 2\ \mu$m hole in the center of a $w = 10\ \mu$m broad wire (bottom), and fields above it.

The blue line is the trap center, that for every x is the point of minimum for $|\boldsymbol{B}|$; m and M are the positions in the trap where $|\boldsymbol{B}|$ assumes respectively its global minimum and maximum. The kink in the blue line in correspondence of M is given by the limited spatial resolution of the simulation, and it is of less than $100\,\mu$m.

Black and green surfaces represent regions of constant $|\boldsymbol{B}|$; they correspond to values it assumes in m and M , respectively $|\boldsymbol{B}(\mathrm{M})|$ and $|\boldsymbol{B}(\mathrm{m})|$.

Yellow and magenta surfaces are regions of constant B_x; they correspond to values it assumes in m and M , respectively $B_x(\mathrm{M})$ and $B_x(\mathrm{m})$.
Within a few percent we have $|\boldsymbol{B}(\mathrm{M})| - |\boldsymbol{B}(\mathrm{m})| = B_x(\mathrm{M}) - B_x(\mathrm{m})$. Along the whole trap axis we observe a modulation of B_x equal to that on $|\boldsymbol{B}|$. The current density modulation j_y is clearly antisymmetric in y, and so is the modulation on B_x: moving the trap from the represented position $y \simeq 3$ to $y \simeq -3$ (by inverting B_z) we are able to invert the lattice phase. z axis not to scale for better visibility.

We show that this is happening in fig. 11.10; here we analyze the magnetic field above a round hole in the center of a wire, similar to those of fig. 11.19. The minimum of $|\boldsymbol{B}|$ (B_m) is in correspondence of the small black surface ($\boldsymbol{m}$), and its maximum B_M at the bottleneck of the green one ($\boldsymbol{M}$). The trap position deviates only minimally from a straight line (of less than the

transversal potential ground state size $a_\perp$).

This observations are quite important for the simulations we are going to perform in the following, with particular relevance for the results of sec. 11.2.5. The magnetic field modulations are in fact only a minor perturbation (at least in the regions explored with the atoms). To know to a sufficient extent the trap we need to fulfill two requirements:

- Know the fields with a relative precision much bigger than the relative potential modulation. If the typical modulation of the trap minimum is around 1% of $|\boldsymbol{B}| = |B_x|$, then we have to calculate B_x, B_y, B_z with an error of about 0.1%.
- The spatial resolution Δr along any direction ($r = x, y, z$) has to be at least $\Delta r \ll |\Delta B| \,/\, |\partial_r \boldsymbol{B}|$, where we indicated the modulations introduced by the cuts in the wire with ΔB. We clearly need much finer spatial sampling along y and z.

The yellow and magenta surfaces on fig. 11.10 represent the regions where B_x takes the values it has, respectively, in $\boldsymbol{m}$ and $\boldsymbol{M}$. What we see is:

- The difference between these two values of B_x is equal to $B_M - B_m$.
- Along the whole trap minimum the modulation on B_x is equal to the modulation on $|\boldsymbol{B}|$.
- We make an error of only a few percent if we consider B_x along a straight line, where the trap would sit in case of a not sculptured wire.

We verified these observations with the different geometries proposed below and found that they are always valid. Therefore we will limit ourselves to calculating effects of the current-perturbing geometries only on B_x. In such a case the second of the aforementioned simulation requirements is much more relaxed (longitudinal trapping is weak), and the first one too: in fact we do not need to perform the vectorial calculation $|\boldsymbol{B}| = \sqrt{B_x^2 + B_y^2 + B_z^2}$, and we can equivalently consider the case with $B_x = 0$. This greatly simplifies the simulations.

Model cases

The cuttings we will analyze can be viewed as defects on an otherwise uniform structure. Among the simplest we consider here a round hole at the center of a conducting sheet, a step and a square cut at the edge of a semiinfinite sheet, as in fig. 11.11. Let us take as spatial directions x and y and a current density (far away from the perturbation) j_0 along x. The defects will perturb the normal current flow, generating the current density modulations j_x and j_y (along x and y).

The case of a round hole is analytically solvable and well known [126].For more general structures one needs numeric calculations.

However, if we restrict ourselves to the case of polygonal cuts in the edge of a conductor the *Schwarz-Christoffel* transformation can be used. This powerful technique allows to solve the *Laplace equation* in proximity of a boundary defined by linear segments, by a remapping to the solvable case of a flow in proximity of a uniform edge, a procedure known as *conformal mapping*. Details can be easily found in literature[127] and numerical solutions are also at hand[3].

The simplest defect that can be considered is a single step: it creates either a barrier or a trough, depending on the orientation of the dominating longitudinal field component and on the direction of the step. The notch can be seen as a *current dipole*, and above it there are both the barrier and the trough, at a short separation in x. The hole at the center of the wire generates a magnetic field configuration similar to this one, that can be inverted by moving in y, and that is exactly zero in x, along the center of the defect.

[3] http://www.math.udel.edu/~driscoll/SC/

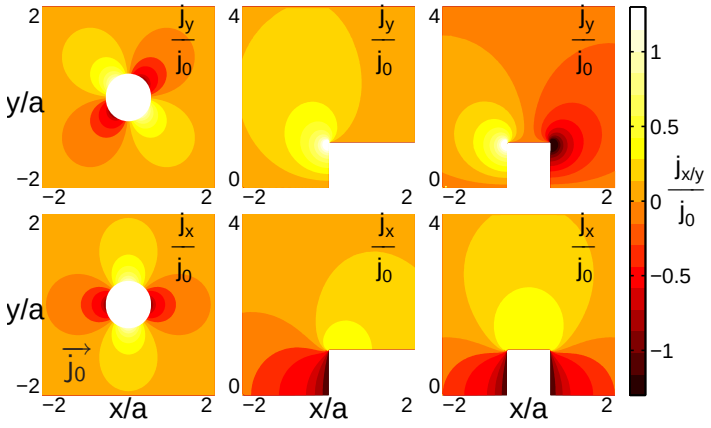

Figure 11.11: Any defect in a conducting sheet creates current modulations parallel (j_x) and perpendicular (j_y) to the unperturbed current flow (j_0), as shown in the picture above. *Left*: situation for a round hole ($\varnothing = a$) in a uniform conducting sheet. *Center, right*: a step and a square notch (size a) at the edge of a semi infinite sheet. In these last two cases maxima and minima of j_y have a singularity at the internal corners; at distances from the defects of the order of a current perturbations are already around 10% of j_0. Figures reproduce a region of interest around the defects.

The magnetic field of a general two dimensional current distribution can be evaluated in the Fourier domain. Following [128], the current densities' Fourier Transform components in x and y direction ($j_{x/y}$) are defined by:

$$\hat{j}_{x/y}(k_x, k_y) = \int_{-\infty}^{\infty} dx \int_{-\infty}^{\infty} dy\, j_{x/y}(x, y) e^{i(k_x x + k_y y)} \tag{11.1}$$

and the magnetic fields' Fourier transform:

$$\begin{aligned} \hat{B}_x &= f(k_x, k_y, z, d)\hat{j}_y(k_x, k_y) \\ \hat{B}_y &= -f(k_x, k_y, z, d)\hat{j}_x(k_x, k_y) \end{aligned} \tag{11.2}$$

where the filter f acts as a low pass filter for $j_{x/y}$; for homogeneous conductors, with $j_{x/y}$ independent of z

$$f(k_x, k_y, z, d) = \frac{\mu_0 d}{2} e^{-kz} \left(\frac{1 - e^{-kd}}{kd} \right) \tag{11.3}$$

where $k = \sqrt{k_x^2 + k_y^2}$ is the absolute value of the wave vector, z the distance to the top of the current carrying surface and d the thickness of the layer. At the surface of a thin conductor $f = \mu_0 d/2$.

Eq. 11.3 shows that the magnetic field computation can be effectively done by applying a low pass filter in Fourier space to the current distribution. This nicely illustrates the limits for potential design. In order to keep features up to a certain wave vector $k_{max} = \frac{2\pi}{\lambda_{min}}$ and to maximize their amplitude two requirements must be respectively met:

- In the limit of thin current layers $f(k_x, k_y, z, d)$ reduces to $f = \frac{\mu_0 d}{2} e^{-kz}$ and the structures of the current flow pattern are exponentially damped when receding from the wire. To achieve a modulation of a fraction η_0 of the maximum achievable field at a minimum structure size λ_{min} one has to stay at distances $z < -\log \eta_0 / k_{\max}$
- For finite thickness d, the contribution of current flowing deep below the surface of the sheet starts to drop off already inside the conductor. Increasing d leads to larger modulation until

this last saturates in the limit of a thick conductor. To reach a fraction η_1 of the maximum achievable modulation, one has to satisfy $d > \frac{-\log(1-\eta_1)}{k_{max}}$

11.2.3 Polishing wires

As a realization of the step in the wire edge we cut a $w = 10$ μm broad $d = 2.5$ μm thick wire for a length of $l = 250$ μm. An overview was already given in 11.1.1, where we also explained what we want to achieve. To sum it up shortly we expect to see maxima/minima in the trapping potential in correspondence of the steps at the end of the cut section. Then we hope to achieve a more uniform current flow in the wire and thus obtain a smoother trap.

In fig. 11.12 we have a zoom on the wire in correspondence of the end of a cut (top view). The contrast on the image has been enhanced to improve the visibility of defects in the wire edge. We can clearly see that the fibbed wire (left part of the picture) looks more uniform than the bare edge, on which filament-like structures arise; probably there is a deviation of the unpolished edge from a straight line of about $100-200$ nm, on length scales of the order of 1 μm, but from this perspective they are difficult to quantify, because the wire edge is not perpendicular to the observation point.

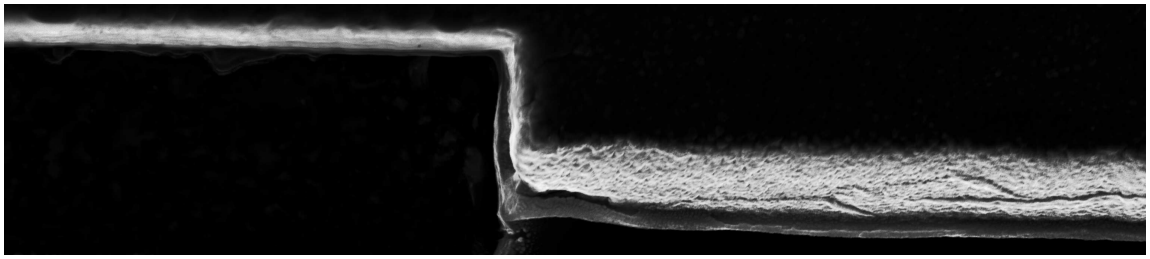

Figure 11.12: Step between the polished (left) and untreated (right) wire edge. Image is 9.5×2 μm is a detail of what reproduced in fig. 11.2, right.

If we transfer ultra cold thermal atoms to the area where the edge is modified by the FIB we observe as dominating potential features a trap [129] and a barrier at the step of the wire edge (see fig. 11.14 left, center). The longitudinal potential along the whole trap $V_{\|}(x)$ is recovered from the 1D atom density n_{1D} using Maxwell-Boltzmann statistics: n_{1D} falls exponentially with the value of $V_{\|}(x)$ above the trap minimum.

When cooling further, the higher atomic density in the deep potential dimple at one corner of the FIB modified area causes an enhancement of the condensate growth [130]. Care has to be taken that not all atoms accumulate there. Precisely controlling the final steps of the RF cooling process we can obtain a BEC in the dimple with atom numbers ranging from $4 \cdot 10^4$ to a few 100.

The longitudinal trapping frequency depends on the distance. For the set of experiments reported below we measured values in the range $40 < \nu_{\|} < 120$ Hz (see fig. 11.14 right, top). As the wire has been polished on both sides, and the two steps in correspondence of the cut end are not symmetric and present an offset of about 1μm in x (as visible in fig. 11.2) we expect a complex variation of the potential modulation with the position. From numerical simulation of the area we see that on the right cut we always have a potential minimum, with $\nu_{\|}$ dependent on y. The $\nu_{\|}$ values given above have been obtained from a harmonic fit of the measured longitudinal trapping potential in the dimple minimum; they agree with the expectations, given the relatively big error we have in determining the y position of the trap (at the moment the measurements were performed we still had to calibrate the positioning along y).

We can compare $\nu_{\perp}$ obtained above with those of the two biggest minima due to the fragmentating potential of the second chip (see chap. 7). Instead of deriving them from the observed longitudinal trapping potential, we excited the *breathing mode* (see sec. 3.5.1), by modulating the

trap bottom. Although the damping due to anharmonicities limits the observation to $3-4$ oscillations (as clear from fig. 11.13), we got for the two dimples $\nu_{\parallel,\,1} = [29.7,\ 20.1,\ 13.6]$ Hz and $\nu_{\parallel,\,2} = [38.7,\ 24.2,\ 16.6]$ Hz at heights of $z = [11,\ 28,\ 37]\,\mu$m and current density similar to those used previously. These data are important to see how big our microdesigned potentials are in comparison to the *noise floor* on the same potentials. We will discuss about this issue further on.

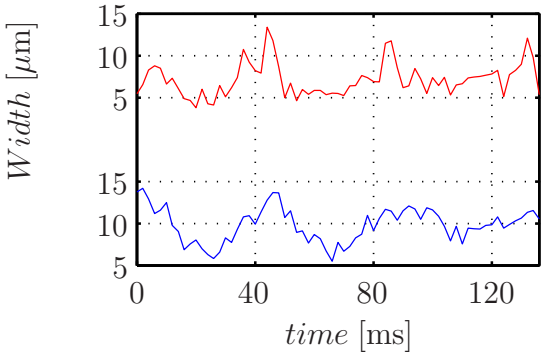

Figure 11.13: Longitudinal width of two BEC captured in minima of the fragmentating potential, exhibiting breathing mode oscillations. Anharmonicities cause fast damping, but behaviour is reproducible. Data taken at $z = 37\ \mu$m, $TOF = 6$ ms

Using different parameters we can obtain an extended 1D-BEC: we let current flow in a copper wire perpendicular to the trap, to generate a field gradient that shifts the trap minimum away from the dominating dimple, allowing to create a BEC that covers $600 - 800\ \mu$m.

The density of such a 1D-BEC is a very sensitive measure of the potential variations at the bottom of an elongated trap and allows to deduce the magnetic field variations along the wire [123, 131, 13]. We employ this measuring method to study the potential roughness and we use it to compare the polished section of the wire with the unpolished section.

Experiments were done with trapping currents ranging from $I = 20$ mA to $I = 60$ mA at an external bias field of 4.3 G, leading to atom-surface distances between $z = 6.4\,\mu$m to $z = 28.5\,\mu$m. Transversal confinement varied from $\nu_\perp = 6.6$ kHz to $\nu_\perp = 2.1$ kHz, longitudinal confinement was $0.5 < \nu_\parallel < 2.0$Hz and trap bottom of 0.86 G, or 1.2 MHz.. Using the modulation in the observed 1D atomic density we can reconstruct the potential modulation over the whole length of the 1D BEC. Over nearly the whole range of heights, the polished section of the wire gives a smoother potential, as characterized by the rms potential roughness.

For the lowest heights the full potential corrugation in the untouched region cannot be measured because it can be bigger than the chemical potential μ, and we exclude these data from further analysis. Comparing the standard deviation of the potential corrugations of polished section to the bare wire we find $\sigma_{\text{polished}}/\sigma_{\text{bare}} = 0.63 \pm 0.1$ The polished section gives nearly a factor two smoother potential, indicating a contribution of wire edge roughness [132] of the same order of that due to other causes. A plot of ρ in dependence of z is visible in fig. 11.14, right bottom. The two data points for $z < 8\ \mu$m correspond to the positions where the fragmentating potential is deeper than μ. The high value of the last sample at $z = 28.5\ \mu$m can be due to a higher percentage of thermal atoms in the unpolished region, that for such z is at the edge of the BEC cloud. However we did not reject this value in calculating ρ.

The potential corrugation in the bare wire was measured on a region as long as that used for the polished section; we choose the exact position by requiring the two areas to have the same average atom density: in this way we minimize errors due to imprecise calibration for the density. However, also by choosing different sections of the wire we obtain values of ρ compatible with the result given above.

These measurements have to be compared to previous observations of potential roughness.

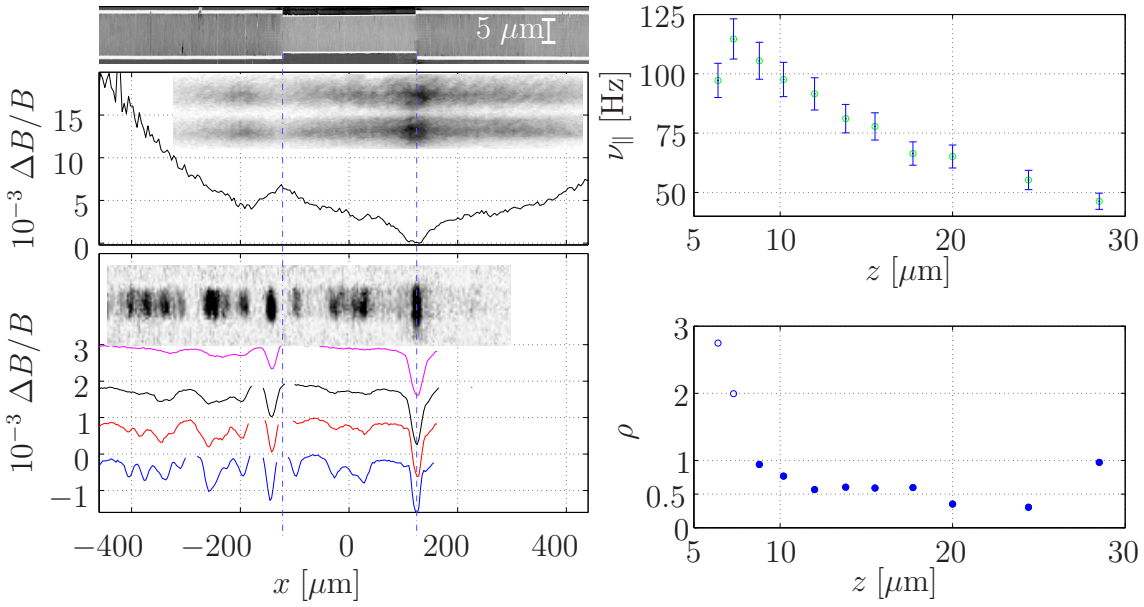

Figure 11.14: The measurements on the polished wire.
Left. Top: electron microscopy of the wire. Center: potential variation ΔB along x in units of the local wire field B at $z = 35\mu$m, measured with thermal atoms (in the insert an absorption picture, $TOF = 2$ ms). Bottom: potential roughness measured with a BEC at $z = [20,\ 16,\ 12,\ 8]\mu$m (curves from top to bottom); curves interrupted where roughness exceed the chemical potential μ and shifted for visibility. In the insert absorption image at $z = 9\mu$m . Data taken with $TOF = 1.8$ ms .
Right. Top: trap frequencies in the deep minimum at the end of the polished region. Bottom: Ratio ρ of the potential corrugation in the polished region and in the bare wire. Higher values for $z < 8$ μm are apparent, and due to roughness exceeding μ. For $z = 28.5$ μm a probably higher number of thermal atoms at the cloud edge smooths the density in the bare wire, increasing ρ .

Significant disorder in atom chip potentials has been reported at surface distances below $\sim 100\mu$m when using electroplated chip wires [133, 134, 135, 136]. The production process of such chips tends to generate columnar structures along the edges of the conductors, with roughness of about $1\,\mu$m. As clearly seen in [136, 132], this is the predominant cause for the disorder potentials in wires with a width of a few $10\,\mu$m.

Evaporated gold wires show on the contrary edge roughness on the scale of the gold nanocrystals (about 100 nm), without discernible columnar pattern. The disorder potential observed in our chips can be orders of magnitude smaller [13] and allows to create continuous 1D condensates for distances z down to a few μm. The chip used for this series of experiments shows a potential roughness more than a factor 10 smaller than observed in [133, 134, 135, 136, 137], but about a factor 10 larger than for the wires studied in [13]. Our experiments indicate that edge roughness can give a contribution to disorder potentials even for lithographically patterned evaporated gold wires [96] of the same order of magnitude of that due to other causes. To significantly decrease potential roughness the overall homogeneity of the conductor, determining the current flow also in the bulk of the wire, is the critical technological issue. We will explore in a forthcoming experiment this dependence. To fully exploit the possibility given by the potential modulations discussed below it is however clear that trapping potentials as smooth as those seen in [13] have to be used.

Before the bonding of the trapping wire broke we began a series of experiments to fully map the fragmentating potential in z and y. To that purpose we performed a calibration of the magnetic fields, as outlined in sec. 10.4. We then moved the trap position along y, at a fixed $z = 9$ μm by choosing the correct values of the fields B_y and B_z. In situ imaging shows that in the region

explored of $-2 < y < 6$ μm the z trap position deviates of less than 1 μm from the expected value (fig. 11.15). We do not expect to see significant variations in $V_{\|}$ by moving in y of less than z, because of the filtering of high spatial frequencies given by eqn. 11.3, and indeed the observed atomic density at first sight does not depend on y. However by careful inspection we notice that there is a shift of about 20 μm in the dimple at $x = -125$ μm; this is caused by the asymmetry of the steps at the end of the polished section. The bserved behaviour corresponds to what we obtain by modelling the current flow in the actual wire geometry.

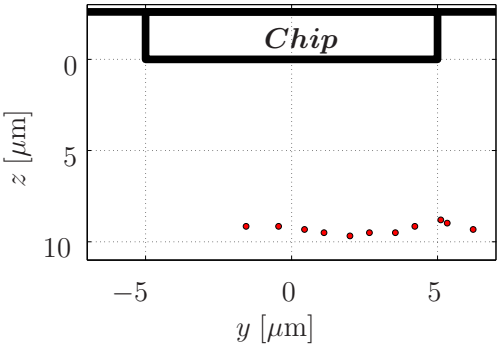

Figure 11.15: Scan of the trap position parallel to the chip wire (red points); y position of the data points calculated from knowledge of magnetic fields, z position measured with in situ imaging. Acquired data shown in fig. 11.15.

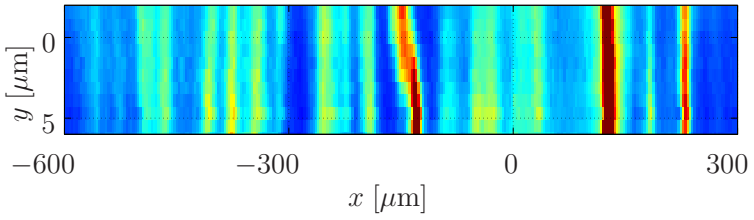

Figure 11.16: Atom density (a.u.) obtained by scanning the trap at $-2 < y < 6$ μm, $z = 9; \mu$m, as depicted in fig. 11.15. The polished area lies at $-125 < x < 125$ μm.

To further characterize the trapping wire we would like to close with a last experiment realized. We trapped atoms close to the wire ($z \simeq 6$ μm) and performed a TOF experiment, by switching off the chip current with a small delay in respect to the magnetic fields. The atoms experience then an acceleration (pushing them away from the chip) proportional to the local transversal field gradient. We know that when we move close to a wire, such that its width $w \simeq z$ the trapping frequency reaches a maximum, due to the wire finite size; at the limit of $z = 0$ the local field is ideally that seen close to an infinite, uniform conducting sheet. However, if originally we had $w = 10$ μm, the polished section has $w = 8$ μm, and the field gradient is higher. This is why in fig. 11.17 the atoms in the polished section move further away from the wire. In the following we give a few examples for potentials which can be created by FIB-sculpturing.

11.2.4 Double barrier

A short and deep cut generates a magnetic field perturbation with a maximum and a minimum along x; their mutual ordering can be inverted (for a given current flow and Ioffe field B_x orientation) by moving the cut to the other side of the wire. Combining two cuts on opposite sides, and shifting their position in x we realize a double-barrier potential, with a deep minimum in between, as that

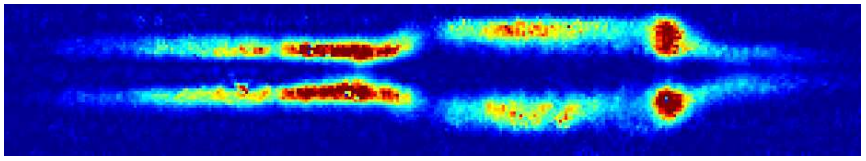

Figure 11.17: Atom density on the FIBbed wire, after $TOF = 2\,\mathrm{ms}$. The higher gradient in the polished region (center-left) accelerates to a greater extent the Rb cloud during the TOF; visible are also the dimples (maximum and minimum of $V_\parallel$) at the extremes of the polished edges. Image dimensions: 930×160 μm.

in fig. 11.18. As an example we realized two $0.9\,\mu$m deep, $0.15\,\mu$m wide cuts (insert of fig. 11.18 and sec. 11.1.2). For equal cuts, the double-barrier is symmetric in the wire center. Asymmetries can be introduced when moving off center.

For atom transport through such a structure resonances of the atom transmission are expected [129]; as they are separated by small energy differences (equivalent to few tens of nK) it may be challenging to observe them. In addition other non-linear effects can become dominant [138]. Inverting the relative position of the cuts changes the sign of the potential.

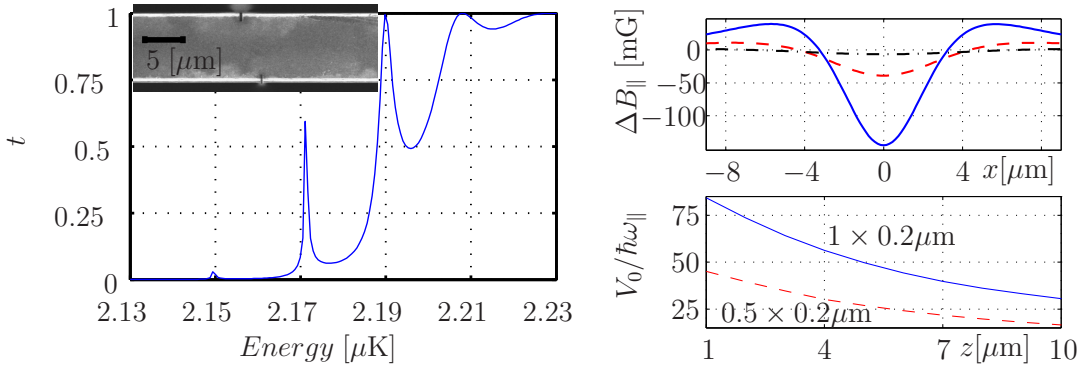

Figure 11.18: *Left*: Quantization of the transmission coefficient through the double barrier potential generated by the two notches shown in the insert (see also sec. 11.1.2), at $I = 100\,\mathrm{mA}$, $z = 5$ μm.
Right: simulations done on a $w = 10$ μm wide, $d = 0.50$ μm thick wire, with $I = 25$ mA. Top, potential perturbation $\Delta B_\parallel$ generated at $z = [2,\ 5,\ 10]$ μm (curves blue, red, black) by two 1×0.2 μm notches; bottom, depth of the potential in units of the longitudinal level spacing $\hbar\omega_\parallel$ obtained by making a harmonic approximation at the minimum. Data given for $1 < z < 10$ μm and two notches dimensions.

11.2.5 Periodic potentials

A regularly spaced set of cuts on the edge will generate a lattice. Similarly, an array of holes in the center of a plane conductor, as illustrated in fig.11.19, creates a modulation that is sinusoidal in first approximation. The array of holes in the center gives the additional advantage that the potential modulation is antisymmetric as a function of the direction transversal to the wire, y, and consequently can be inverted (or removed) without significantly changing other trap parameters. This is done by shifting the trap position transversely by about one lattice length.

The parameters we are going to use for the following considerations are:

- w the wire width.

- d the wire thickness.
- D the holes diameter.
- a the lattice step, or separation between holes.
- $E_r = \frac{\hbar^2 k^2}{2m_{Rb}}$ the energy associated with the lattice vector $k = \frac{2\pi}{a}$; in the lattice this is the most natural energy unit.
- V_0 the maximum potential modulation depth, due to the magnetic field modulation $\Delta B_{\|}$ along the trap direction x. It is dependent on y and z.

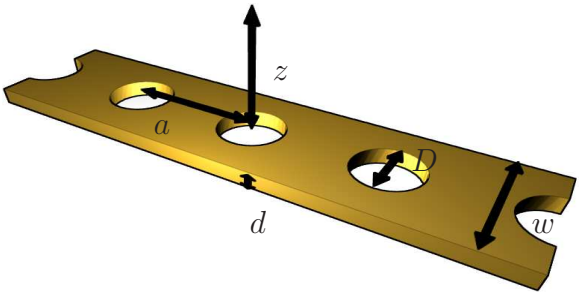

Figure 11.19: A wire section with holes for generating the lattice potential and its relevant parameters: w the wire width, d the wire thickness, D the holes diameter, a the lattice step, z the wire-trap distance.

We would like to know what kind of magnetic field modulation such a structure generates, for every possible choice of its parameters. More specifically we are interested in observing what happens to the atoms in a regime of strong interaction, with a sufficiently high transversal confinement: we are then limited to $2 \lesssim z \lesssim 15$ μm. It makes no sense to have $w > z$: we do not gain in trapping frequency and smaller wires can sustain higher current densities (due to better thermal dissipation, under the condition that electromigration is not relevant). We choose $w = 10$ μm.

We can then make some general observations on d and D. Due to the exponential decay predicted by eqn. 11.3 and to the wave vector $k = 2\pi/a$ it makes no sense to have a wire thicker than a, as the contribution given by the deeper wire layers drops off before reaching the trapping region. The simulated dependence of V_0 on d is shown in black, in fig. 11.21, left; it follows the theoretical expectations. For all the following analysis we will keep $d = 0.5a$.

The situation with D is somewhat more complicated, because we are not working with an infinite conducting sheet, thus the effects of the wire edges, for every choice of D, depend also on a. In general a dependence like that seen in the blue curve of fig. 11.21 is observed. The trend shows a saturation, because with larger holes less current flows in the area between them. A too big hole has also the effect of increasing the current density in the rest of the wire, so we will limit their diameters to $D = 0.6a$.

We are then left with the free parameter a; for each choice of a the field has to be calculated in x, y and z, so that we can get V_0. However the task of calculating with finite-size elements the field above a complex 3D structure (the holes number N_h has to be kept high) is still computationally intensive. What we did is summarized in fig. 11.20.

Essentially we created a 2D structure (the flow in the wire is parallel to the plane xy) and calculated the current flow around the central hole, whose boundary conditions guarantee values of j_x and j_y close to the ideal case (periodic array of holes): the part of the wire in correspondence of this central wire will be our *cornerstone* $\boldsymbol{C}$.

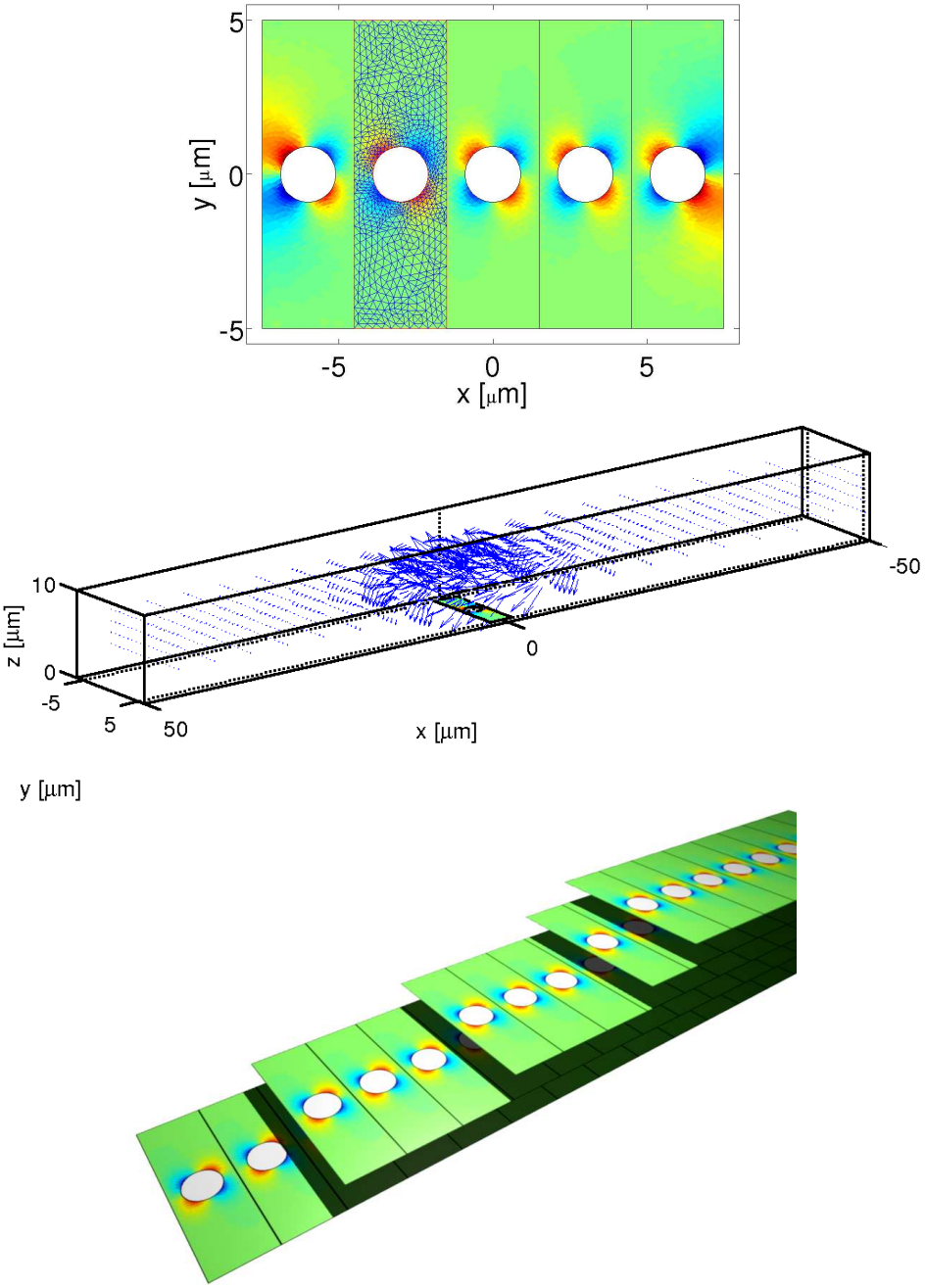

Figure 11.20: The steps for simulating the lattice field of a wire.
Top: A 2D structure with 5 holes is designed, the mesh for finite-size calculations is generated (in blue, around the second hole), and the current flow is calculated (shown is j_y, arb. scale). Due to its boundaries, the flow around the central hole does not differ much from what expected with an infinite hole sequence.
Center: The magnetic field ($\boldsymbol{B}$ or only B_x) of this central structure ***Str*** is found with the Biot-savart law; it has to be calculated with the necessary spatial resolution and for a long enough region in x .
Bottom: The field of a wire of thickness d and with N_h holes is calculated by vectorial sum of the shifted fields of a matrix of ***Str***. The current density in the actual wire is fixed (j_0); depending on the shift in z of the layers of holes their field is scaled, to keep consistence with the required j_0. With this technique we can simulate the effect of the wire thickness (finite-size elements calculation) on $\boldsymbol{B}$.

Then its magnetic field is derived with the Biot-Savart law; finally we generate the complete model wire by putting next to each other N_h copies of $\boldsymbol{C}$ (to create the lattice) and we build the wire thickness d with various layers of these periodic structures (fig. 11.20, left); to have accurate results their separation in z has to be much smaller than the wire-atoms separation; we also need to scale accordingly the current flowing in each sheet (to be consistent with the actual j_0). This procedure speeds up considerably calculations of $\boldsymbol{B}$, by restricting the computationally intensive Biot-Savart calculation to the flow of current in a simple 2D structure, and performing a vectorial sum of the results, shifted along x and z. Consistency and accuracy checks are performed then for specific choices of the running parameters, to verify the outcomes are correct. The periodic modulation of B_x has to be considered then in relation to the realizable trap configurations.

We have already said that B_x varies along x, the trap axis, sinusoidally; this is true to within a few percent for all the cases considered below, where $z > a$. This periodic field modulation generates a potential modulation for the trapped atoms. In the following we consider only the maximum depth of this potential, V_0.

The value V_0 depends on y. For $y = 0$ (exactly above the holes centers) the contributions of the left and right part of the hole cancel out, and $V_0 = 0$. More in general V_0 is antisymmetric in y, as can be seen in fig. 11.21, left. For every lattice length the maximum of V_0 is in correspondence of $y = \pm 0.4\, a$, and grows slowly with z, to $y = \pm 0.6\, a$ for $z = 2\, a$.

To assess if one can observe the transition between a 1D super fluid (SF) to Mott-insulator (MI) in such a magnetic lattice we follow the work by Zwerger [77]. For a 1D system of bosons ($\mu \ll \hbar\omega_\perp$) in a potential lattice the crossover from the SF to the MI regime happens at $\frac{U}{J}\big|_c = 3.84$ for an occupation of $\overline{n} = 1$ atoms per lattice site (J is the hopping amplitude, U the on site interaction). For $\overline{n} \gg 1$, $\frac{U}{J}\big|_c = 2.2\,\overline{n}$. In the case of a 1D BEC of ^{87}Rb one finds in the deep lattice limit ($V_0 \gg E_r$ with $E_r = \frac{\hbar^2 G^2}{2m_{Rb}}$, the energy associated with the lattice vector $G = \frac{2\pi}{a}$):

$$\begin{aligned} J &= \frac{4}{\sqrt{\pi}} E_r^{1/4} V_0^{3/4} \exp\left(-2\sqrt{V_0/E_r}\right) \\ U &= g_{1D} \int |\phi(x)|^4\, dx = 4\pi^{3/2} \cdot \frac{a_s}{a} \hbar\nu_\perp \left(V_0/E_r\right)^{1/4} \\ \frac{U}{J} &\simeq 3.8 \cdot \nu_\perp a \frac{\exp\left(2\sqrt{V_0/E_r}\right)}{\sqrt{V_0/E_r}} \end{aligned} \tag{11.4}$$

with a_s the scattering length, $\nu_\perp$ the trap frequency, a the lattice spacing, $\phi(x)$ the Gaussian ground state in the local oscillator potential. Unlike [77] the 1D nature of the trapping enters here the calculations through the 1D effective interaction strength g_{1D} (or $\nu_\perp$) in eqn. 11.4.

For $\nu_\perp = 20\,\text{kHz}$, $d = a/2$, $D = 0.6\, a$ and $2 < a < 5\,\mu\text{m}$ the SF-MI crossover can be achieved at $z \simeq 1.5\, a$ (fig. 11.22). The characteristic timescale for an experiment is given by the single particle tunnelling time; for $\overline{n} = 1$ it lies in the range of a few ms, about 2 orders of magnitude shorter than the expected lifetime at such z [107, 108, 109, 110, 111, 112, 113]. The limiting factor in an experiment would be detecting the low 1D atoms' density [4].

Increasing $\overline{n}$ up to 30 requires $\frac{U}{J}\big|_c = 66$ and the transition occurs around $V_0 \simeq 12\, E_r$ (fig. 11.22, upper dashed curve), with a single particle tunnelling time in the order of tens of ms, still about one order of magnitude shorter than the estimated lifetime and at a density experimentally observable.

The required value of V_0 at the transition can be lowered, for example increasing $\nu_\perp$. In this case the values for U and J used above (deep lattice) can be no longer valid.

In the limit of a weak lattice, raising the transverse confinement we move into the Tonks-Girardeau (TG) regime, increasing the ratio between interaction and kinetic energy per particle: $\gamma = mg/(\hbar^2 n_{1D})$, with $g = 2\hbar a_s \cdot 2\pi\nu_\perp$ and $n_{1D} = \bar{n}/a$ [77, 71]; in the analytically solvable case of

[4] Our detection sensitivity is $n_{1D} \simeq 1 \quad atom/\mu\text{m}$

one atom per lattice site, a finite excitation gap Δ is observable before the deep TG regime [77]. Keeping a minimum trap bottom at $1\,\mu$MHz to avoid spin flips, and $j_0 = 1 \cdot 10^{10}\mathrm{A/m}^2$, we can achieve $\gamma > 10$ for $z \leq 2\,a$; Δ is then of the same order of magnitude of V_0.

The above estimates are rather conservative. Our atom chips [96] can support at least 10 times larger current densities. This allows either thinner wires resulting in a 10 times longer spin flip lifetime, or much tighter confinement and reaching $\gamma \geq 10^4$ should be possible.

Increasing the γ factor while having at the same time $\bar{n} > 1$ can lead to novel and up to now unobserved phenomena [85, 86, 87, 88]: atoms in a MI phase can undergo a local TG-like transition in each lattice site and localize in spatially separated distributions.

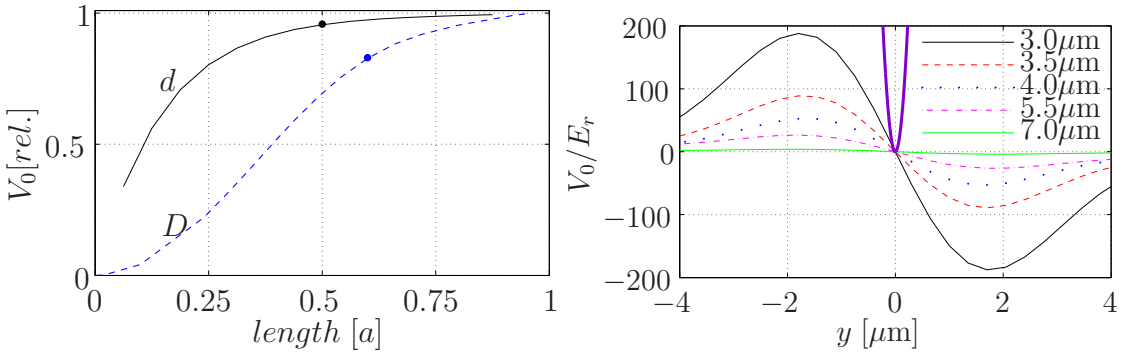

Figure 11.21: *Left*: Relative potential modulation amplitude for various d (in units of lattice length a, continuous curve) and for various D (dashed curve); the dot on the curves indicates the value used in the following simulations.
Right: Amplitude of the modulation on V_0 along the direction y transversal to the wire; the curves, from bigger to smaller in modulus, correspond to the heights $z = [3,\ 3.5,\ 4,\ 5.5,\ 7]\,\mu$m. Thick violet curve shows the trapping potential scaled down a factor 10 for comparison; the modulations are much smaller than the trapping even at small z/a. Apart from the scanned parameter, the others are: $j_0 = 1 \cdot 10^{10}\mathrm{A/m}^2$, $\nu_\perp = 20\,$kHz, $d = a/2$, $D = 0.6\,a$, $w = 10\,\mu$m $z = 6.75\,\mu$m; $a = [4,\ 3]\,\mu$m respectively for the left/right figure.

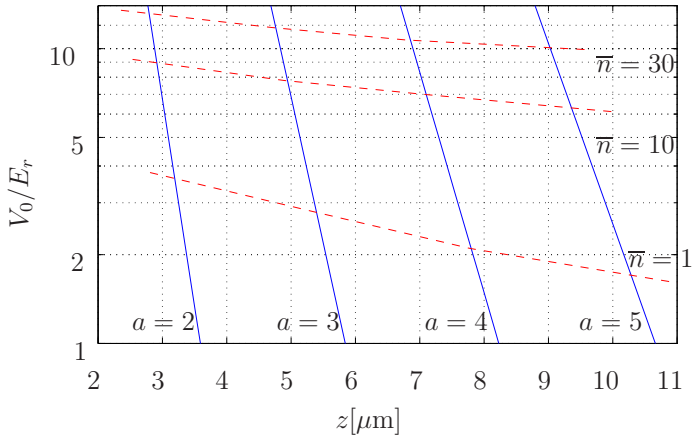

Figure 11.22: Potential modulation depth in lattice recoil energy units at $2 < z < 11\,\mu$m; continuous blue curves correspond to (left to right) $a = [2,\ 3,\ 4,\ 5]\,\mu$m; dashed red lines: critical value of V_0 for the Mott insulator transition, for (bottom to top) $\bar{n} = [1,\ 10,\ 30]$ atoms per lattice site. Simulations done at current density $j_0 = 1 \cdot 10^{10} A/m^2$, $\nu_\perp = 20\,$kHz, $d = a/2$, $D = 0.6a$, $w = 10\mu$m .

Chapter 12

Optical potentials

The microdesigned magnetic potentials studied in the previous chapter introduce a new set of possibilities for the coherent manipulation of matter waves on atomchips. To further expand the capabilities of the atomchip it is also interesting to explore the feasibility of integrating light fields close to its surface. Some results have already been obtained in another group [139, 140]: a couple of reflecting surfaces, glued on the atomchip, was used to integrate a light standing wave some hundred of μm above its surface; two short pulses were then shot in order to Bragg-scatter the trapped BEC. A theoretical explanation of the technique used has been outlined below.

We would like to see here if a standing wave is realizable in the close vicinity of the atomchip. In this way we hope to combine the light field to a magnetic trap with strong confinement $\nu_\perp$, possible only a few micromenters away from the trapping wires. We performed a series of measurements on our BEC apparatus to verify the feasibility of this idea and explore the experimental limits. Using laser light with a few nm detuning from the transition $\lambda = 780.24\,\mathrm{nm}$ we can reduce the spontaneous scattering probability to a level low enough to perform the desired experiments. The standing wave in which the BEC sits has a lattice length $a = \lambda/2$ about an order of magnitude shorter than the values explored in the previous chapter (sec. 11.2.5): this has huge effects on the conditions needed to reach the MI or TG phase transitions (i.e. in terms of tunneling lifetimes). Moreover the smaller value of a results in a factor 10 in the 1D atom density (for the same number of atoms/lattice site $\bar{n}$), enabling us to detect the TG gas ($\bar{n} = 1$).

The standing wave is obtained with two beams counterpropagating along the x direction and incident on the chip surface under a small angle α. The interference between the two incoming beams and the two produced by their reflection on the chip surface creates a standing wave along x, sinusoidally modulated in z with the periodicity $a_z = \lambda/(2\cos\alpha)$, as explained already in sec. 8.2.

12.1 An atomic beamsplitter

If we realize a standing wave and shine a short pulse of light on a BEC, the space varying potential $V(x,t) = V_0(t) \cdot \sin^2(k_0\,x)$ will not act for a sufficient long time to cause density modulations. Nonetheless it will imprint a sinusoidally modulated phase on the coherent matter wave. As phase gradients correspond to momentum components, we should expect the atoms to start moving; the periodicity of the modulation allows only precise momentum components: we have realized *Bragg scattering*.

In general different scattering orders are populated; with a careful shaping of the light pulse in time, $V_0(t)$, it is however possible to maximize the atom number in a precise order. The basic idea is to shine a short pulse, wait for the phase to develop, and then shine a second one. The idea has been presented and realized in [139, 140], and we will follow in short their derivation. We start by

writing the Schrödinger equation describing an atom in the light field:[1]

$$\mathrm{i}\dot{\psi}(x,t) = \left(-\frac{\hbar}{2m}\frac{\mathrm{d}^2}{\mathrm{d}x^2} + V_0(t)\cos(k_0\,x)\right)\,\psi(x,t) \tag{12.1}$$

k_0 is, as usual, the light wave vector $k_0 = 2\pi/\lambda$. As the amplitude varies generally in time, so does the potential $V_0(t)$. It is a good idea to expand ψ in the *Bloch basis*:

$$\psi(x,t) = \int dk \sum_n C_{2n}(k,t)\exp\left(\mathrm{i}(2nk_0 + k)x\right) \tag{12.2}$$

Then from eqn. 12.1 we have the set of equations (dependent on the integer index n):

$$\mathrm{i}\,\dot{C}_{2n}(k,t) = \frac{\hbar}{2m}(2nk_0 + k)^2 C_{2n}(k,t) + \frac{V_0(t)}{2}\left(C_{2n-2}(k,t) + C_{2n+2}(k,t)\right) \tag{12.3}$$

these equations describe how the various momentum orders evolve in time. We can consider the BEC to be at rest before the pulse, at $t = 0$, with a very narrow momentum distribution, so that $k \ll k_0$, and only C_0 is populated. The infinite set of eqn. 12.3 can be narrowed down to three ($n = -1,\ 0,\ +1$) if we limit ourselves to small potentials, in which case a negligible atom number is coupled to the orders with $n > 2$; this translates into the relation $V_0 \ll \frac{\hbar}{m}(2\cdot 2k_0)^2$.

After a unitary transformation on C_{2n} to cancel the kinetic energy associated with k, writing eqn. 12.1 in terms of the new quantities $C_+ = (C_2 + C_{-2})/\sqrt{2}$, $C_- = (C_2 - C_{-2})/\sqrt{2}$ and $\omega_r = E_r/\hbar$ returns:

$$\begin{cases} \mathrm{i}\,\dot{C}_0(k,t) = \dfrac{V_0(t)}{\sqrt{2}}C_+ & & & \\ \mathrm{i}\,\dot{C}_+(k,t) = 4\omega_r C_+ + \dfrac{V_0(t)}{\sqrt{2}}C_0 & + & 4\omega_r\dfrac{k}{k_0}C_- & \\ \mathrm{i}\,\dot{C}_-(k,t) = 4\omega_r C_- & + & 4\omega_r\dfrac{k}{k_0}C_+ & \end{cases} \tag{12.4}$$

as $k/k_0 \ll 1$ the mutual coupling between C_+ and C_- can be dropped ($C_- = 0$), and we are reconducted to a 2-level system. To transfer the atoms from C_0 to C_+ we shine a short pulse of duration T_1. This puts the system in $|C_0| = |C_+| = \sqrt{2}$. We let now the relative phase evolve in time for T_2, and then we transfer the atoms completely in C_+, with a second pulse of length T_1. An almost complete population inversion can be reached with the choices $T_1 = (2l+1)\pi/4\sqrt{2}\omega_r$, $T_2 = (2m+1)\pi/4\omega_r$ (with l, m integers), and with the optical potential during the pulses of amplitude $V_0 = 2\sqrt{2}\omega_r$. Other ratios of population unbalance can be obtained if the values are not correctly chosen. For ^{87}Rb at the $D2$ transition we have $\omega_r = 23.7\,\mathrm{kHz}$; fig. 12.1 shows the percentage of atoms in the $\pm 2\hbar k$ diffraction orders in dependence of T_1, T_2.

To test the standing wave we split the BEC in the $\pm 2\hbar k$ diffraction orders, by sending two light pulses of duration T_1, separated by a time T_2. The beam angle is $\alpha = 150 \pm 5\,\mathrm{mRad}$, giving $a_z = 2.6 \pm 0.1\,\mu\mathrm{m}$. We prepare the BEC at $100 < z < 130\,\mu\mathrm{m}$ in a trap of typically $\nu_\perp = 900\,\mathrm{Hz}$, $\nu_\parallel = 15\,\mathrm{Hz}$. The pulses are produced immediately after the release of the atoms from the trap. The relatively high value of $\nu_\parallel$ allows to have condensates with a length $l_\parallel$ below $100\,\mu\mathrm{m}$. The velocity of the atoms after scattering $v_{sc} = 11.8\,\mathrm{mm/s}$ enables to see fully resolved clouds after a $TOF = l_\parallel/v_{sc} \simeq 8.5\,\mathrm{ms}$. The alignment of the two beams is critical to obtain a good standing wave. At $z = 100\,\mu\mathrm{m}$ we need a precision in α of 0.3 mRad to have a maximum misalignment in the respective standing wave positions of $\Delta z = a_z/10$.

At the given $\nu_\perp$ the length of the ground state in the local oscillator is $l_\perp = 0.7\,\mu\mathrm{m}$; due to the mutual interaction between the atoms we can expect the BEC to be somewhat broader. Being $a_z \gg l_\perp$ not fulfilled we expect the atoms to see a modulation of the standing wave amplitude along

[1] We disregard in this treatment the mutual interaction between atoms. The approximation can be done because the kinetic energy acquired in the scattering is much bigger than the interaction energy. The atom interacting with the light field along the x axis can be described by a scalar field.

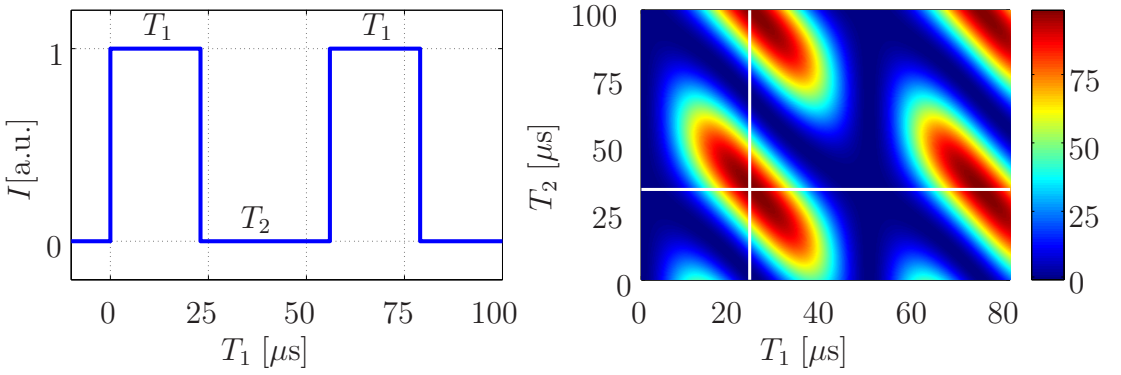

Figure 12.1: *Left*: schema of the two pulses used to transfer the atoms from C_0 to C_+. *Right*: percentage of atoms in the $\pm 2\hbar k$ diffraction orders (C_+), as a function of T_1 and T_2. White lines show the values scanned in experiment (fig. 12.3).

z. This gives the scattering patterns observed in fig. 12.2. If the BEC sits at the minimum of the standing wave most of the atoms are unaffected (left image, central cloud). The tails of the cloud however see the lattice and will be scattered; after a sufficient TOF the BEC expands transversally, and these parts of the cloud separate from the unscattered atoms, along the z direction (the four smaller clouds).

The opposite situation is visible in fig. 12.2, center. Here we moved the trap position so that it matches with the standing wave maximum. Obviously there are all the intermediate situations; by changing continuously the current in the trapping wire and observing the varying scattering pattern (right image) we are able to match the trap with the standing wave. The trap position is then determined by simulating the fields generated by the currents used. With this determination we find that the periodicity of the pattern has a step $a_{z,calc} = 2.73 \pm 0.05$, compatible with what expected from the above considerations.

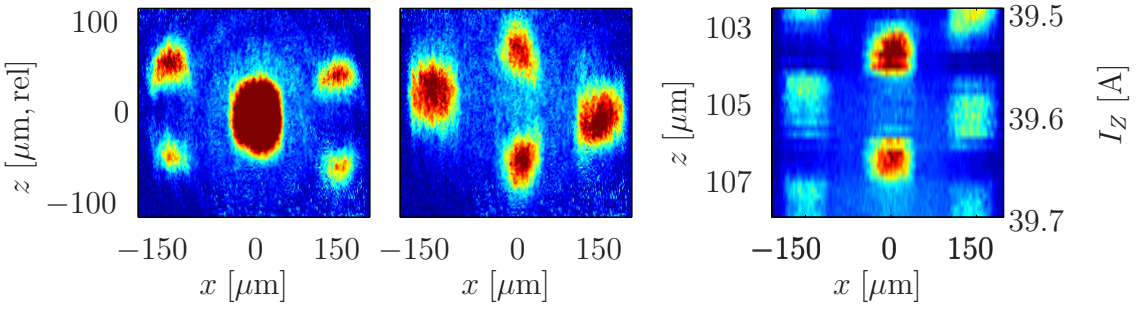

Figure 12.2: Moving the atoms across the standing wave: The trap alternatively sits in the minimum (left) or maximum (center, and get scattered) of the light intensity. The tails of the cloud see a complementary situation (scattered, left; unaffected, center). $TOF = 12\,\text{ms}$.
Right: If we consider only the atoms at the center of the expanded cloud (z direction) and change the wire trapping current between 39.7 A and 39.5 A we see a periodic behaviour (right); the value for z in the image (left axis) has been recovered by a simulation of the trap for the given currents.

Then we performed a series of experiment in which T_1 and T_2 were swept; in case coherence is preserved we expect a periodic dependence of the scattered fraction ρ_{sc} on those parameters: *Rabi oscillations*. In practice we used the parameters indicated by the white lines in fig. 12.1. The results obtained are depicted in figure 12.3. If we correct for a visibility smaller than 1 and exponentially decaying in time the measured ρ_{sc} follows quite closely the theoretical expectations.

The decay time, of the order of hundreds of μs, is 3.5 times shorter when we scan T_1 instead of T_2. This seems to suggest a loss of coherence due to the light field rather than to other factors (like for example noise of the trap). Interferometric measurements performed with the two 45° MOT beams show there is coupling of vibrations from the environment (even from normal talking) with oscillations frequencies in the kHz region. This may explain the relatively short coherence time. Experiments have been done with lower final RF evaporation frequencies, to rule out the influence of thermal atoms.

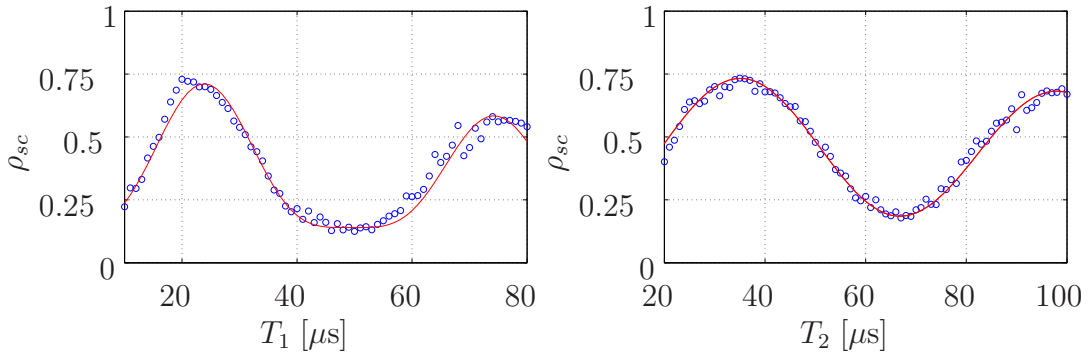

Figure 12.3: Rabi oscillations of the scattered atom fraction ρ_{sc} due to the scan of the scattering pulses duration T_1 (left) and separation T_2 (right). Red curves are calculated according to eqn. 12.4, and corrected for the reduced and time-decaying visibility.

If we want to address all the atoms in the trap with the optical lattice we can either compress strongly the cloud (to decreasetheir transversal extension) or increase a_z. Going down to $\alpha = 56 \pm 1\,\text{mRad}$ (the minimal angle before interfering with the horizontal MOT beam path) we got $a_z = 6.9 \pm 0.1\,\mu\text{m}$. In this situation atoms have been scattered across the whole trap extension, with less than 10% remaining in the zeroth scattering order (fig. 12.4). As the photon momentum is well known, so is the atom scattering velocity, $v_{sc} = 11.78\,\mu\text{m/ms}$. We can use this knowledge to calibrate the imaging system magnification M. Fitting the atom distributions to find their centers we get $v = 7.01 \pm 0.02\,\text{pixel/ms}$, the scale factor is $\Delta x_{sc} = 1.666 \pm 0.005\,\mu\text{m/pixel}$ and $M = 7.74$. This methods returns a result compatible with the previous gravity-based calibration (free-falling clouds), which gives $\Delta x_g = 1.70 \pm 0.03\,\mu\text{m/pixel}$, and shows a higher precision.

Coherence of the beam-splitting process has been tested also by repeating the scattering pulses after a time interval of $100\,\mu\text{s}$; in this case we observed a transfer of the BEC back to the $p = 0$ momentum state, as visible in figure 12.5.

The previous data was obtained with BECs just released from the magnetic trap. If the mutual interaction between atoms is low enough the scattering process should keep the same efficiency also with trapped atoms, and the clouds with the different momenta acquired should evolve in the trap, along x. For this purpose we prepare a BEC cloud with longitudinal extension of about $200\,\mu\text{m}$, as explained above, and then relax $\nu_{\|}$ to about 3 Hz, to allow the spatial separation of the scattered clouds. Although the scattering efficiency is not 100% (due also to unstable conditions of the trap parameters and of the BEC during the light pulses) we clearly see the atoms with momentum $p = \pm 2\hbar k$ evolving along x and joining the unscattered BEC after about 120 ms; as the trap confinement is non linear over the region explored (steeper potential far from the center) the oscillation half-time is somewhat shorter than the 167 ms expected from $\nu_{\|}$.

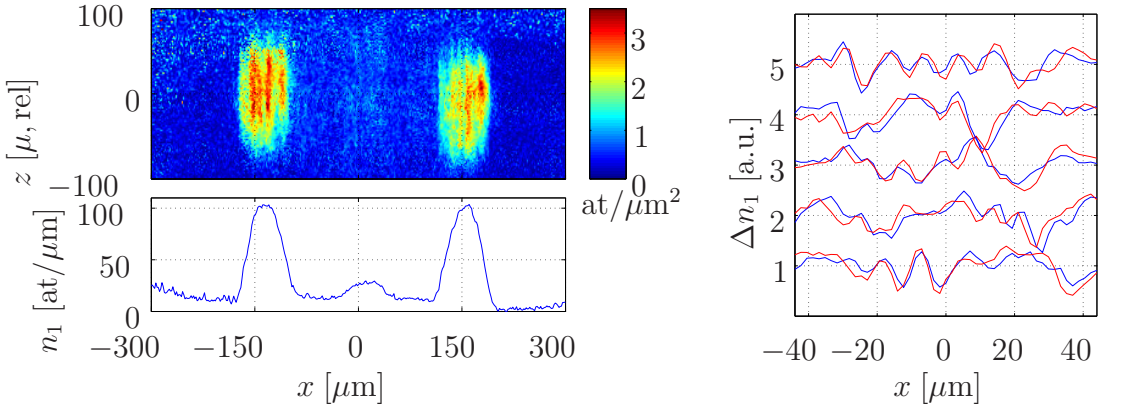

Figure 12.4: Scattering of atoms from a standing wave with $a_z = 6.9\,\mu$m. *Left*: the lower blue curve is the 1D atom density n_{1D}, averaged on four experimental realizations; the measure of the clouds position in x allows us to derive the velocity the atoms have (pixel/ms), and can be used to calibrate the imaging magnification. *Right*: 1D density modulation (fringes) on top of the TF profile for the two scattered clouds (red and blue curves). In the five experimental realizations plotted we can see an almost perfect overlap of the fringes caused by phase fluctuations in the trapped BEC, indicating the beamsplitter has the same influence on both clouds; a global phase difference may not be ruled out by this measure. Pictures taken with $TOF = 11.7\,$ms

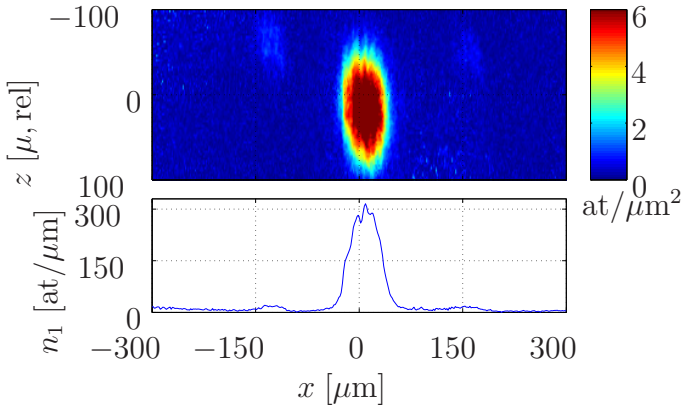

Figure 12.5: Repeating the double pulse (after $t = 100\,\mu$s) transfers almost all the atoms back to the $p = 0$ momentum state. This confirms the beamsplitter is coherent.

12.2 Deep potential lattices

The optical potentials used to coherently scatter the atoms can be employed to generate a steady, deep lattice. Trapping frequencies of up to $\nu_\perp = 20\,$kHz are possible with the wires on the chip, and at a potential depth of $V_0/E_r = 20$ we can achieve a Mott-insulator phase transition (see section 4.2) with $\overline{n} \simeq 20$ atoms per lattice site, meaning a density of $n_{1D} \simeq 60$atoms/μm easily observable with our imaging system. The selected potential depth, with 3 nm detuning, gives a lifetime of more than 0.5 s, much higher than the tunneling time $\tau_{tunnel} \simeq 60$ms.

We did some experiments with this and shallower lattices. The first step was searching for the standing wave position. By using high intensity and keeping the atoms for a sufficient amount of time in the lattice we observed heating. The position of the trap when heating is maximum is $z = (0.5 + n) \cdot a_z$, with $n = 0, 1, 2, ...$ In situ imaging and simulations of the trap configuration (given the currents used) correspond. Then a BEC was placed in the position where the lattice

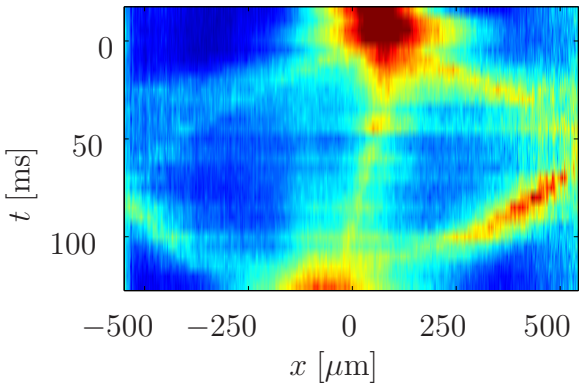

Figure 12.6: Evolution of a scattered atomic cloud inside the trap for 120 ms after the light pulses. The BEC (above, for $t < 0$) is split in three components ofmomentum $p = [-2, 0, 2] \cdot \hbar k$. Each cloud evolves along the trap axis ($0 < t < 120$ ms) and after 120 ms joins the others again, at $x \simeq -70\,\mu$m. The shift toward negative x values is caused by a mismatch between the initial cloud position and the actual trap center. Unbalance in scattered populations (left-right clouds) is partly an imaging artifact (see fig. 10.2), caused by oscillations in the z direction during the evolution. $\nu_\perp = 950$ Hz, $\nu_\parallel \simeq 3$ Hz, in situ imaging.

is located and the depth of this one was ramped up (slowly compared to the tunneling time); in case a MI transition is realized, removing the lattice slowly should restore the BEC. This can be recognized with TOF imaging, by observing the emergence of fringes (due to phase inhomogeneities in 1D condensates) or the expansion behaviour of BEC fragments. The observations were done with different lattice depths, in the following setups:

- The BEC was trapped in a $\nu_\perp = 8.5$ kHz trap, TOF pictures were taken; after a few ms the cloud is undetectable (low density, due to thermal expansion).
- The BEC was trapped in a $\nu_\perp = 8.5$kHz trap; after the lattice is ramped down the trap was relaxed in 2ms to $\nu_\perp = 80$Hz, to decrease the atom density (and thus the mutual interaction) but keep it at observable values.
- Same as the above points, but using at the beginning a weaker trap, $\nu_\perp = 1 - 3$kHz .

In all tests done we ended up with a thermal cloud. Tests without the standing wave show the atoms remain a BEC throughout the process. That was particularly clear when we trapped the BEC in a tight trap close to the chip and RF evaporated until a few distinct blobs remained in the minima of the fragmentating potential. By shifting the trap away from the surface (removing the disorder potential) these blobs moved to the trap center (along x), without showing appreciable broadening (caused by heating).

We think the heating observed is due to shaking of the lattice, mainly caused by mechanical vibrations of the chamber (as already observed above). Further studies are underway to pinpoint the exact cause of the problem.

In any case, to mechanically stabilize the lattice a different experimental setup is needed, with a shorter chip mounting and a stiff base for fixing the standing wave optics. In case, acoustic vibrations of small amplitude could be further reduced measuring the chip position (by means of laser interferometry) and actively driving the mirrors for the standing wave (with piezo actuators).

From the first results collected, the integration of light fields close to reflecting surfaces looks promising. Together with the technique described in the previous chapter it gives the atomchip much more flexibility for the coherent manipulation of quantum gases.

Part IV

APPENDICES

Appendix A

Constants and symbols used

The following tables, although not complete, list the constant and symbols most often used in this thesis.

Constant	Value	Description
ϵ_0	$8.854187817...10^{-12}\,\mathrm{Fm}^{-}1$	Vacuum permittivity (definition)
μ_0	$4\pi \cdot 10^{-7}\,\mathrm{N/A}^2$	Vacuum permeability (definition)
μ_B	$9.27400949(80) \cdot 10^{-24}\mathrm{J/T}$	Bohr Magneton

Constant	Value	Description
a_s	$5.237(1)\,nm$	^{87}Rb scattering length [141]
c	$2.99792458 \cdot 10^8\,\mathrm{m/s}$	Light speed in vacuum (definition)
e	$1.60217653(14) \cdot 10^{-19}\,\mathrm{C}$	Elementary charge
h	$6.6260693(11) \cdot 10^{-34}\mathrm{Js}$	Planck constant
$\hbar$	$1.05457168(18) \cdot 10^{-34}\mathrm{Js}$	Planck constant/2π
I_s	$42.503(3)\,\mathrm{mW/cm}^2$	Saturation intensity (D2 line, π polarization)
k_B	$1.3806505(24) \cdot 10^{-23}\,\mathrm{J/K}$	Boltzmann constant
m_u	$1.66053886(28) \cdot 10^{-27}\mathrm{kg}$	Atomic mass constant
m_e	$9.1093826(16) \cdot 10^{-31}\,\mathrm{kg}$	Electron mass

Symbol	Description
μ	Chemical potential
ν_w	Osc. freq. around the local lattice minimum
ν_x, ν_y, ν_z	Trap frequency along x, y, z
$\nu_\parallel$	Trap frequency along x
$\nu_\perp$	Trap frequency along y, z, in the case $\nu_y = \nu_z$
ω_i	Trap angular frequencies along direction i , with $i = [x, y, z, \parallel, \perp]$

Symbol	Description
a_s	Scattering length
a_w	Ground state size in the local lattice minimum
B_x, B_y, B_z	Magnetic field component along x, y, z
d_0	Mean interatomic distance $d_0 \simeq \sqrt[3]{a_s}$
$E_r = \frac{\hbar^2 k^2}{2m_{Rb}}$	Lattice recoil energy, in a lattice of wavevector k
FD	Fermi-Dirac
g	Interaction potential between atoms
g_{1D}	Effective 1D interaction potential
g_p	Gas parameter $g_s = na_s^3$
j_0	Current density in the chip wires
$j_{x/y}$	Current density modulation along x/y in the chip wires, due to the FIB cuts.
J	Hopping energy for bosons in an optical lattice
K	Kinetic energy per particle
k k_x	Lattice wave vector
$l_\perp$, $l_\parallel$	Harmonic oscillator ground size, along y, z or x.
MI	Mott insulator
MOT	Magneto optical trap
n	Atoms density
N	Atoms number
n_0	Density/number of atoms in the ground state (condensate)
n_{1D}	1D density along the trap axis
$\overline{n}$	Number of atoms in each lattice minimum
r_g	Characteristic interaction length in 1D
r_{MI}	Ratio U/J
T_C	Critical (condensation) temperature
T_D	Degeneracy temperature
TF	Thomas-Fermi
TG	Tonks-Girardeau
TOF	Time of flight: time between BEC release from the trap and imaging
T_ϕ	Phase coherence temperature
U	Interaction energy per particle
V_0	Potential modulation depth
x	Direction along the trap axis
y	Direction transversal to the trap, parallel to chip
z	Direction perpendicular to the chip surface

Appendix B

Rb 87 D line data

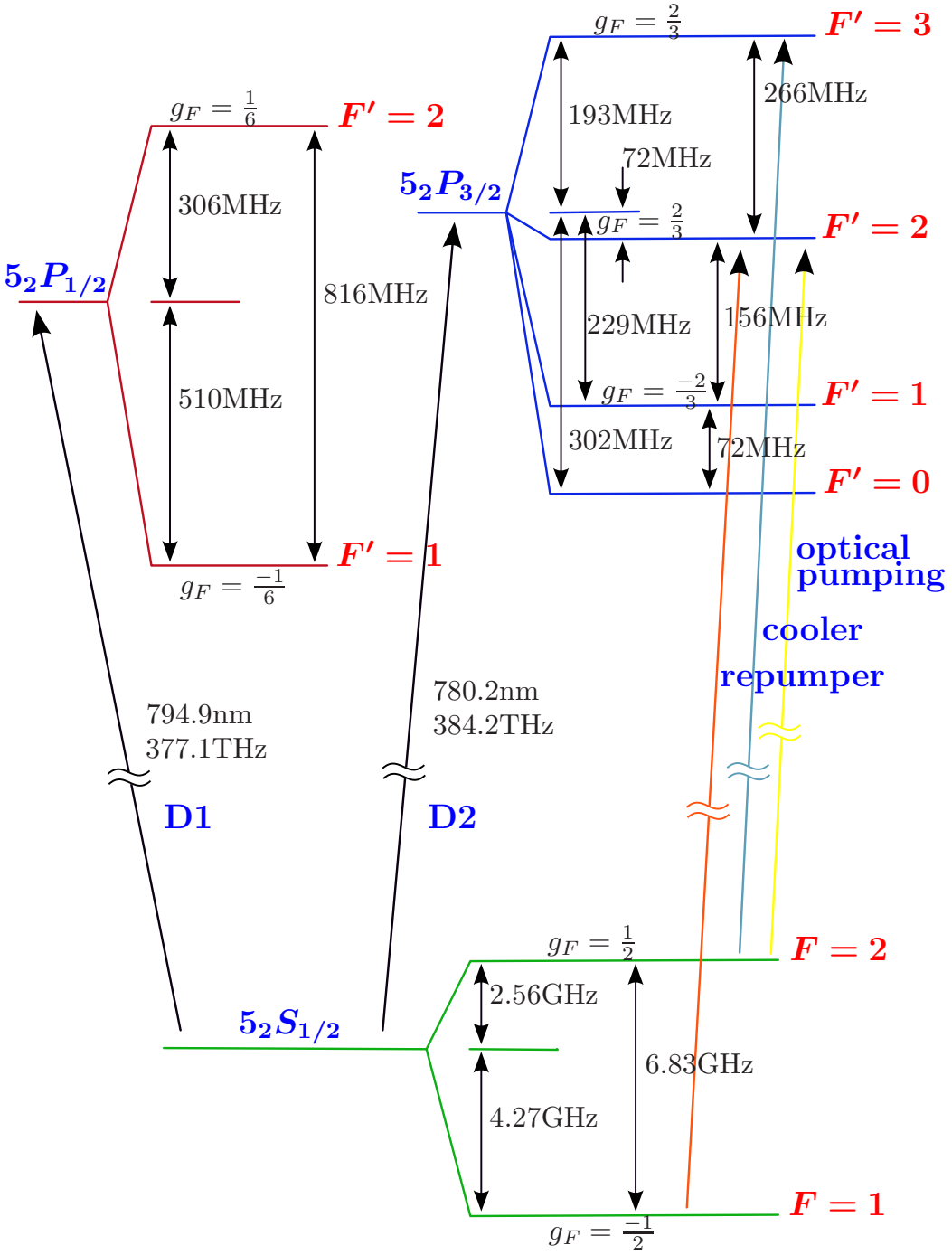

Figure B.1: ^{87}Rb D1 and D2 line data [142], and laser transitions used in the experiment.

Appendix C

Bec block scheme

The software driving the experiment can be reconducted to two main blocks. A first one, for a total of about 8000 lines of code, is composed mainly by matlab scripts to control the user interface; its operating schema is shown in fig. C.1. The second block (for other 7000 lines) is written in ADBASIC[1]

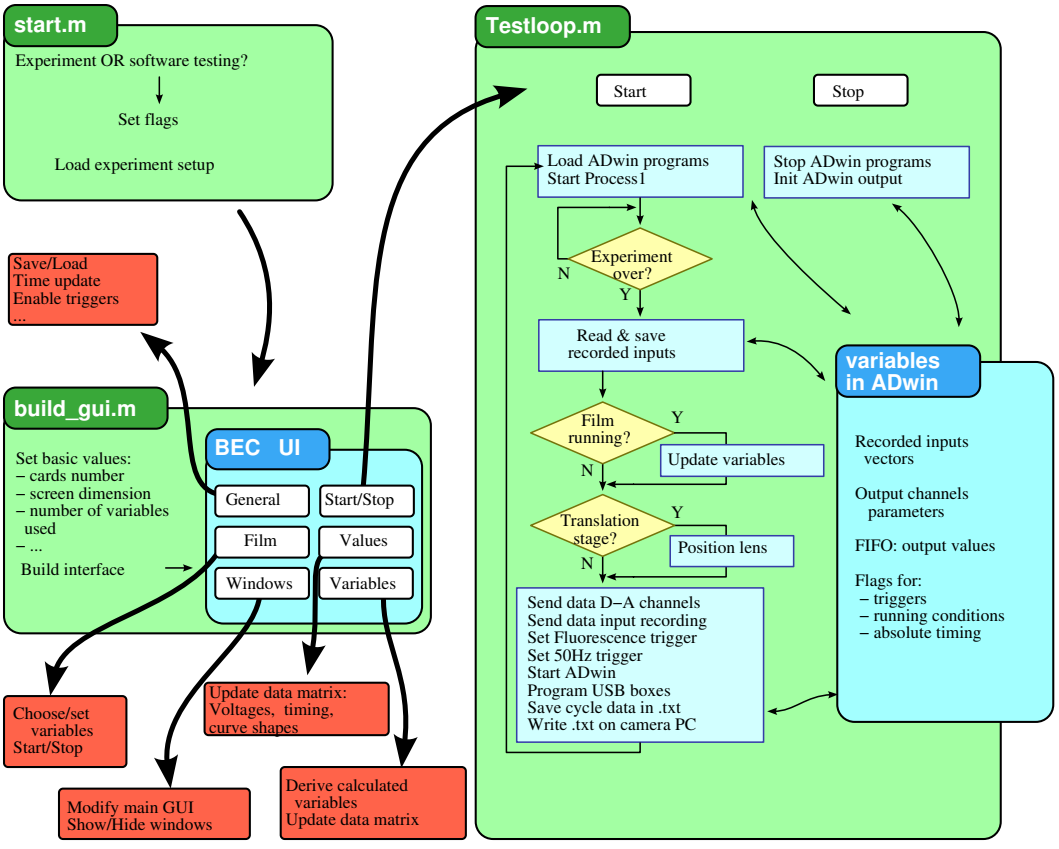

Figure C.1: Schema of the software realizing the man-experiment interface. **1**: The script start.m sets the flags deciding whether we are in the lab or in a test machine; in this second case the ADwin IO PC is simulated. Then a prompt allows to choose one of the saved experiment sessions. **2**: build_gui.m creates the interface (GUI) from here onward the control goes to the GUI. **3**: testloop.m controls ADwin, by checking its status and writing/reading its variables and registers. **4**: Various other scripts respond to GUI callbacks, updating the experiment parameters (red boxes).

[1] A BASIC variant developed by company Jäger

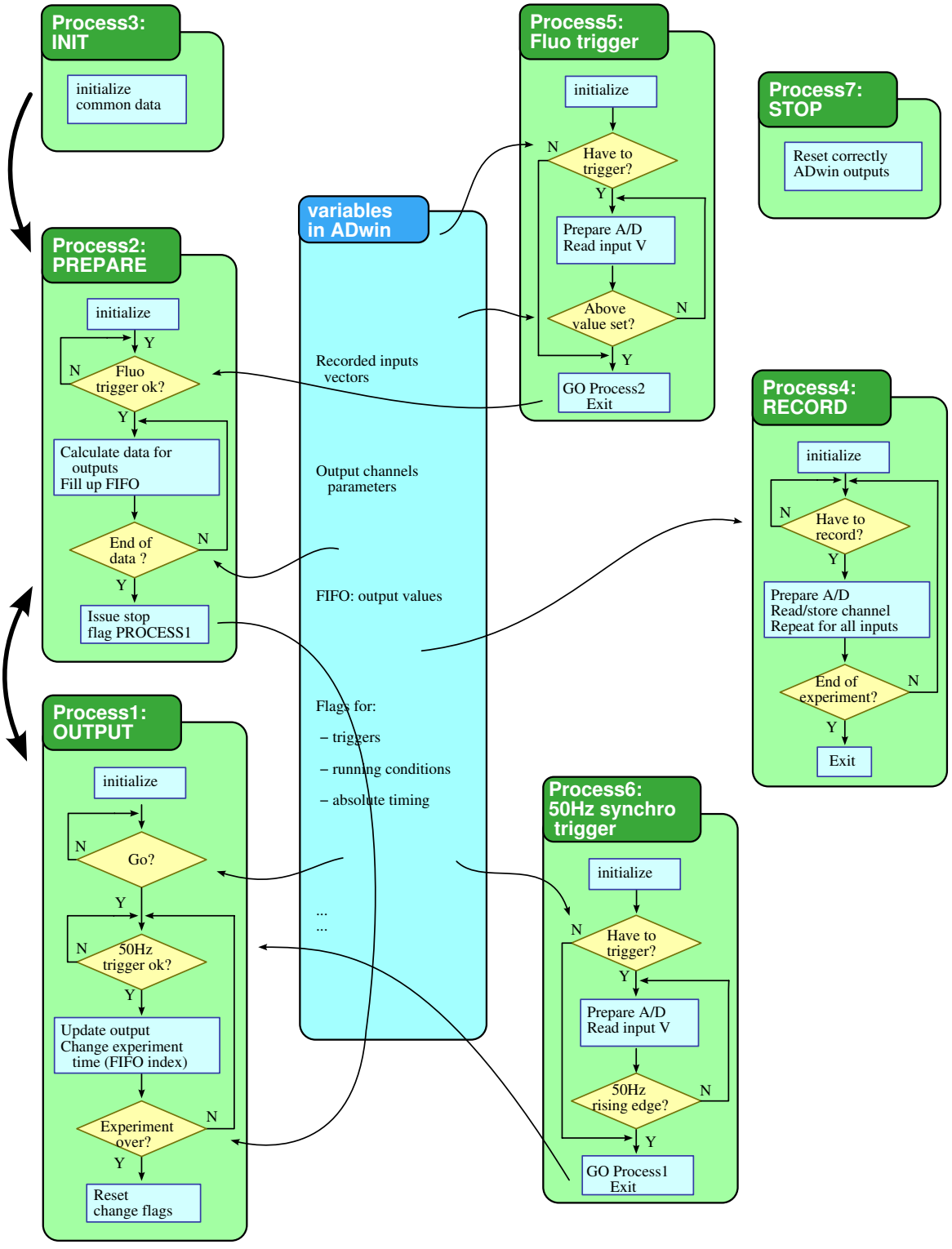

Figure C.2: ADwin software. Various processes run concurrently, their number specifies the priority they have. **Process1** is the most important; it updates the outputs to control the experiment with the requested clock (usually $\tau = 12.5\,\mu s$); in the CPU spare time **Process2** calculates and fills in the FIFO with the data needed by the outputs; these two programs represent the core of the experiment control

Below we reproduce images of the single windows that build up the GUI. For explanations check chapter 9.

Figure C.3: Variables and calculated variables used in the experiment.

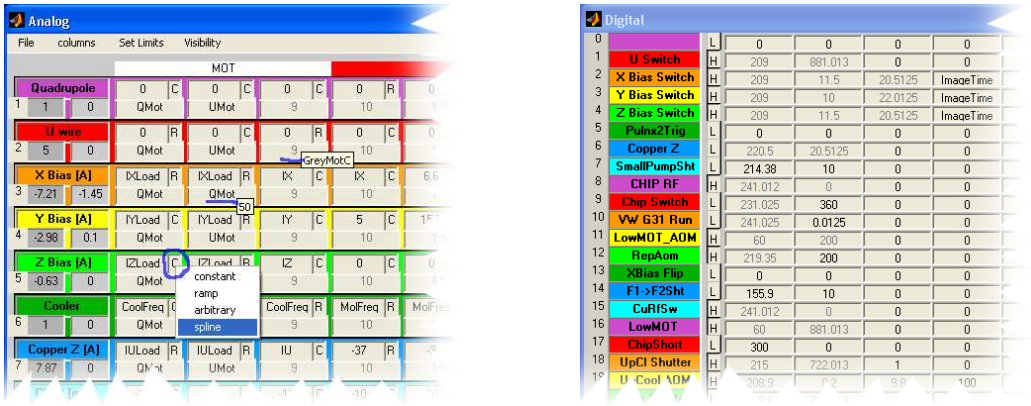

Figure C.4: Analog and digital signals. Digital channel n.22 is normally used to define the moment where the 50 Hz synchronization has to happen; the channel number can be changed (as may other general variables) in build_gui.m .

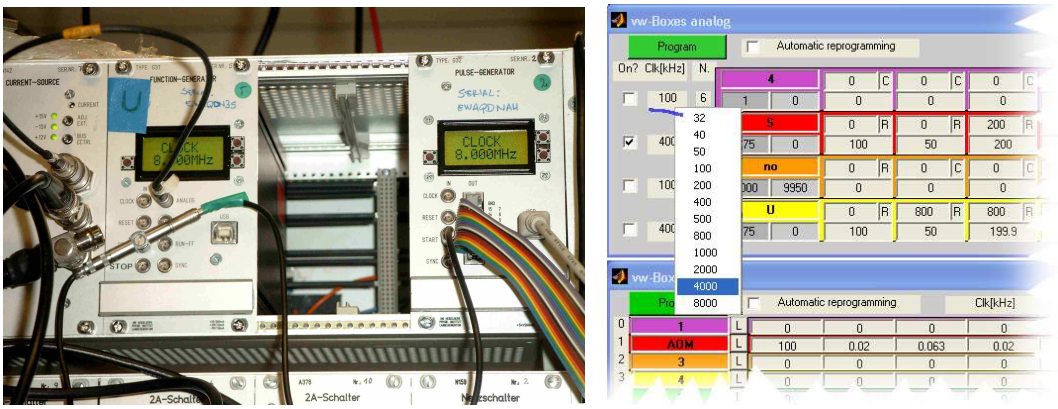

Figure C.5: The USB modules (left) and their programming interfaces

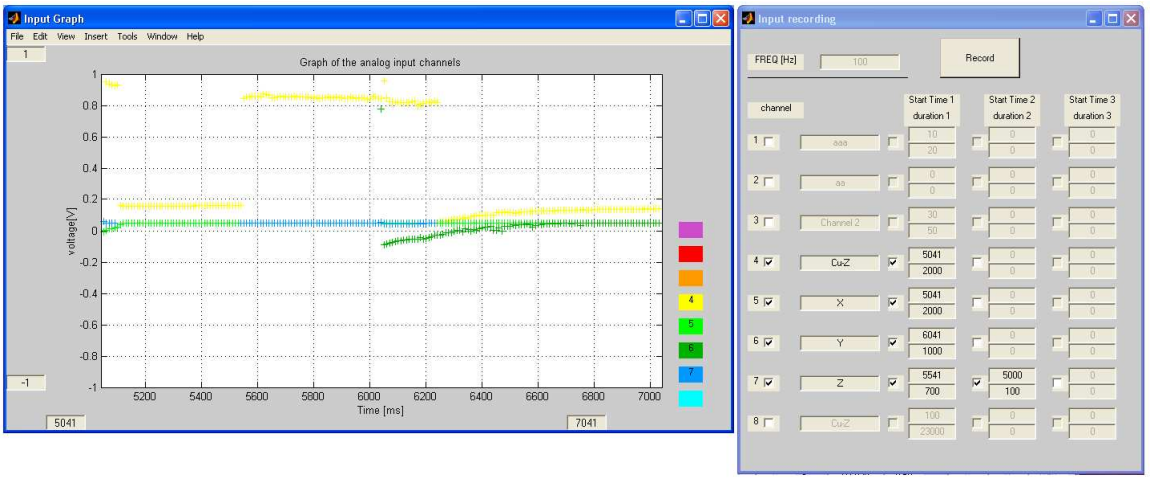

Figure C.6: Input Control; for every input channel up to three distinct periods in which data is read in can be defined. Clock time changing is disabled, but can be varied in the m-files (complex_input_recording.m and related). Data read-in in the previous cycle can be plotted.

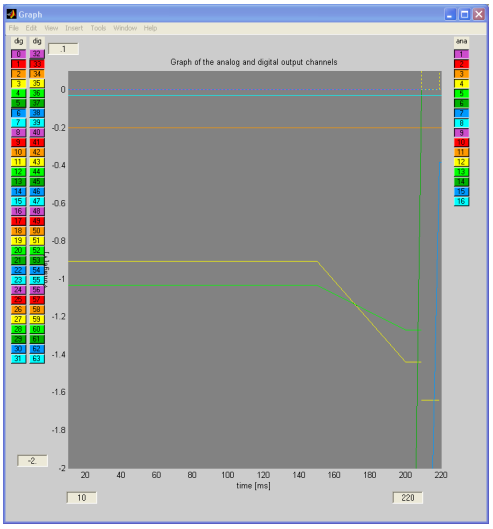

Figure C.7: Signals overview; zooming and signal selection enables fast checking of chosen transitions.

Appendix D

Feedback schematics

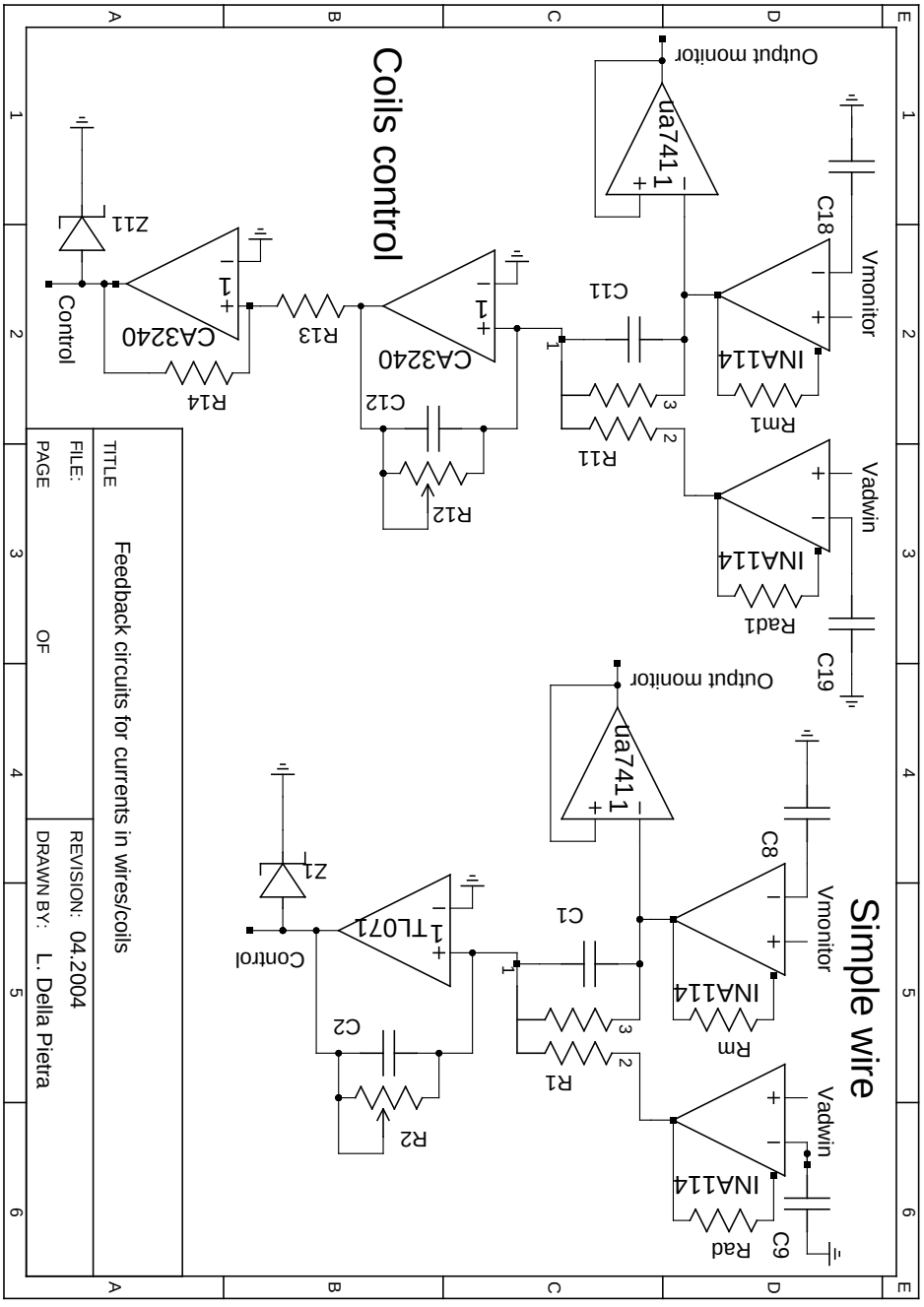

Rad	Rm	R1	R2	C1	C2	Z1	C8	C9
250kΩ	2.6kΩ	4.7kΩ	2MΩ	35nF	44nF	3.6 V	100nF	100nF

Rad1	Rm1	R11	R12	R13	R14	C11	C12	Z11	C18	C19
250kΩ	6.5kΩ	4.7kΩ	2MΩ	4.7kΩ	42kΩ	.47μF	100nF	5.1 V	100nF	100nF

Figure D.1: Feedback schematics and elements values

Appendix E

Chip holder and copper structures schematics

Next schematics show the upper structures of the mounting, modified from the previous version to accommodate the second chip (see also fig. 6.14): the ceramic holder and the two independent copper conductors.

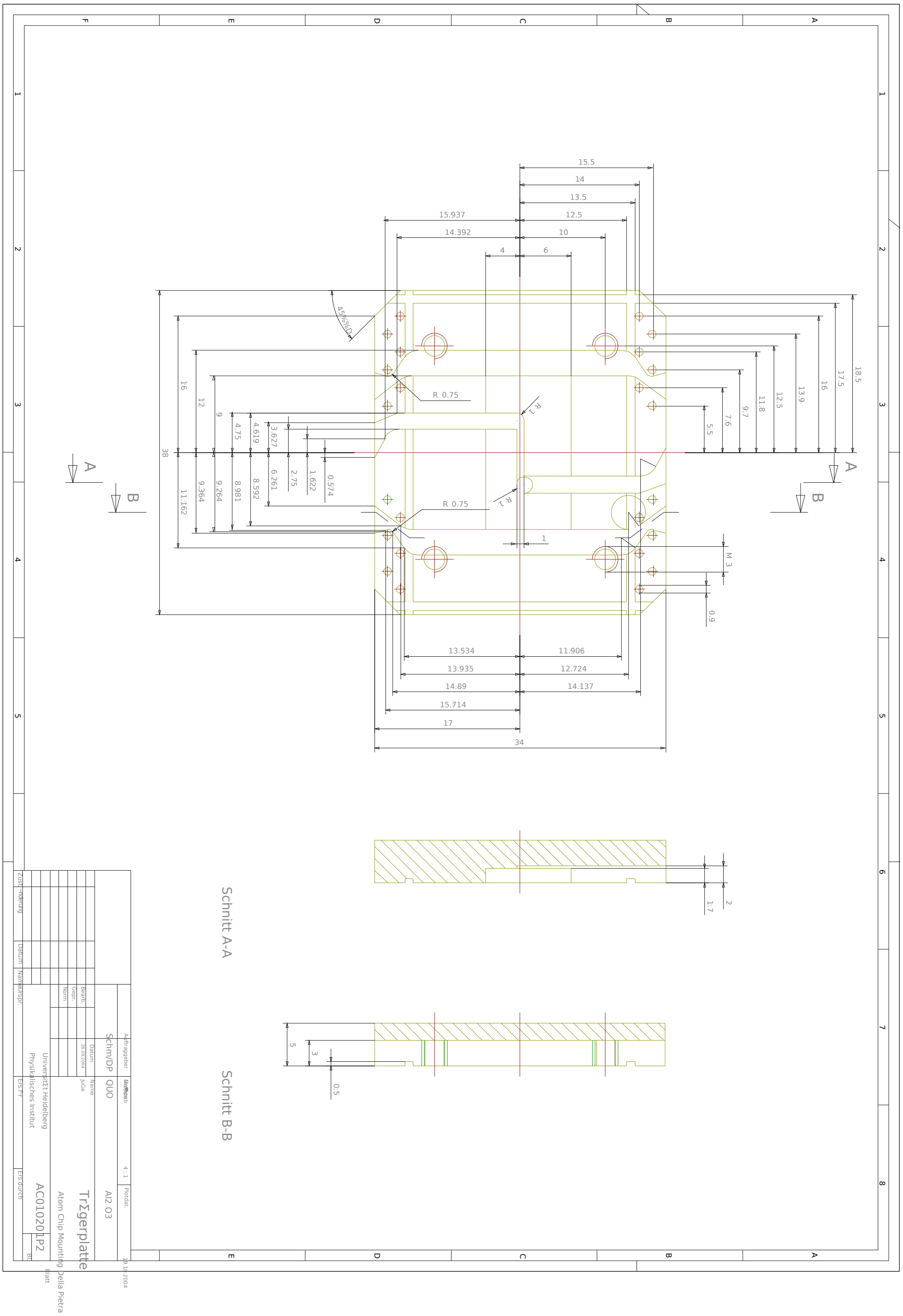
Schnitt A-A
Schnitt B-B
Atom Chip Mounting
Della Pietra
AC010201P2
Al2 O3

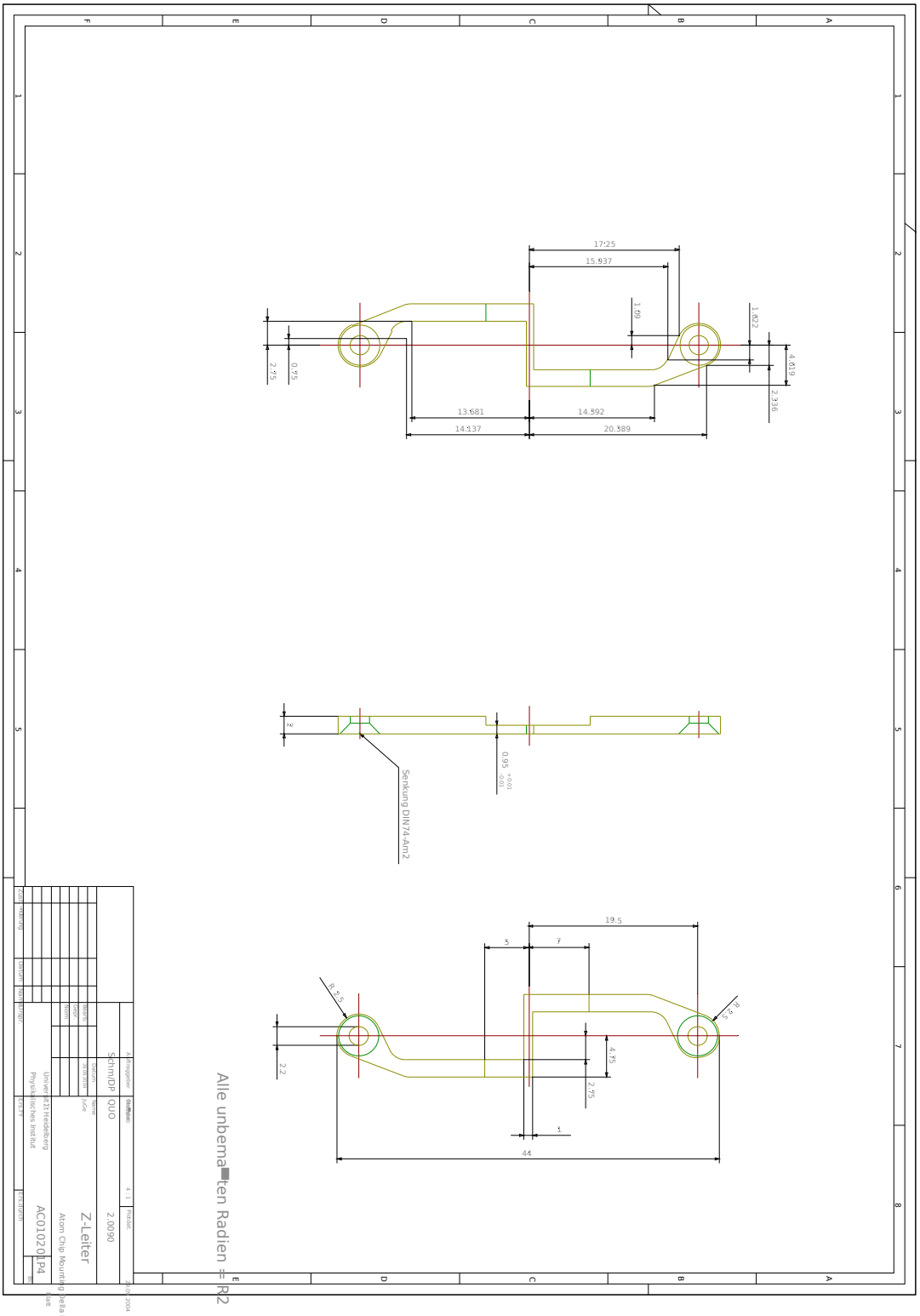
17.25
15.937
1.09
1.622
4.619
2.336
2.75
0.75
13.681
14.892
14.137
20.889
Senkung DIN74-Am2
0.95 +0.01 -0.01
19.5
5
7
6.25
6.25
4.75
2.75
2.2
1
44
Alle unbemaßten Radien = R2
Z-Leiter
Atom Chip Mounting Della Pietra
AC01020_P4
Schm/DP
QUO
2.0090
4 : 1
Physikalisches Institut
Universität Innsbruck

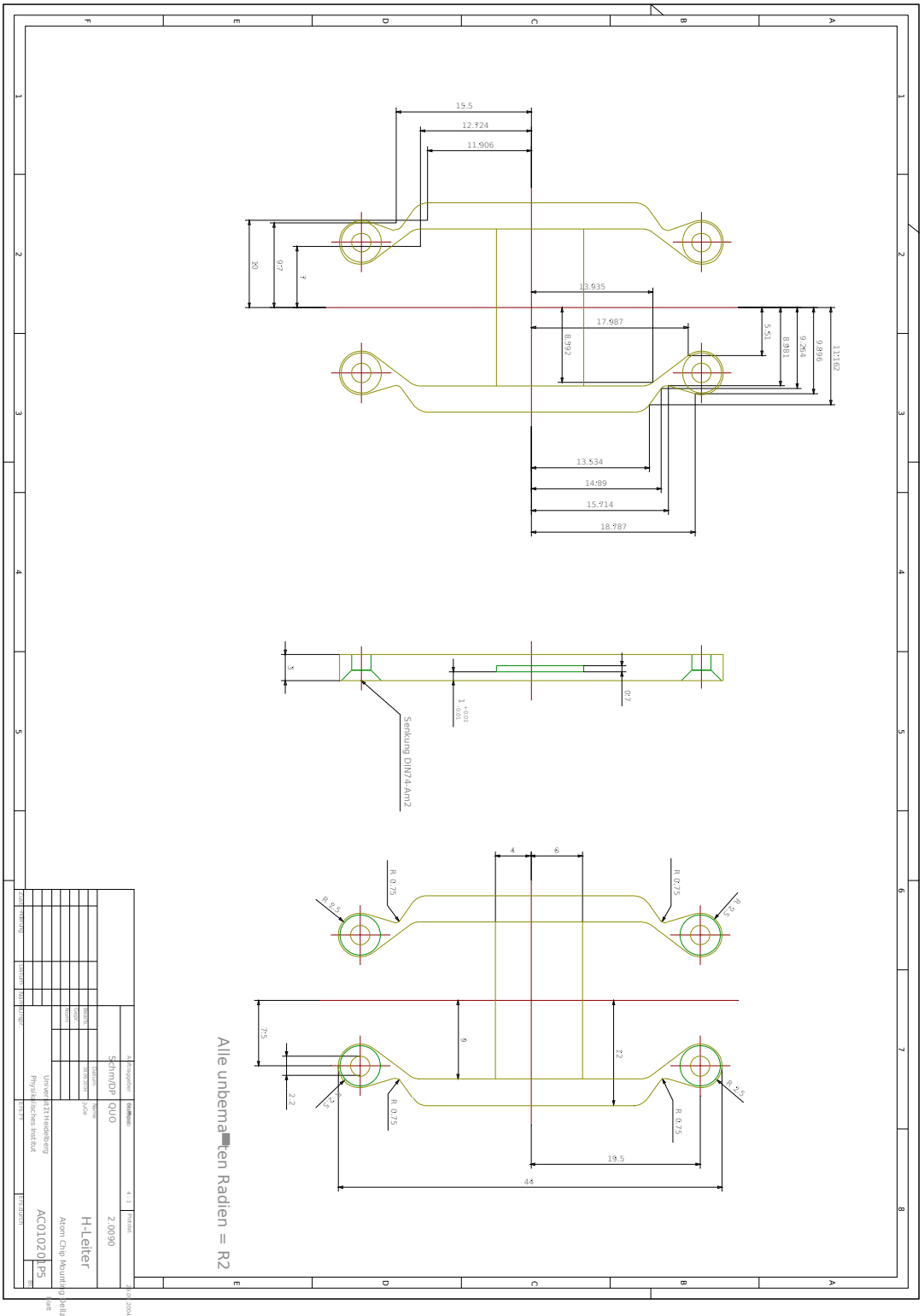
15.5
12.724
11.906
30
9.7
7
13.935
17.987
8.592
5.51
8.981
9.264
9.896
11.102
13.534
14.89
15.714
18.787
5
1 +0.01 -0.01
0.7
Senkung DIN74-Am2
4
6
R 0.75
R 0.5
7.5
9
12
2.2
19.5
44
Alle unbemaßten Radien = R2
Schm/DP
QUO
H-Leiter
Atom Chip Mounting Delta Pietra
AC01020_PS
Universität Heidelberg
Physikalisches Institut
2.0090
4:1

Index

Bibliography

[1] A. Einstein. Quantentheorie der Strahlung. *Phys. Zeits.*, 13:121, 1917.

[2] Steven Chu, L. Hollberg, J. E. Bjorkholm, Alex Cable, and A. Ashkin. Three-dimensional viscous confinement and cooling of atoms by resonance radiation pressure. *Phys. Rev. Lett.*, 55(1):48–51, Jul 1985.

[3] Kurt Gibble and Steven Chu. Laser-cooled Cs frequency standard and a measurement of the frequency shift due to ultracold collisions. *Phys. Rev. Lett.*, 70(12):1771–1774, Mar 1993.

[4] K.B. Davis, M.-O. Mewes, M.R. Andrews, N.J. van Druten, D.S. Durfee, D.M. Kurn, and W. Ketterle. Bose-Einstein condensation in a gas of sodium atoms. *Phys. Rev. Lett.*, 75:3969, 1995.

[5] K. M. O'Hara, S. L. Hemmer, M. E. Gehm, S. R. Granade, and J. E. Thomas. Observation of a strongly interacting degenerate Fermi gas of atoms. *Science*, 298:2179, 2002.

[6] N.N. Bogoliubov. 16of 249. *J. Phys. USSR*, 11:23, 1947.

[7] T. Bourdel, L. Khaykovich, J. Cubizolles, J. Zhang, F. Chevy, M. Teich mann, L. Tarruell, S. J. J. M. F. Kokkelmans, and C. Salomon. Experimental Study of the BEC-BCS Crossover Region in Lithium 6. *Physical Review Letters*, 93(5):050401, 2004.

[8] Markus Greiner, Olaf Mandel, Tilman Esslinger, Theodor W. Hänsch, and Immanuel Bloch. Quantum phase transition from a superfluid to a Mott insulator in a gas of ultracold atoms. *Nature*, 415:39, 2002.

[9] P. Cladé, S. Guellati-Khélifa, C. Schwob, L. Julien, and F. Biraben. A promising method for the measurement acceleration of gravity using bloch of ultracold atoms in a vertical standing wave. *Europhys. Lett.*, 71:730, 2005.

[10] David P. DiVincenzo. The physical implementation of quantum computation. *Fortschritte der Physik*, 48:771, 2000.

[11] Jörg Schmiedmayer, Ron Folman, and Tommaso Calarco. Quantum information processing with neutral atoms on an atom chip. *Journal of Modern Optics*, 49:1375, 2002.

[12] R. Folman, P. Krüuger, J. Schmiedmayer, J. Denschlag, and C Henkel. Microscopic atom optics: from wires to an atom chip. *Adv. At. Mol. Opt. Phys.*, 48:263, 2002.

[13] P. Krüger, L. M. Andersson, S. Wildermuth, S. Hofferberth, E. Haller, S. Aigner, S. Groth, I. Bar-Joseph, and J. Schmiedmayer. Disorder potentials near lithographically fabricated atom chips. *arxive preprint cond-mat/0504686*, 2005.

[14] O.R. Frisch. Experimenteller Nachweis des Einsteinschen Strahlungrückstosses. *Z.f.Phys.*, 86:42, 1933.

[15] T. Hänsch and A. Schwalow. Cooling of gases by laser radiation. *Opt. Commun.*, 13:68, 1975.

[16] D. Wineland H. Dehmelt. Proposed $10^14 < \Delta\nu < \nu$ laser fluorescence spectroscopy on TI^+ mono-ion oscillator III. *Bull. Am. Phys. Soc.*, 20:637, 1975.

[17] D. Wineland W. Itano. Laser cooling of atoms. *Phys. Rev. B*, 20:1521, 1978.

[18] A. Ashkin. Trapping of atoms by resonance radiation pressure. *Phys. Rev. Lett.*, 40:729, 1978.

[19] D.J. Wineland, R. E. Drullinger, and F. L. Walls. Radiation-pressure cooling of bound resonant absorbers. *Phys. Rev. Lett.*, 40:1639, 1978.

[20] Steven Chu. The manipulation of neutral particles, Nobel prize lecture. *Rev. Mod. Phys.*, 70:685, 1998.

[21] Claude N. Cohen-Tannoudji. Manipulating atoms with photons, Nobel prize lecture. *Rev. Mod. Phys.*, 70:707, 1998.

[22] William D. Phillips. Laser cooling and trapping of neutral atoms, Nobel prize lecture. *Rev. Mod. Phys.*, 70:721, 1998.

[23] C. Cohen-Tannoudji. *Atomic motion in laser light, in Fundamental Systems in Quantum Optics, Les Houches 1990 Session LIII.* North Holland, -, 1992.

[24] W.D. Phillips. *Laser cooling, Optical Traps and Optical Molasses, in Fundamental Systems in Quantum Optics, Les Houches 1990 Session LIII.* North Holland, -, 1992.

[25] J. P. Gordon and A. Ashkin. Motion of atoms in a radiation trap. *Phys. Rev. B*, 21:1606, 1980.

[26] J. Dalibard and C. Cohen-Tannoudji. Laser cooling below the doppler limit by polarisation gradients: simple theoretical models. *J.Opt.Soc.Am. B*, 6:2023, 1989.

[27] P.J. Ungar, D.S. Weiss, E. Riis, and Steven Chu. Optical molasses and multilevel atoms: experiment. *J.Opt.Soc.Am. B*, 6:2058, 1989.

[28] Umakant D. Rapol, Ajay Wasan, and Vasant Natarajan. Loading of a Rb magneto-optic trap from a getter source. *Phys. Rev. B*, 64:23402, 2001.

[29] A.L. Migdall, J.V. Prodan, and W. Phillips. First observation of magnetically trapped neutral atoms. *Phys. Rev. Lett.*, 54:2596, 1985.

[30] E. Majorana. Atomi orientati in campo magnetico variabile. *Nuovo Cimento*, 9:43, 1932.

[31] M.H. Anderson, J.R. Ensher, M.R. Matthews, C.E. Wieman, and E.A. Cornell. Observation of Bose-Einstein condensation in dilute vapor. *Nature*, 269:198, 1995.

[32] T. Bergeman, G. Erez, and H.J. Metcalf. Magnetostatic trapping fields for neutral atoms. *Phys. Rev. B*, 35:1535, 1987.

[33] D.E. Pritchard. Cooling neutral atoms in a magnetic trap for precision spectroscopy. *Phys. Rev. Lett.*, 51:1336, 1983.

[34] V.S. Bagnato, G.P. Lafyatis, A.G. Martin, E.L. Raab, R.N. Ahmad-Bitar, and D.E. Pritchard. Continuous stopping and trapping of neutral atoms. *Phys. Rev. Lett.*, 58:2194, 1987.

[35] V.V. Vladimirskii. *Sov. Phys. JETP*, 12:740, 1961.

[36] J. Schmiedmayer. *Technical Digest, IQEC 92: XVIIIth International Conference on Quantum Electronics*. Technische Universitat Wien, -, 1992.

[37] J. Schmiedmayer. *Appl. Phys. B*, 60:169, 1995.

[38] J. Schmiedmayer. *Phys. Rev. B*, 52:R13, 1995.

[39] R. Frisch and E. Segrè. *Z. Phys*, 75:610, 1933.

[40] C.V. Sukumar and D.M. Brink. *Phys. Rev. B*, 56:2451, 1997.

[41] S. Gov, S. Shtrikmann, and H. Thomas. Magnetic trapping of neutral particles: Classical and quantum-mechanical study of a Ioffe-Pritchard type trap. *J. Appl. Phys. D*, 87:3989, 2000.

[42] J Reichel. Microchip traps and Bose-Einstein condensation. *Appl. Phys. B*, 74:469, 2002.

[43] C.J. Pethick and H. Smith. *Bose-Einstein Condensation in Dilute Gases*. -, -, 2002.

[44] H.M.J.M. Boesten, A.J. Moerdijk, and B.J. Verhaar. Dipolar decay in two recent Bose-Einstein experiments. *Phys. Rev. B*, 54:29, 1996.

[45] E.A. Burt, R.W. Ghrist, C.J. Myatt, M.J. Holland, E.A. Cornell, and C.E. Wieman. Coherence, correlations and collisions: what one learns about Bose-Einstein condensates from their decay. *Phys. Rev. Lett.*, 79:337, 1997.

[46] J. Söding, D. Guéry-Odelin, P. Desbiolles, F. Chevy, H. Inamori, and J. Dalibard. Three-body decay of a rubidium Bose-Einstein condensate. *Appl. Phys. B*, 69:257, 1999.

[47] O. J. Luiten, M. W. Reynolds, and J. T. M. Walraven. Kinetic theory of evaporative cooling of a trapped gas. *Phys. Rev. B*, 53:381, 1996.

[48] M. Yamashita, M. Koashi, T. Mukai, M. Mitsunaga, and N. Imoto. Optimization of evaporative cooling towards a large number of Bose-Einstein-condensed atoms. *Phys. Rev. B*, 67:23601, 2003.

[49] Tetsuya Mukai and M. Yamashita. Efficient rapid production of a Bose-Einstein condensate by overcoming serious three-body loss. *Phys. Rev. B*, 70:13615, 2004.

[50] Rudolf Grimm, Matthias Weidemüller, and Yurii B. Ovchinnikov. Optical dipole traps for neutral atoms. *Advances in Atomic, Molecular and Optical Physics*, 42:95, 2000.

[51] John D. McGervey. *Introduction to modern physics*. -, -, 1983.

[52] S. N. Bose. Plancks gesetz und lichtquantenhypothese. *Z. Phys*, 26:178, 1924.

[53] A. Einstein. Quantentheorie des einatomigen idealen gases. *Sitzungberichte der Preussischen Akademie der Wissenschaften, Physikalisch-mathematische Klasse*, page 261, 1924.

[54] C.E. Hecht. The possible superfluid behaviour of hydrogen atom gases and liquids. *Physica*, 25:1159, 1959.

[55] F. Dalfovo and S. Giorgini. Theory of Bose-Einstein condensation in trapped gases. *Rev. Mod. Phys.*, 71:463, 1999.

[56] L.P. Pitaevskii and S. Stringari. *Bose-Einstein Condensation*. Clarendon Press, -, 2003.

[57] L.P. Pitaevskii. *Zh. Eksp. Teor. Fiz.*, 40:646, 1963.

[58] E. P. Gross. *Nuovo Cimento*, 20:454, 1961.

[59] E. P. Gross. Hydrodynamics of a superfluid condensate. *J. Math. Phys.*, 4:195, 1963.

[60] G. Baym and C.J. Pethick. Ground-state properties of magnetically trapped Bose-condensed rubidium gas. *Phys. Rev. Lett.*, 76:6, 1996.

[61] Toshio Tsuzuki. Nonlinear waves in the Pitaevskii-Gross equation. *Journal of Low Temperature Physics*, 4:441, 1971.

[62] L. Khaykovich, F. Schreck, G. Ferrari, T. Bourdel, J. Cubizolles, L. D. Carr, Y. Castin, and C. Salomon. Formation of a matter-wave bright soliton. *Science*, 296:1290, 2002.

[63] S. Inouye, S. Gupta, T. Rosenband, A. P. Chikkatur, A. Görlitz, T. L. Gustavson, A. E. Leanhardt, D. E. Pritchard, and W. Ketterle. Observation of vortex phase singularities in Bose-Einstein condensates. *Phys. Rev. Lett.*, 87(8):080402, Aug 2001.

[64] S. Stringari. Collective excitations of a trapped Bose-condensed gas. *Phys. Rev. Lett.*, 77:2360, 1996.

[65] Y. Castin and R. Dum. Bose-Einstein condensates in time dependent traps. *Phys. Rev. Lett.*, 77:5315, 1996.

[66] Yu. Kagan, E. L. Surkov, and G. V. Shlyapnikov. Evolution of a Bose-condensed gas under variations of the confining potential. *Phys. Rev. B*, 54:R1753, 1996.

[67] U. Ernst, A. Martegif, F. Schreck, J. Schuster, and G. Rempe. Bose-Einstein condensation in a pure Ioffe-Pritchard field configuration. *Europhys. Lett.*, 41:1, 1998.

[68] M. Olshanii. Atomic scattering in the presence of an external confinement and a gas of impenetrable bosons. *Phys. Rev. Lett.*, 81:938, 1998.

[69] D.S. Petrov, G.V. Shlyapnikov, and J.T.M. Walraven. Regimes of quantum generacy in trapped 1D gases. *Phys. Rev. Lett.*, 85:3745, 2000.

[70] D.S. Petrov, D.M. Gangardt, and G.V. Shlyapnikov. Low-dimensional trapped gases. *J. Phys. IV*, 116:5, 2005.

[71] B. Paredes, A. Widera, V. Murg, O. Mandel, S. Fölling, I. Cirac, G.V. Shlyapnikov, T.W. Hänsch, and I. Bloch. Tonks-Girardeau gas of ultracold atoms in an optical lattice. *Nature*, 429:277, 2004.

[72] B. Laburthe Tolra, K. M. O'Hara, J. H. Huckans, W. D. Phillip s, S. L. Rolston, and J. V. Porto. Observation of reduced three-body recombination in a correlated 1D degenerate Bose gas. *Physical Review Letters*, 92(19):190401, 2004.

[73] Chiara Menotti and Sandro Stringari. Collective oscillations of a one-dimensional trapped Bose-Einstein gas. *Phys. Rev. B*, 66:43610, 2002.

[74] F. Gerbier. Quasi-1D Bose-Einstein condensates in the dimensional crossover regime. *Europhys. Lett.*, 66:771, 2004.

[75] Matthew P. A. Fisher, Peter B. Weichman, G. Grinstein, and Daniel S. Fisher. Boson localization and the superfluid-insulator transition. 40:546, 1989.

[76] D. Jaksch, C. Bruder, J. I. Cirac, C. W. Gardiner, and P. Zoller. Cold bosonic atoms in optical lattices. *Phys. Rev. Lett.*, 81:3108, 1998.

[77] Wilhelm Zwerger. Mott-Hubbard transition of cold atoms in optical lattices. *J. Opt. B: Quantum Semiclass. Opt.*, 5:1464, 2003.

[78] T. D. Kühner and H. Monien. Phases of the one-dimensional Bose-Hubbard mode. 58:R14741, 1998.

[79] Meret Krämer. *Bose-Einstein Condensates in Rotating Traps and Optical Lattices.* PhD thesis, Universita' degli Studi di Trento, 2004.

[80] K.K. Likharev and A.B. Zorin. Theory of the Bloch-wave oscillations in small Josephson-junctions. *J. of Low Temp. Phys.*, 59:347, 1984.

[81] J. C. Slater. A soluble problem in energy bands. *Phys. Rev.*, 87:807, 1952.

[82] T. Stöferle, H. Moritz, C. Schori, M. Köhl, and T. Esslinger. Transition from a strongly interacting 1D superfluid to a Mott insulator. *Phys. Rev. Lett.*, 92:130403, 2004.

[83] Gretchen K. Campbell, Jongchul Mun, Micah Boyd, Patrick Medley, Aaron E. Leanhardt, Luis G. Marcassa, David E. Pritchard, and Wolfgang Ketterle. Imaging the Mott insulator shells by using atomic clock shifts. *Science*, 313:649, 2006.

[84] M. Abramowitz and I.A. Stegun. *Handbook of Mathematical Functions.* Dover, New York, 1969. Chapter 20.

[85] Ofir E. Alon, Alexej I. Streltsov, and Lorenz S. Cederbaum. Zoo of quantum phases and excitations of cold bosonic atoms in optical lattices. *Phys. Rev. Lett.*, 95:30405, 2005.

[86] L. S. Cederbaum and A. I. Streltsov. Self-consistent fragmented excited states of trapped condensates. *Phys. Rev. B*, 70:23610, 2003.

[87] L. S. Cederbaum and A. I. Streltsov. Best mean-field for condensates. *Phys. Lett. A*, 318:564, 2003.

[88] Alexej I. Streltsov, Lorenz S. Cederbaum, and Nimrod Moiseyev. Ground-state fragmentation of repulsive Bose-Einstein condensates in double-trap potentials. *Phys. Rev. B*, 70:53607, 2004.

[89] K. Gibble, S. Chang, and R. Legere. Direct observation of s-wave collisions. *Phys. Rev. Lett.*, 75:2666, 1995.

[90] Stephan Schneider. *Bose-Einstein condensation in a robust microtrap - the combination of wire traps and atom chips.* PhD thesis, Physikalisches Institut der Universität Heidelberg, 2003.

[91] Alexander Kasper. *Bose-Einstein Kondensation in einer magnetischen Z-Falle.* PhD thesis, Physikalisches Institut der Universität Heidelberg, 2003.

[92] K. I. Lee, J. A. Kim, H. R. Noh, and W. Jhe. A single beam atom trap in a pyramidal and a conical hollow mirror. *Opt. lett.*, 21:1177, 1996.

[93] Ron Folman, Peter Krüger, Donatella Cassettari, Björn Hessmo, Thomas Maier, and Jörg Schmiedmayer. Controlling cold atoms using nanofabricated surfaces: Atom chips. *Phys. Rev. Lett.*, 84:4749, 2000.

[94] Paul Horowitz and Winfield Hill. *The art of electronics.* Cambridge University Press, -, 1989.

[95] Leonardo Della Pietra. Analysis of noise in agilent voltage driver. Internal memo, 2003.

[96] S. Groth, P. Krüger, S. Wildermuth, R. Folman, T. Fernholz, J. Schmiedmayer, D. Mahalu, and I. Bar-Joseph. Atom chips: Fabrication and thermal properties. *Appl. Phys. Lett.*, 85:2980, 2004.

[97] S. Wildermuth, P. Krüger, C. Becker, M. Brajdic, S. Haupt, A. Kasper, R. Folman, and J. Schmiedmayer. Optimized magneto-optical trap for experiments with ultracold atoms near surfaces. *Phys. Rev. A*, 69:30901, 2004.

[98] Johannes Denschlag, Gerhard Umshaus, and Jörg Schmiedmayer. Probing a singular potential with cold atoms: A neutral atom and a charged wire. *Phys. Rev. Lett.*, 81:737, 1998.

[99] M. J. Snadden, J. M. McGuirk, P. Bouyer, K. G. Haritos, and M. A. Kasevich. Measurement of the earth's gravity gradient with an atom interferometer-based gravity gradiometer. *Phys. Rev. Lett.*, 81(5):971–974, Aug 1998.

[100] J. M. McGuirk, G. T. Foster, J. B. Fixler, M. J. Snadden, and M. A. Kasevich. Sensitive absolute-gravity gradiometry using atom interferometry. *Phys. Rev. A*, 65(3):033608, Feb 2002.

[101] Simon Aigner. PhD thesis, Physikalisches Institut der Universität Heidelberg, 2007.

[102] J. Estéve, C. Aussibal, T. Schumm, C. Figl, D. Mailly, I. Bouchoule, C. I. Westbrook, and A. Aspect. Role of wire imperfections in micromagnetic traps for atoms. *Phys. Rev. A*, 70:43629, 2004.

[103] S. Groth. *Development, Fabrication and Characterisation of Atom Chips.* PhD thesis, Physikalisches Institut der Universität Heidelberg, 2006.

[104] J. Fortágh, H. Ott, S. Kraft, A. Günther, and C. Zimmerman. Surface effects in magnetic microtraps. *Phys. Rev. A*, 66:41604, 2002.

[105] A. E. Leanhardt, Y. Shin, A. P. Chikkatur, D. Kielpinski, W. Ketterle, and D. E. Pritchard. Bose-Einstein condensates near a microfabricated surface. *Phys. Rev. Lett.*, 90:100404, 2003.

[106] M. P. A. Jones, C. J. Vale, D. Sahagun, B.V. Hall, and E. A. Hinds. Spin coupling between cold atoms and the thermal fluctuations of a metal surface. *Phys. Rev. Lett.*, 91:80401, 2003.

[107] C. Henkel and M. Wilkens. Heating of trapped atoms near thermal surfaces. *Europhys. Lett.*, 47:414, 1999.

[108] C. Henkel, S. Pötting, and M. Wilkens. Loss and heating of particles in small and noisy traps. *Appl. Phys. B*, 69:379, 1999.

[109] C. Henkel and S. Pötting. Coherent transport of matter waves. *Appl. Phys. B*, 72:73, 2001.

[110] C. Henkel. Magnetostatic field noise near metallic surfaces. *Eur. Phys. J. D*, 35:59, 2005.

[111] P.K. Rekdal, S. Scheel, P. L. Knight, and E. A. Hinds. Thermal spin flips in atom chips. *Phys. Rev. B*, 70:13811, 2004.

[112] B.Zhang, C. Henkel, E. Haller, S. Wildermuth, S. Hofferberth, P. KrÃijger, and J. Schmiedmayer. Relevance of sub-surface chip layers for the lifetime of magnetically trapped atoms. *Eur.Phys.J. D.*, 35:97, 2005.

[113] S.Scheel, P. K. Rekdal, P. L. Knight, and E. A. Hinds. Atomic spin decoherence near conducting and superconducting films. *Phys. Rev. B*, 72:42901, 2005.

[114] V. Dikovsky, Y. Japha, C. Henkel, and R. Folman. Reduction of magnetic noise in atom chips by material optimization. *Eur. Phys. J. D*, 35:87.

[115] Hartmut Gimpel. Magnetische oberflächenfallen für atom-interferometer. Master's thesis, Physikalisches Institut der Universität Heidelberg, 2003.

[116] Daniel Gallego Garcia. Dipolfallen in atomchip-experimenten. Master's thesis, Physikalisches Institut der Universität Heidelberg, 2005.

[117] Mihael Brajdic. Entwicklung einer computersteuerung und ihre anwendung in einem experiment zur vereinfachten Bose-Einstein kondensation in einer oberflächenfalle. Master's thesis, Physikalisches Institut der Universität Heidelberg, 2003.

[118] Proceedings of the 1998 Enrico Fermi summer school on Bose-Einstein condensation in Varenna, Italy. *Loading of a Rb magneto-optic trap from a getter source HMMM, making, probing....*, 1998.

[119] L.Della Pietra, S. Aigner, C. vom Hagen, H.J. Lezec, and J. Schmiedmayer. Cold atoms near surfaces: Designing potentials by sculpturing wires. *J. Phys.: Conf. Ser.*, 19:30, 2005.

[120] L.Della Pietra, S. Aigner, H.J. Lezec, and J. Schmiedmayer. Designing potentials by sculpturing wires. *cond-mat/0604619*, 2006.

[121] Alexander Bietsch and Bruno Michel. Size and grain-boundary effects of a gold nanowire measured by conducting atomic force microscopy. *Appl. Phys. Lett.*, 80:3346, 2002.

[122] J.Meingailis. Focused ion beam technology and applications. *J.Vac.Sci.Technol.B*, 5:469, 1987.

[123] S. Wildermuth, S. Hofferberth, I. Lesanowsky, E. Haller, L. Mauritz Andersson, S. Groth, I Bar-Joseph, P. Krüger, and J. Schmiedmayer. Microscopic magnetic-field imaging. *Nature*, 435:440, 2005.

[124] P. Krüger, X. Luo, M. W. Klein, K. Brugger, A. Haase, S. Wildermuth, S. Groth, I. Bar-Joseph, R. Folman, and J. Schmiedmayer. Trapping and manipulating neutral atoms with electrostatic fields. *Phys. Rev. Lett.*, 91:233201, 2003.

[125] A. Smerzi, S. Fantoni, S. Giovanazzi, and S. R. Shenoy. Quantum coherent atomic tunneling between two trapped Bose-Einstein condensates. *Phys. Rev. Lett.*, 79:4950, 1997.

[126] R Feynman, R Leighton, and M Sands. *The Feynman Lectures on Physics; Vol. I.* Addison-Wesley Pub. Co, -, 1965.

[127] Mary L.Boas. *Mathematical Methods in the Physical sciences.* Wiley ed, -, 1966.

[128] B.J.Roth, Nestor G. Sepulveda, and John P. Wikswo. Using a magnetometer to image a two-dimensional current distribution. *J.Appl.Phys*, 65:361, 1989.

[129] L.Della Pietra, S. Aigner, C. vom Hagen, H.J. Lezec, and J. Schmiedmayer. Cold atoms near surfaces: Designing potentials by sculpturing wires. *J. Phys.: Conf. Ser*, 19:30, 2005.

[130] D.M.Stamper-Kurn, H.-J. Miesner, A. P. Chikkatur, S. Inouye, J. Stenger, and W. Ketterle. Reversible formation of a Bose-Einstein condensate. *Phys. Rev. Lett.*, 81:2194, 1998.

[131] S. Wildermuth, S. Hofferberth, I. Lesanovsky, S. Groth, P. Kruger, J. Schmiedmayer, and I. Bar-Joseph. Sensing electric and magnetic fields with Bose-Einstein condensates. *Applied Physics Letters*, 88(26):264103, 2006.

[132] Daw-Wei Wang, M.D. Lukin, and E. Demler. Disordered Bose-Einstein condensates in quasi-one-dimensional magnetic microtraps. *Phys. Rev. Lett.*, 92:76802, 2004.

[133] J. Fortagh, H. Ott, S. Kraft, A. Günther, and C. Zimmerman. Surface effects in magnetic microtraps. *Phys. Rev. B*, 66:41604(R), 2002.

[134] A. E. Leanhardt, Y. Shin, A. P. Chikkatur, D. Kielpinski, W. Ketterle, and D. E. Pritchard. Bose-Einstein condensates near a microfabricated surface. *Phys. Rev. Lett.*, 90:100404, 2003.

[135] M. P. A.Jones, C. J. Vale, D. Sahagun, B. V. Hall, and E. A. Hinds. Spin coupling between cold atoms and the thermal fluctuations of a metal surface. *Phys. Rev. Lett.*, 91:80401, 2003.

[136] J.Estéve, C. Aussibal, T. Schumm, C. Figl, D. Mailly, I. Bouchoule, C. I. Westbrook, and A. Aspect. Role of wire imperfections in micromagnetic traps for atoms. *Phys. Rev. B*, 70:43629, 2004.

[137] T. Schumm, J. Estéve, C. Figl, J.-B. Trebbia, C. Aussibal, H. Nguyen, D. Mailly, I. Bouchoule, C.I. Westbrook, and A Aspect. Atom chips in the real world: the effects of wire corrugation. *Eur.Phys.J.D*, 32:171, 2005.

[138] K. Richter T. Paul and P. Schlagheck. Nonlinear resonant transport of Bose-Einstein condensates. *Phys. Rev. Lett.*, 94:20404, 2005.

[139] Saijun Wu, Ying-Ju Wang, Quentin Diot, and Mara Prentiss. Splitting matter waves using an optimized standing-wave light-pulse sequence. *Physical Review A (Atomic, Molecular, and Optical Physics)*, 71(4):043602, 2005.

[140] Ying-Ju Wang, Dana Z. Anderson, Victor M. Bright, Eric A. Cornell, Quentin Diot, Tetsuo Kishimoto, Mara Prentiss, R. A. Saravanan, Stephen R. Segal, and Saijun Wu. Atom Michelson interferometer on a chip using a Bose-Einstein condensate. *Physical Review Letters*, 94(9):090405, 2005.

[141] E. G. M. van Kempen, S. J. J. M. F. Kokkelmans, D. J. Heinzen, and B. J. Verhaar. Interisotope determination of ultracold rubidium interactions from three high-precision experiments. *Phys. Rev. Lett.*, 88(9):093201, Feb 2002.

[142] Daniel A. Steck. Rubidium 87 D line data. 2003.